KAUNAS UNIVERSITY OF TECHNOLOGY
VYTAUTAS MAGNUS UNIVERSITY

IEVA PALEVIČIŪTĖ

RESEARCH AND DEVELOPMENT OF THE ROBOTIZED METAL AND POLYMER SHEET INCREMENTAL FORMING PROCESSES

Doctoral dissertation
Technological Sciences, Mechanical Engineering (T 009)

Kaunas, 2022

This dissertation was prepared at Kaunas University of Technology, Institute of Mechatronics, during the period of 2018–2022.
The right of doctoral studies has been granted to Kaunas University of Technology together with Vytautas Magnus University.

Scientific Supervisor:
Prof. Habil. Dr. Vytautas OSTAŠEVIČIUS (Kaunas University of Technology, Technological Sciences, Mechanical Engineering, T 009).

Edited by: English language editor Armandas Rumšas (Publishing House *Technologija*), Lithuanian language editor Violeta Meiliūnaitė (Publishing House *Technologija*)

Dissertation Defence Board of Mechanical Engineering Science Field:

Chief researcher, Dr. Gintautas DUNDULIS (Kaunas University of Technology, Technological Sciences, Mechanical Engineering, T 009) – **chairperson**;
Prof. Dr. Sergei KRUCHININ (Bogolyubov Institute of Theoretical Physics, Ukraine, Natural Sciences, Physics, N 002);
Prof. Dr. Juozas PADGURSKAS (Vytautas Magnus University, Technological Sciences, Mechanical Engineering, T 009);
Prof. Habil. Dr. Minvydas Kazys RAGULSKIS (Kaunas University of Technology, Technological Sciences, Natural Science, Informatics N 009).

The official defence of the dissertation will be held at 1 p.m. on the 27th of June, 2022 at the public meeting of the Dissertation Defence Board of the Mechanical Engineering Science Field in the Dissertation Defense Hall at Kaunas University of Technology.

Address: Donelaičio 73-403, 44249 Kaunas, Lithuania.
Phone (+370) 37 300 042; fax (+370) 37 324 144; email doktorantura@ktu.lt

The doctoral dissertation was sent out on the 27th of May, 2022.
The doctoral dissertation is available on the internet at http://ktu.edu and at the library of Kaunas University of Technology (Donelaičio 20, 44239 Kaunas, Lithuania) and the library of Vytautas Magnus University (Donelaičio 52, 44244, Kaunas, Lithuania)

KAUNO TECHNOLOGIJOS UNIVERSITETAS
VYTAUTO DIDŽIOJO UNIVERSITETAS

IEVA PALEVIČIŪTĖ

METALO IR POLIMERO LAKŠTŲ ROBOTIZUOTŲ LAIPSNIŠKO FORMAVIMO PROCESŲ TYRIMAI IR TAIKYMAI

Daktaro disertacija
Technologijos mokslai, mechanikos inžinerija (T 009)

Kaunas, 2022

Disertacija rengta 2018–2022 metais Kauno technologijos universiteto Mechatronikos institute.
Doktorantūros teisė Kauno technologijos universitetui suteikta kartu su Vytauto Didžiojo universitetu.

Mokslinis vadovas
Prof. Habil. dr. Vytautas OSTAŠEVIČIUS (Kauno technologijos universitetas, technologijos mokslai, mechanikos inžinerija, T 009).

Redagavo: anglų kalbos redaktorius Armandas Rumšas (leidykla „Technologija“), lietuvių kalbos redaktorė Violeta Meiliūnaitė (leidykla „Technologija“)

Mechanikos inžinerijos mokslo krypties disertacijos gynimo taryba:
vyr. m. d. dr. Gintautas DUNDULIS (Kauno technologijos universitetas, technologijos mokslai, mechanikos inžinerija, T 009) – **pirmininkas**;
prof. dr. Sergejus KRUCHININ (Bogoliubovo teorinės fizikos institutas, Ukraina, gamtos mokslai, fizika, N 002);
prof. dr. Juozas PADGURSKAS (Vytauto Didžiojo universitetas, technologijos mokslai, mechanikos inžinerija, T 009);
prof. habil. dr. Minvydas Kazys RAGULSKIS (Kauno technologijos universitetas, gamtos mokslai, informatika, N 009).

Disertacija bus ginama viešame Mechanikos inžinerijos mokslo krypties disertacijos gynimo tarybos posėdyje 2022 m. birželio 27 d. 13:00 val. Kauno technologijos universiteto Disertacijų gynimo salėje.

Adresas: K. Donelaičio g. 73-403, 44249 Kaunas, Lietuva.
Tel. (370) 37 300 042; faks. (370) 37 324 144; el. paštas doktorantura@ktu.lt

Disertacija išsiųsta 2022 m. gegužės 27 d.
Su disertacija galima susipažinti internetinėje svetainėje http://ktu.edu ir Kauno technologijos universiteto bibliotekoje (K. Donelaičio g. 20, 44239 Kaunas) ir Vytauto Didžiojo universiteto bibliotekoje (K. Donelaičio g. 52, 44244, Kaunas, Lithuania).

CONTENTS

LIST OF ABBREVIATIONS

ANN – Artificial Neural Network
CAD – Computer Aided Design
CAM – Computer Aided Manufacturing
CAPP – Computer Aided Process Planning
CAX – Citrix Application Experience
CE – Calculated Error
CNC – Computer Numerical Control
DBN – Deep Belief Network
DT – Decision Trees
EHIF – Electric Hot Incremental Forming
ELU – Exponential Linear Unit
FE – Finite Element
GPR – Gaussian Process Regression
IE – Erichsen Index
IO – In-to-Out
KNN – *K*-Nearest Neighbors
LASPIF – Laser Assisted Single Point Incremental Forming
MAE – Mean Absolute Error
ML – Machine Learning
MSE – Mean Squared Error
NC – Numerical Control
NGSVE – Negative General Semi-Vertical Edge
OI – Out-to-In
OPGF – Ordinary Positive General Freeform
PGSVE – Positive General Semi-Vertical Edge
PLC – Programmable Logic Controller
PVC – Polyvinyl Chloride
RMSE – Root Mean Square Error
RBT – Rigid Body Translation
ReLU – non-linear activation function
RMSE – Root Mean Square Error
SF – Stretch Forming
SPIF – Single Point Incremental Forming
SVM – Support Vector Machine
SSR – Sum of Squares of Residuals
SST – Total Sum of Squares
Tanh – Hyperbolic tangent

INTRODUCTION

Importance of the topic

Industry 4.0 is a new industrial revolution, and the adoption of this new concept offers enormous opportunities to deliver the initiatives of the *Green European Course*, while promising to improve the quality, flexibility and efficiency of any production process. It is a new strategy to boost growth by addressing some of the key environmental and climate challenges, based on investment in green technologies, sustainable solutions and new businesses. Lithuania supports the goal of the year 2050 to move towards a climate-neutral impact on the EU economy, provided that competitiveness is maintained**.** The success of European companies in competing with Asian manufacturers has been driven by a shift from mass production to customized products. In this context, traditional sheet-forming processes seem less and less viable as they involve the design and development of expensive stamping equipment that pays off only in mass production conditions. Thus, the incremental metal and polymer sheet forming technology developed in this work is the answer to this problem, as it allows the development of quality products without the additional costs associated with the conventional processes. The *Single Point Incremental Forming* (SPIF) research is currently underway in the world, and this technology is not used at all in Lithuania. One of the reasons for this is the environmental requirements, especially with the launch of the *Green European Course*, as well as the technological features of this process, which have not yet been fully explored. In contrast to the simplicity of the technology itself and the ability to implement it with traditional technological equipment such as *Computer Numerical Control (CNC)* machines or the universal robots the SPIF process itself requires a theoretical investigation of the sheet metal forming limits under stretch-bending conditions and dynamic characteristics of a robotized process. In this research in addition to mathematical models, robotized sheet SPIF equipment is being developed, and innovative methods of metal and polymer sheets forming by ultrasonic excitation, which eliminates environmentally harmful lubrication, and laser heating, allowing the waiver of the sheet support, are being proposed. In this way, it is possible to shorten the manufacturing time of the product and speed up its market entry. Production costs are also reduced by using robots instead of expensive CNC machines for the SPIF process. This research work is dedicated to R&D, one of the key milestones in *Industry 4.0*, where digital and physical devices for SPIF processes of metals and polymers are getting developed and tested for the first time in Lithuania. The great benefit of SPIF is such that the development of the product is economical even during small-scale production, and its design can be changed very quickly and easily with minimum costs. The combined research results of the SPIF processes of metals and polymers in this work allowed highlighting the advantages of each process and providing solutions for the improvement of this technology. The holistic concept of SPIF from the digital component model using the artificial neural network algorithms is presented for the researched forming processes. A suitable network structure has been created. Datasets for proper training have been developed. The network topology has been identified, trained and tested. Comparative analysis of machine learning algorithms with the

objective to predict the effect of force on robotic shaping has allowed the identification of the most efficient algorithms. The peculiarities of different network configurations, training algorithms and their sets have been investigated. Comparative analysis of machine learning algorithms for predicting the effect of force on the robotized forming has been performed. The R&D results that are presented in this research will be accessible to the developers of *Future Smart Factories*; furthermore, the developed strategies shall facilitate the supply of the required products under critical conditions imposed by the Globalization processes.

Aim and objectives of the research

The aim of the research is to investigate and develop robotized metal and polymer sheets single point incremental forming and to predict the forming forces by machine learning algorithms.

To achieve this aim, the following objectives have been set:

1. To theoretically investigate the sheet metal forming limits under stretch-bending conditions and dynamic characteristics of robotized process;
2. To validate and apply the developed and patented robotized environmentally friendly metal sheet incremental forming technology;
3. To perform comparative analysis of machine learning algorithms for predicting the effect of force on the robotized forming;
4. To theoretically and experimentally investigate the robotized polymer sheet single point incremental forming technology and to develop an efficient polymer heating method.

Research methods

Virtual and physical research methods were used for investigation in this work. The theory of vibration was applied to describe the models that were implemented in the commercial *LS-Dyna, Ansys, and Comsol Multiphysics 5.1*. software packages. Piezoelectric transducers, 3D scanning laser Doppler vibrometer (*Polytec Inc.*), *PicoScope* hardware and software were used in the study. Theoretical conclusions were validated by an experimental study conducted at Kaunas University of Technology, Institute of Mechatronics.

Defended statements

1. The coefficients of friction of lubricated and vibrated technological surfaces are identical.
2. Spot heating without a support plate allows the stiffness of the polymer sheet to be maintained.
3. Artificial intelligence techniques speed up product development.

Scientific novelty

1. The developed numerical model of metal sheet SPIF made it possible to the sheet metal forming limits under stretch-bending conditions and dynamic characteristics of robotized process.

2. The proposed and developed methods of heating and forming the polymer allowed formulating the conditions for the most suitable extraction of the product shapes.
3. The ANN and GPR models were found to be the most efficient for the forming force prediction.

Practical significance

1. Technologies of robotized metal and polymer sheets incremental forming have been developed and researched. They are entirely new in Lithuania.
2. The developed and patented forming technology replaces the lubrication of technological surfaces with environmentally friendly vibration excitation.
3. The developed and patented sheet forming tool speeds up and reduces the cost of the product development process.

Research approbation

The research presented in the dissertation has been covered in scientific journals and conferences: three articles have been published in the *Web of Science* indexed international journals with a high impact score: journal *Sensors* (IF3.275), journal *Materials* (IF 3.623), and a further article has been presented in the indexed international journal *IEEE Proceedings*.

The results have been presented in the following international conferences:

The 24th International Scientific Conference *Mechanika* 2019, Kaunas.

The 15th International Conference *Mechatronic Systems and Materials* 2020, Poland.

The 25th International Scientific Conference *Mechanika* 2021, Kaunas.

The following patent applications have been submitted:

V.Ostaševičius, V.Jūrėnas, V.Grigaliūnas, D.Eidukynas, A.Bubulis, I.Palevičiūtė. *Incremental forming machine for sheet metal parts*. Patent Application number LT2020 516.

V.Ostaševičius, V.Jūrėnas, D.Eidukynas, A.Bubulis, I.Palevičiūtė, V.Ambrasas. *Incremental forming machine for sheet plastic parts*. Patent Application number LT2020 528.

V.Ostaševičius, V.Jūrėnas, A.Bubulis, D.Eidukynas, A.Paulauskaitė-Tarasevičienė, I.Palevičiūtė. *Incremental forming device for sheet parts*. Patent Application number LT2021 549.

Structure of the dissertation

This dissertation consists of an introduction, the main part which is split into four chapters, conclusions, references, and the list of publications.

I. LITERATURE REVIEW

Introduction

With the rapid advancements of the industry technology, many new concepts have emerged in manufacturing. The next generation of industry, defined by the far-sighted term *Industry 4.0*, highlights a new industrial revolution. This new paradigm shift utilizing the application and connectivity of Artificial Intelligence algorithms commits to increasing the manufacturing flexibility, thereby allowing better results in the manufacturing process as a whole. This chapter provides the technological features of sheet forming, as well as general information on the applicable test methods, product shape design, and extraction capabilities required for successful sheet deformation, the selection of the forming angles, friction reduction and sheet heating methods. The perspective methods of using ultrasonic vibrations, forming force prediction by artificial intelligence methods, and the use of formed polymers for biomedical purposes are discussed as well.

1.1. General information about the process under study

In order to clearly state the performed research, other authors who are engaged in this type of research were sought and their works were analyzed. Keyword phrases or words were refined during this type of search. The search for information began with the most recent articles, which reveal not only the latest research findings and interpretations, but also include links to older publications.

The paper [1] presents a classical sheet single-point incremental forming (SPIF) scheme (Fig. 1.1) and a model of the sheet blank based on the analysis based on the membrane analogy, which involves the interaction of the membrane with a rod-shaped forming tool. The rotating tool moves in two perpendicular directions in contact with the surface of the sheet blank, thereby deforming it. The sheet blank is pressed onto the rig surface by a blank holder. In order to limit the deflection of the sheet blank behind the tool action area, the sheet blank is supported by a backing plate.

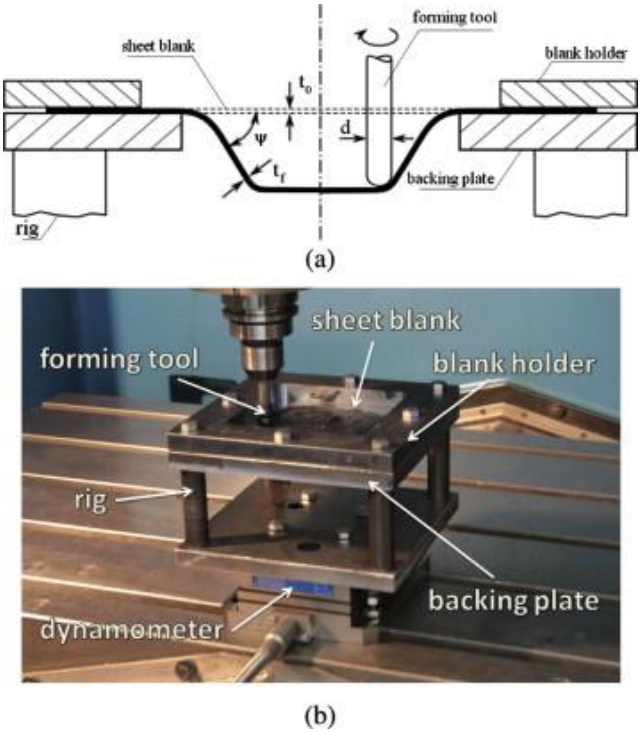

Fig. 1.1 Sheet forming process scheme (a) and photograph (b) [1]

Another publication illustrates how asymmetric and complex product configurations can be formed with a single tool [2]. One of the most popular industrial examples is *Ford's 'Company Rapid freeform technology'* (Fig. 1.2). This process can be used to create asymmetric 3D products. As the success of new models in one of the fastest growing automotive industries is determined by design decisions, the ability to create a model layout in a few hours by using this technology is promising and often determines the speed with which a new product enters the market. Unlike 3D printing, this technology allows creating large car body details and ensures minimal cross-sectional deviations, not to mention the involved production time and costs.

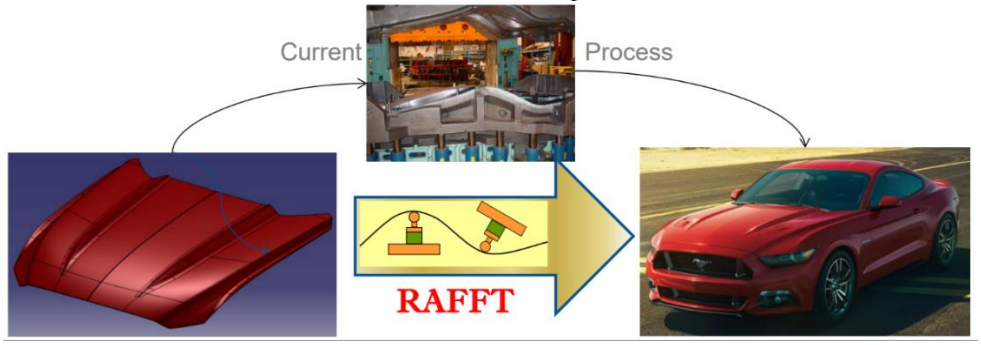

Fig. 1.2 Rapid free form technology (RAFFT) in *Ford Company* [2]

The research [3] is based on the theory of splines focused on the formation of asymmetric parts using the CNC technology, thereby replacing the expensive stamping process (Figure 1.3). The paper compares traditional and modern forming methods, trying to exemplify the development of different sheet metal bending methods. The focus is on shear forming, conventional and modern computer-controlled forming methods. Peculiarities of forming were revealed using the Standard Triangular Language (STL) file format orthogonal to the part Computer-Aided Design (CAD) model surface and the implementation of the spline method.

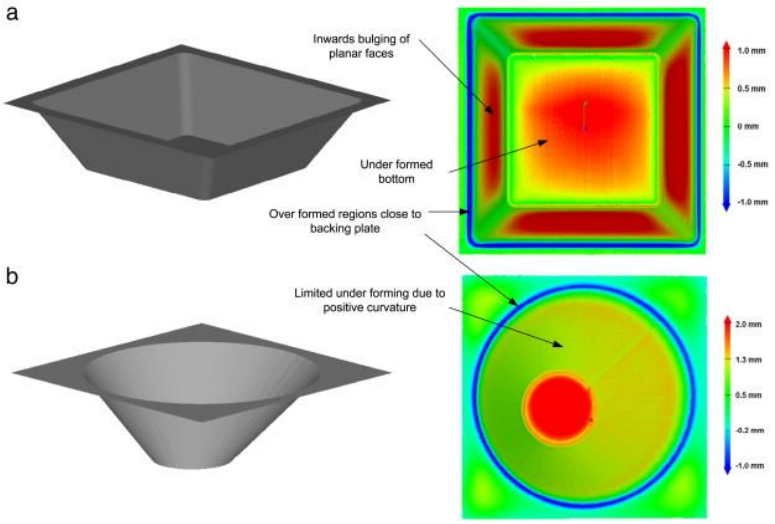

Fig. 1.3 Products in asymmetrical shape: a) truncated pyramid, b) conical shape [3]

The article [4] analyzes the SPIF process using theoretical and experimental methods. The interaction of the forming tool with the plate described in the principles of membrane analogy was evaluated during the modeling. The article [5] shows that the process of incremental sheet forming is substantially different from the traditional sheet deformation methods. These differences are related to the type and size of the tool, the feed rate, the friction on the sheet surface, and all this affects the formability of the sheet. The forming of a straight groove was chosen as the standard deformability test method, which resulted in a reduction in friction and in the feed rate. The most suitable diameter of the forming tool was found equal to 10 mm. It has also been observed that the due the plane-anisotropy the formability depends from the direction of the tool displacement. The influence of the rotation speed and direction of the forming tool on the incremental forming process is evaluated in [6]. In the experimental research program, the coefficient of friction on the surface sheet was evaluated. As a result, a significant decrease in forming force was observed when the tool was being rotated in both directions, and this is related to the coefficient of friction. Temperature measurements revealed the dependence of the sheet heating temperature on the tool rotation speed and direction. The micro-roughness of the sheet surface was little affected by the forming regimes. The absolute value of the ratios of the horizontal F_h to the vertical F_v force components (see Fig. 1.4 for a non-rotating

tool) showed an upward trend in the first and second columns, while it showed an almost constant trend of the stand in the central area of the specimens in the third and fourth columns where the evaluation was performed.

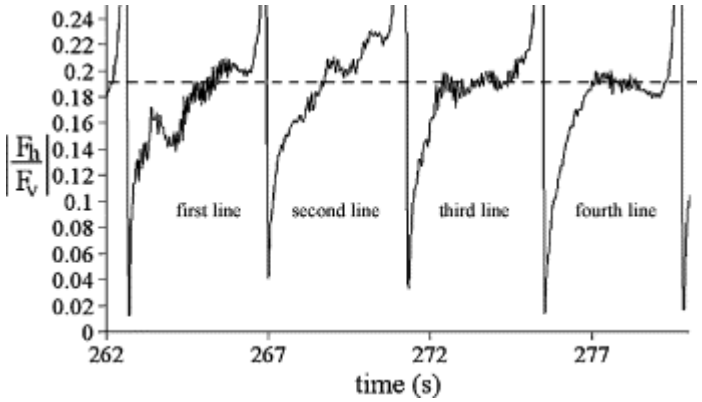

Fig. 1.4 Absolute value of the ratio of the F_h and vertical F_v components of the forming force to estimate the coefficients of friction [6]

1.2. Possibilities to increase metal sheet forming capabilities

The process of improvement of the incremental forming technology is related to the evaluation of the factors determining the formability of the sheet. In addition to reducing the coefficient of friction between the technological surfaces, the improvement in the formability parameters of the sheet under the influence of temperature is increasingly being noted. This is important in forming products from materials such as titanium [7]. This article is devoted to the forming of human implants from titanium sheets. The geometric accuracy of the implants is related to the springback effects, so heating the sheet reduces its stiffness and makes it easier to achieve the required dimensional and shape accuracy. Bearing in mind that lubrication of the technological contact surface also improves the formability, it is noted that the grease liquefies under the influence of temperature, so recommendations are made for the choice of lubricants.

The article [8] is devoted to the discussion of the temperature regime of a car door formed from a titanium alloy (Ti6Al4V). The equipment shown in Fig. 1.5 was intended for heating the Ti sheet (the temperature can be further increased by turning the tool). The equipment consists of a support for the connection to a CNC machining center workbench, i.e. that the temperature development in the central area of the sheet can be monitored continuously throughout the forming tests. The results of the research have showed that the values of the largest deformations measured in the formed sheet increased continuously with the increasing tool rotation speed, and that this issue affected the accuracy of the formed part as well as the surface quality in general.

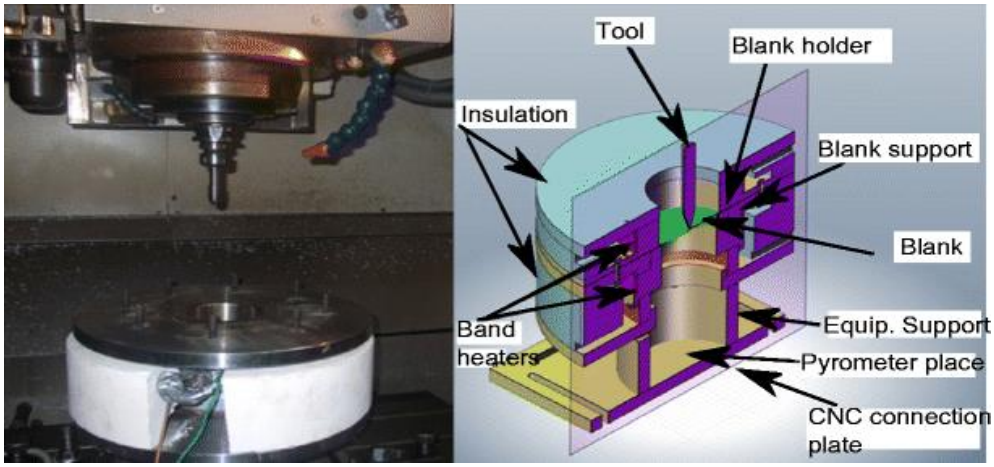

Fig. 1.5 Ti sheet heating equipment [8]

The *Laser Assisted Single Point Incremental Forming (LASPIF)* process is presented in [9]. In Fig. 1.6, the schematic LASPIF setup allows the part to be heated at a selected location near the tool contact area, and it is possible to dynamically track the movement of the forming tool. By using the LASPIF process to form titanium sheets (0.6 mm thick). The heating of the workpiece allowed to reduce the molding forces, the stress level, and the springback effects of the springs, which resulted in an increased product accuracy and formability.

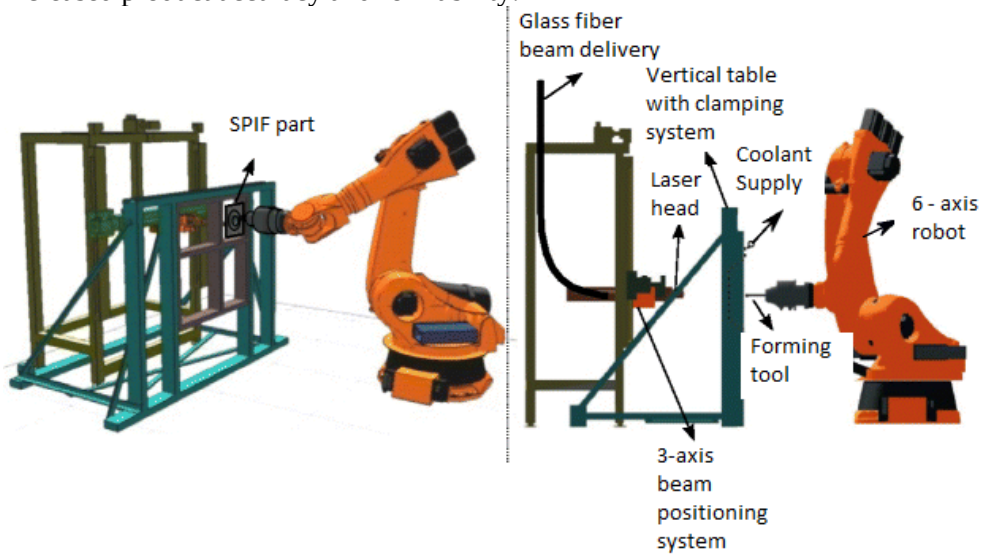

Fig. 1.6 Robotized forming stand setup [9]

The paper [10] analyzes the formability problems of 1mm thick AZ31B magnesium alloy. The maximum forming angle was found to be 64°, and Electric Hot Incremental Forming (ESIF) is a great alternative to a variety of sheet heating methods. Although the incremental forming of sheets of various alloys is easily

realized at room temperature, magnesium alloys with limited ductility during processing require additional heating. The efficient heating system proposed in the article is integrated into CNC machines, where the electric current flowing through the sheet metal generates heat to facilitate the forming process. A temperature range from 150 to 250 °C is considered to be the most suitable, as it provides a higher formability than at room temperature.

In another paper [11], statistical evaluation of the effect of *Electric Hot Incremental Sheet Forming (EHISF)* on the three types of metal sheets is presented. It was concluded that the formability of Ti-6Al-4V titanium sheets is influenced by both the amount of electric current and the lubrication of the contact surfaces, while the formability of aluminum alloy AA6061 sheets is mainly influenced by electric current, but the formability of cold-rolled steel DC01 is determined by the type of the lubricating fluid and the feed rate. A schematic view of the *EHISF* equipment is presented in Fig. 1.7.

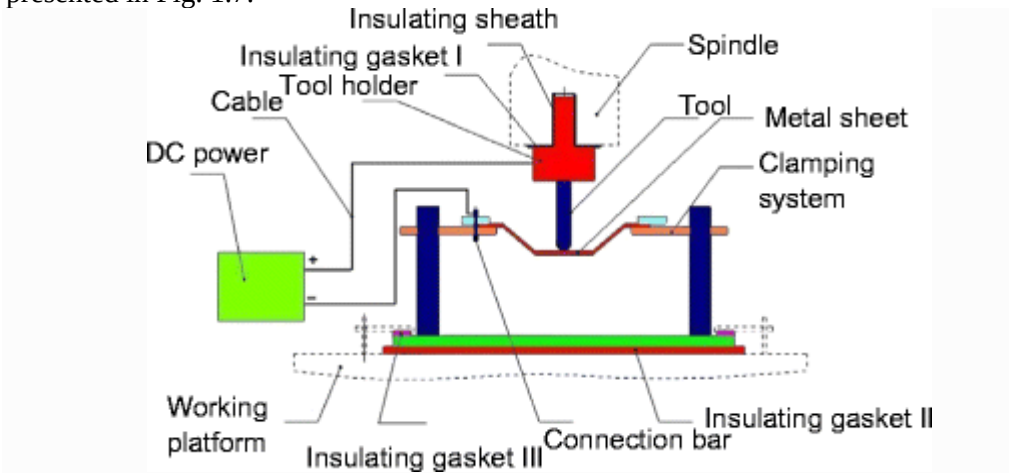

Fig. 1.7 Schematic view of the electric hot incremental sheet forming process [11]

The article [12] is devoted to the evaluation of the dependence of the formability of aluminum and titanium sheets on the size of the forming angles. Joule's effect sheet heating equipment was developed for experimental research. The influence of the forming angle on the amount of the heat energy generated in the sheet, which could be useful in optimizing the forming processes, has been evaluated. The microstructural aspects of the materials related to the influence of micrograins on heating and the induced strain depending on the properties of the material were also evaluated. The effect of electric heating on the formability of Ti-6Al-4V titanium sheets is also investigated in [13]. It has been found that the amount of the heat transferred to the sheet through the tool is highly dependent on the diameter of the tool and the draw angle. The choice of Ni disulfide for lubrication allows the formation of a more accurate draw angle product up to 72° in the high temperature range of 500–600 °C. In addition, the proposed lubricant protects the sheet surface from oxidation. The paper [14] deals with the thermal phenomena of AZ31 sheets. In order to reduce the coefficient of friction, the sheet surface was coated with a ceramic

nano-K2Ti4O9 coating, thus achieving a value of 0.1 coefficient of friction. Another study on the temperature formation of AZ31 magnesium alloy sheets is presented in [15]. The entire 1 mm thick AZ31-O sheet was heated above 150 °C with a hot air blower. The sheet temperature was controlled by three thermocouples which were giving feedback while being connected to a controller. The device view is shown in Fig. 1.8. Formability evaluation tests showed that a forming angle of 60° can be achieved at 300 °C temperature. The effect of tool depth step and the temperature was also found to be significant, but the tool size had no significant effect. The best formability results were obtained at a heating temperature of 250 °C.

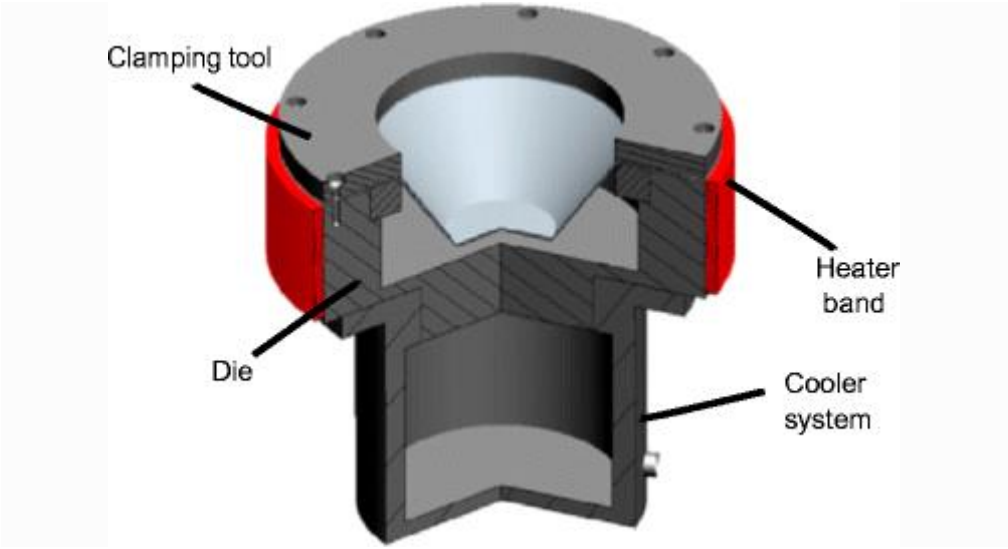

Fig. 1.8 Schematic of AZ31 sheet heating device [15]

The results of the formability study of a heated AZ31B magnesium alloy sheet are presented in [16]. The flow of oil heated to 300 °C is fed into the tool housing (Fig. 1.9) which transfers heat to the sheet by heating it by convection. Microstructural analysis of the products formed in this way showed that, at temperatures of 250 °C, the complete recrystallization process took place, at which a forming angle of up to 60° could be reached. The magnesium alloy products thus formed are in great demand in the automotive and aerospace industries.

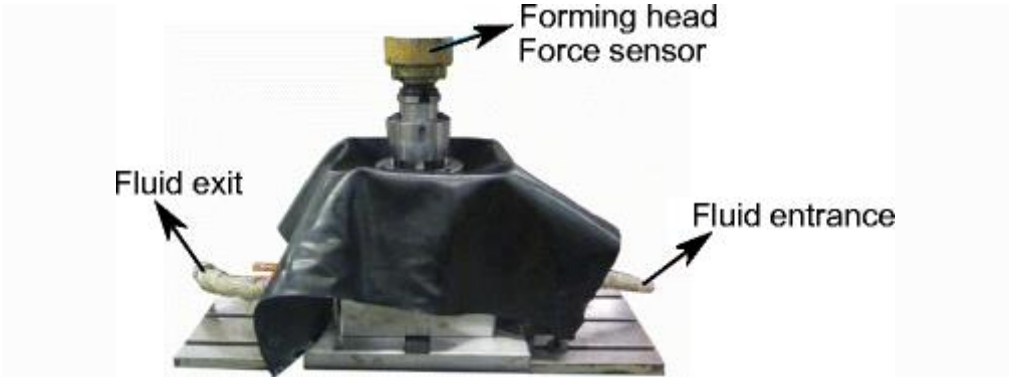

Fig. 1.9 An oil-based heating device [16]

1.3. Material redistribution during SPIF

The gradual decrease in the sheet thickness during forming depends on the achievable wall angle. An increase of this angle reduces the wall thickness of the product, which compromises the strength characteristics of the finished products. The paper [17] proposes a five-step strategy for forming a cylindrical product. A cone is first formed, which is then brought closer to a cylindrical shape without changing the tool depth in between the steps. The In-to-Out (IO-up) and Out-to-In (OI-down) methods correspond to the direction of tool movement (Fig. 1.10, a). This study has shown that the directions of movement of the OI and IO tool affect the wall thickness distribution of the product. Such an improved multi-stage forming strategy also allowed the formation of the flat-bottom surface of a cup. Results of similar studies were discussed in [18]. The numerical modeling trajectories obtained during the formation of the five-step strategy are shown in Fig. 1.10, d. The thinning of the sheet during five-step forming may outweigh the reduction in the wall thickness observed in the course of single-step processing. This strategy forms vertical walls, but substantial tangential strains may be exceeded if comparing to the one-step strategy.

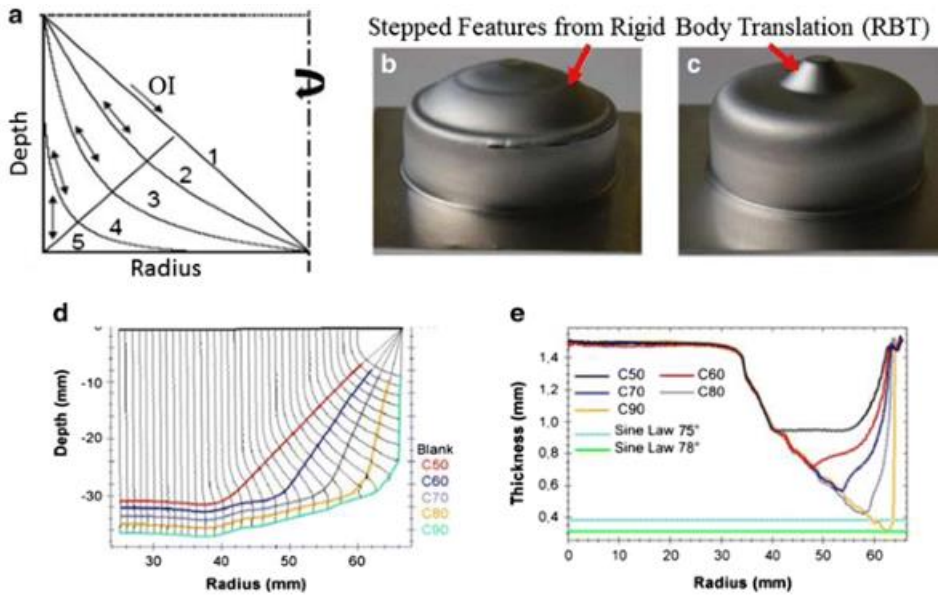

Fig. 1.10 (a) Cross-section of multi-step tool path strategies implemented in [17]; (b) the part formed by using OI and (c) the part formed by using IO; (d) material flow and cross-sections in accordance with the OI five-step strategy implemented in [18]; (e) appropriate thickness profiles

Before starting the incremental forming, it is necessary to predict the accuracy of the formed product which is achieved between different steps. The simulation results presented in [19] show that a more uniform sheet thickness distribution in the double forming process is beneficial as the total area of plastic deformation increases, but the tool trajectory determines the geometric accuracy of the final product. In the SPIF process, the tool is pressing the sheet at the edges (Fig. 1.11). The results of numerical simulation of the forming process of aluminum alloy Al 3003-O SPIF with respect to isotropic hardening and the anisotropic law of elastoplastic behavior are presented in [20]. In the first part of this paper, detailed theoretical and experimental evaluation of the process is performed to determine the influence of continuous and discontinuous tool trajectories. In the second part of the paper, the results of the numerical simulation are presented for conical and pyramidal models of different thicknesses. After obtaining the results of the numerical simulation, a study was performed to evaluate the formed product.

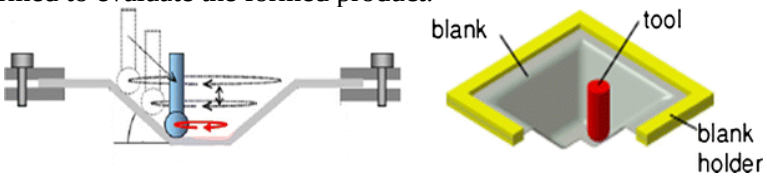

Fig. 1.11 Sheet pressed at the edges formed by a single tool [20]

The accumulation of strain described in [21] makes it possible to estimate the influence of changes in the tool path direction in the corner areas of a pyramid-shaped

part drawing. The semi-vertical rib significantly influences the deformation patterns of the forming process, and this effect is inversely proportional to the size of the corner angle. In order to address this issue, the article reveals how a toolpath strategy was developed to increase the product accuracy. For example, during incremental forming, the depth of the tool path is constantly changing [22], and, in order to better capture geometric transitions, it is necessary to estimate and limit volumetric errors. It is also possible to define the contour of the tool path to a certain depth by manipulating the slope of the intersecting planes. When the depth is increased, the plane of the intersection is gradually rotated about the selected axis for the purpose of determining the path of the tool. The paper [23] presents the extension of this idea by identifying the features based on the number of intersections of contours at a given depth, Z (Fig. 1.12).

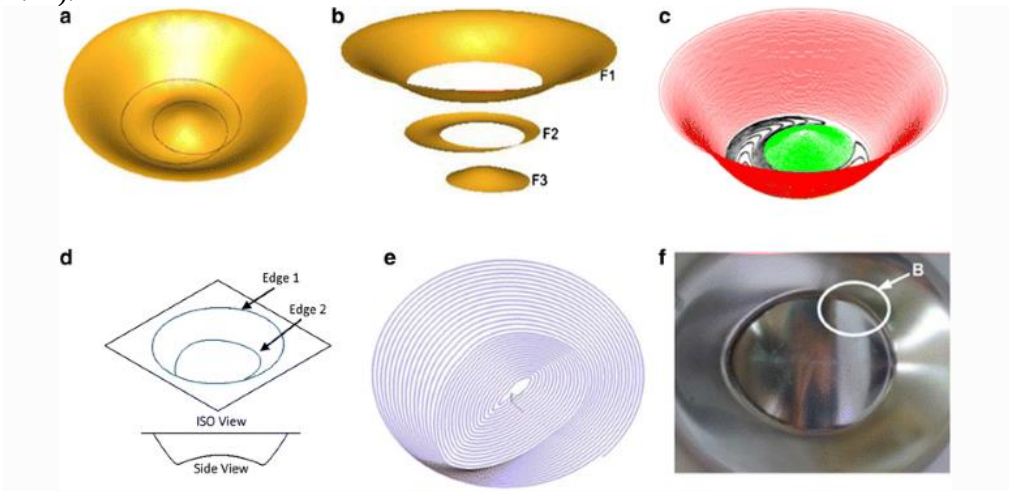

Fig. 1.12 Identification of features: (a) desired geometry when slicing at the Z level; (b) different identification of the region and sequence of forming; (c) the resulting tool path; (d) the part with a flat bottom; (e) separation by using a spiral tool path; (f) the inside of the formed part in area B compared to the standard part obtained by Z-level slicing

An alternative to this method is to take into account the tool paths optimized for the recognized feature, while also considering the aspects of the local surface finish. The overall tool path trajectory is then obtained by joining the individual tool paths according to the continuity requirements for the different properties [24], as applied in Figure 1.13.

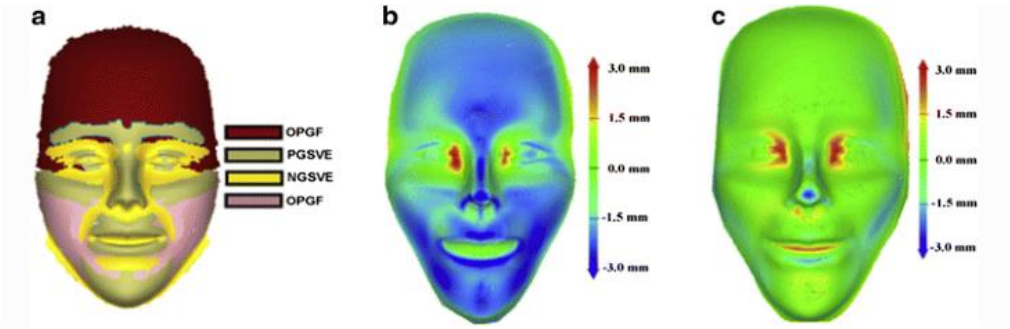

Fig. 1.13 SPIF made from Al 1050 human face replica: (a) various features of: OPGF – Ordinary Positive General Freeform, PGSVE – Positive General Semi-Vertical Edge, and NGSVE – Negative General Semi-Vertical Edge. (b) SPIF process without precision compensation compared to (c) where the precision compensation methods are used [24]

The paper [25] presents a methodology based on FE modeling intended to reduce geometric inaccuracies. So far, the expected deviation between the surface calculated from the tool trajectory and the part actually caused by elastic deformations has been integrated into the systematic compensation scheme. Due to the abundance of possible parameters and combinations, the *Multivariate Adaptive Regression Splines (MARS)* software package was used to automate the prediction process. A compensation strategy was developed and implemented while using this model, which showed a significant improvement in accuracy.

1.4. Tool trajectory formation

Together with the pure SPIF process, additional processes, such as Stretch Forming, are also being used. Therefore, there is a need for special technological equipment to perform such hybrid processes. CAD/Computer Aided Process Planning (CAPP)/CAM classic software for toolpath programming was integrated into the Citrix Application Experience (CAX) environment platform in the study [26]. As of the moment of writing this thesis, software tools were being used to form each combined stretch-forming together with the SPIF. The SPIF for the CAX environment has been developed by numerical control. As the stretch-forming does not provide the final part geometry, the part's properties must finally be formed by the SPIF process after stretch-forming. This is achieved by scanning the results of the FE modeling of the stretch-forming process into a CAD/CAM system. The areas formed by SPIF are thus detected, and the tool path trajectory planning is shown in red in Fig. 1.14.

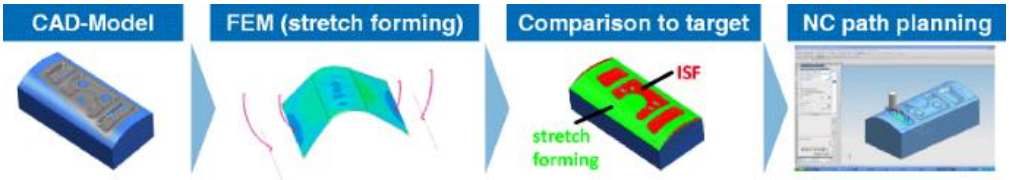

Fig.1.14 CAX process integration in tool path planning [26]

Simulations with 8 stretch-forming axes and 5-axis SPIF are performed by estimating collisions so that to ensure the safe use of the hybrid process. A laser-assisted LASPIF has been developed; it uses collision estimation to ensure safety of the hybrid process. The laser-operated LASPIF was designed with special optics which rotate the laser beam around the forming tool. Thus, the position of the laser focus was determined by the angle of rotation with respect to the X axis (Fig. 1.15).

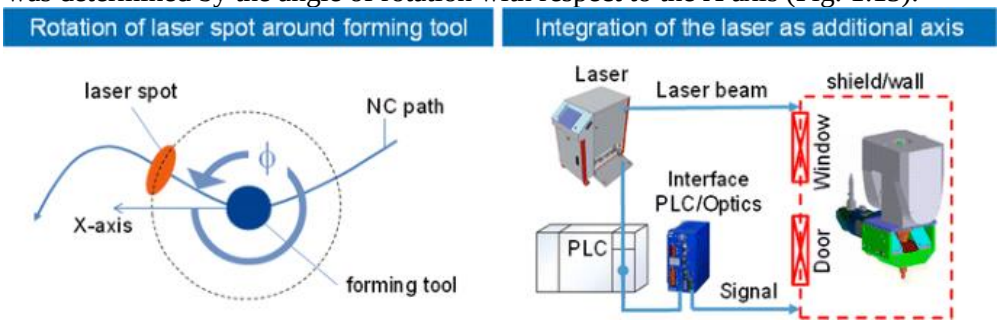

Fig. 1.15 (a) Integration of the rotating laser into the device (b) via *Programmable Logic Controller* (PLC) [26]

The paper [27] discusses the concept of laser-heated asymmetric SPIF while illustrating the laser control and the hot spot location programming used by CAX. The test results have shown that the formability of the Ti grade 5 (TiAl6V4) alloy used in aeronautics can be increased in this way. The developed titanium sheet heating device, consisting of special laser optics and a heating laser, has been successfully integrated into a CNC forming machine. The performed experiments confirmed the results of the initial studies

1.5 Ultrasound in the SPIF process

Lubrication is still the most commonly used process applied to reduce friction between technological surfaces. The use of lubricants pollutes the environment and involves additional costs as products must be washed before they can be placed on the market. It is therefore necessary to look for alternative ways to reduce the forming forces associated with the process dynamics. Until now, ultrasound has only been used to improve sheet forming. The behavior of an ultrasonically excited tool in the sheet metal forming process was investigated in [28]. The amplitude-frequency characteristics of ultrasonically excited metal sheets were analyzed by using numerical FE models. The *ABAQUS* software package was used to evaluate the effect of sheet vibrations on the magnitude of the deformation force. Axial forces using medium frequency ultrasound were found to be almost indistinguishable from the conventional forming without additional ultrasonic excitation. Ultrasonic vibrations can prevent metal sheet fractures and enhance the quality of the material surface. For the validation of the numerical simulation results, an experimental system was developed. The final shape of simulation is shown in Fig. 1.16.

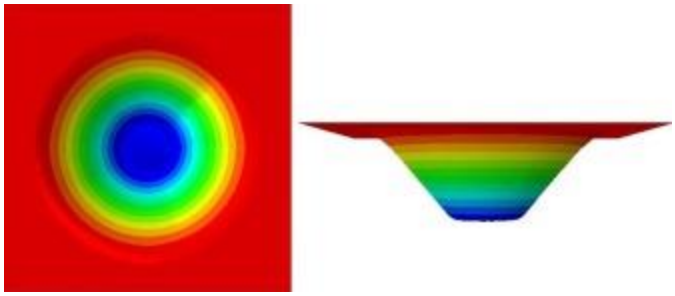

Fig. 1.16 Final shape of simulation [28]

The results of the ultrasonic sheet metal forming process are presented in the paper [29] which shows that the vibration influence on the metal stress, strain and thickness is minimal at the 15kHz frequency. However, with an increase in frequency above 40 kHz, the axial force increases dramatically. These results were obtained by FE modeling with the *ABAQUS* software. The paper [30] presents a detailed study of the sheet metal SPIF by ultrasonic vibration (Fig. 1.17). A new constitutional model of acoustoplasticity was used to evaluate the sheet deformation response to extremely high degrees of deformation. The appropriate experimental studies were also conducted so that to find out the capabilities of constitutional and digital models. Such parameters as the tool size, the tool feed rate, the rotation speed, the step and the amplitude of the tool vibrations, the influence on the forming force and the springback were investigated in detail. The simulation results show that the influence of ultrasound on the stress and thickness of the sheet metal is minimal, and the deformation corresponds to the cosine law, where the deformation is minimal when the oscillation frequency is equal to 15 kHz. Ultrasound also affects the axial force which decreases to 40kHz, but the axial force increases sharply at frequencies above 40 kHz.

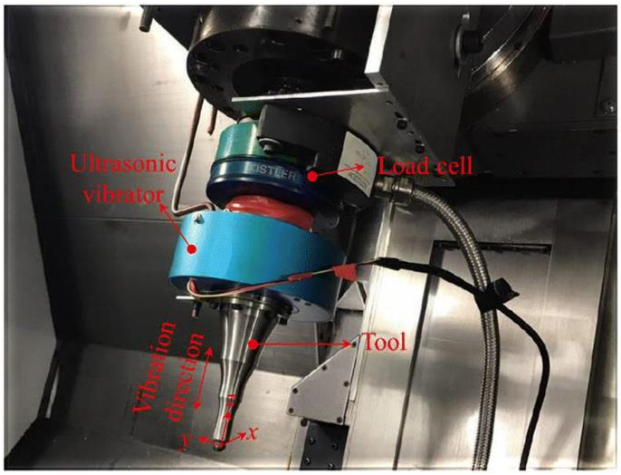

Fig. 1.17 Forming tool with the ultrasonic system [30]

As the review of the research shows, ultrasound is still being used only for the tool excitation; hence, it is necessary to look for other advantages of ultrasound excitation and link them not only to the improvement of the technological process parameters, but also to the solution of ecological problems.

1.6. SPIF process simulation

FE analysis is commonly used for SPIF operations to predict the geometry of the finite part, as outlined in [31]. The force must be accurately predicted in order to limit the road error when using the coupling method. Therefore, the correlation of the forming forces is required for the classical truncated cone formation by increasing the prediction accuracy in the course of examining three influential parameters: the type of finite elements, the boundary conditions, and the law of hardening. This principle was determined as a result of numerical and experimental research. Two FE models have been applied for this purpose: the first model uses brick elements, while the second uses shell elements. Compared to the traditional model based on classical literature hypotheses, the improvement in the force prediction of the first model was 30%. The second model defined a more realistic clamping system with pressure ranges applied in the contact area between the sheet and the blank holder. This technique was used to form a truncated cone and an asymmetrical part (a twisted pyramid). The experimental results showed the relevance of the method, as the errors due to the un-stiffness of the serial robot in both formed parts were reduced by about 80%. When brick elements are being used in the contact area between the tool and the sheet (Fig. 1.18), shell elements are being kept in other areas. This 'mixed model' results in a reasonable computation time, regardless of the selection of the brick elements. On the final mesh with a shell thickness of 4 brick elements, the values of approximately 10° shear angle in each direction were marked.

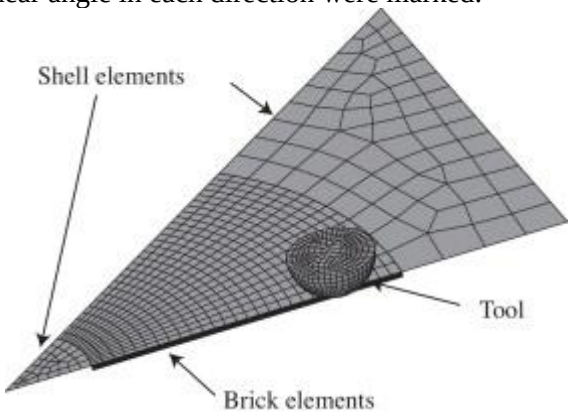

Fig. 1.18 Description of the mix model [31]

The results of the measurements of the *Transverse Thickness Shear (TTS)* in a steel sheet cone-shaped product were presented in [32]. The dependence of the TTS on the angle of the cone wall was determined. SPIF predictions using the Marciniak-Kuczyński (MK) type forming boundary model was presented as well. The paper [33] presents a numerical modeling method saving computer time resources. For this

purpose, the FE mesh is divided into several non-overlapping parts. The plastic substructures describe the part of the sheet in contact with the tool by estimating all nonlinearities such as plastic deformation and the tool slip, while the rest of the sheet is described by pseudo-linear elastic substructures. The simulation divides the substructures into plastic and elastic areas to capture the tool movement. The presented restructuring of modeling is 2.4 times faster than the classical implicit modeling.

The paper [34] investigates how strain monoforms can induce non-monotonic deformation. 50° and 73° cones were formed from a 1.2 mm thick aluminum 3003-O sheet by using an implicit elastic-plastic FE program. Approximately 1/6 of the outer sheet surface was used as an input to predict the forming limits of the Marciniak-Kuczyński type, also taking into account the initial texture-based anisotropy and anisotropic hardening. The same model was used to predict the onset of necking when the strain paths were found from FE simulation. The predicted forming limits were significantly higher than those obtained under monotonic loading.

The incremental forming process clearly enhances the sheet metal formability. In the work [35] based on the original formulations of the micro element force balance according to the isotropic yield criterion was reviewed analytically (Fig. 1.19). The fracture formation limit model, in contrast to the conventional necking, was chosen to depict the failure mechanism of aluminum alloy AA1050-H111. By combining the adequate principle of plastic formation with the stress elements expressed in the form of process parameters, the proposed model agrees well with the experimental results. For the consistent fracture concerns, the results of failure accumulation are provided. The modified fracture forming limit model has been shown to meet the needs of practical application as a process window design specification for damage assessment.

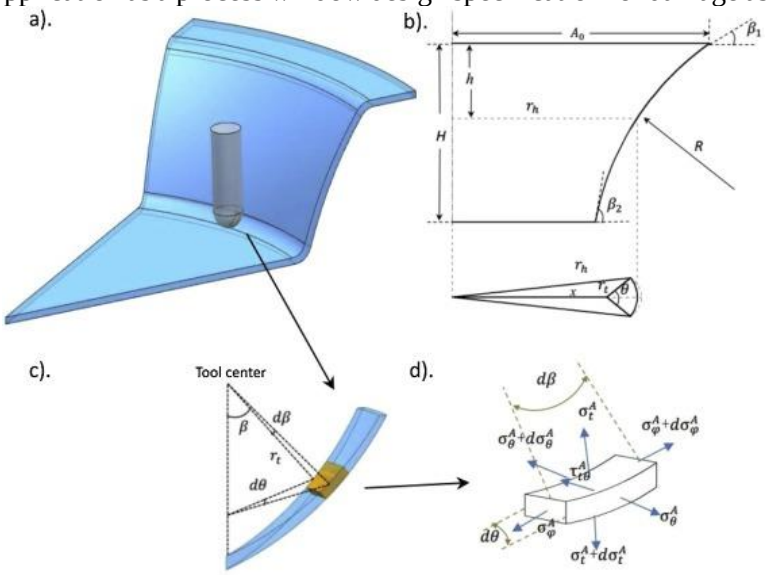

Fig. 1.19 Schematic of the analytical SPIF model: a) fragment of the general image; b) forming a profile; c) tool-sheet contact diagram; (d) sheet element load balance [35]

The strain rate of polymer and metal sheets affects the magnitude of the forming forces and the energy requirements. The influence of the strain rate on the forming parameters of various types of steels was investigated in [36]. This influence was determined on the stress-strain curves of the materials. The results explain that the influence of the strain rate on the forces and energies used in the forming process and on the forming limits is insignificant and highly dependent on the type of the material.

The incremental forming process is superior to other sheet deformation technologies in terms of higher formability. A number of theories have been proposed to elucidate the cause of this phenomenon, but the relationship between the strain state caused by SPIF and specific stress has not been revealed yet. The Tvergaard-Needleman model proposed in the article [37] is used with the objective to predict the SPIF damage to the surface by using the FE modeling. In order for the simulations to be tested and validated, the linear test was run which compared the force and shape predictions with the actual results. Several SPIF cone simulations were performed at different wall angles to be able to predict failures (Fig. 1.20). Porosity appears to reach high strain values only in the area of contact between the tool and the sheet. It seems that effective porosity can significantly exceed the he failure limit (Fig. 1.20, a). According to Gurson Tvergaard Needleman (GTN) –Thomasson criteria for the prediction of a ductile fracture in micro-scaled plastic deformation the coalescence occurs in a similar zone (Fig. 1.20, b). The adequacy of the simulation results for the physical research was confirmed by comparing the experimentally obtained force and shape values.

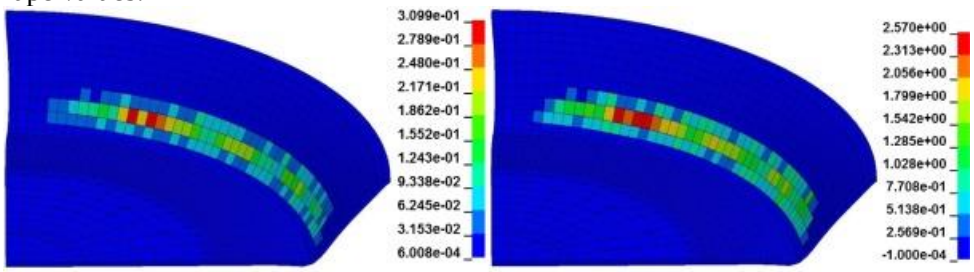

(a) Effective porosity.

(b) Difference between left hand side and right hand side of Thomason criterion (coalescence occurs when positive).

Fig. 1.20 Numerical simulation results when failure occurs (wall angle 52°) [37]

The well-known in the field of aeronautics AlMgSc alloy was investigated in [38]. Gaining more knowledge on this alloy in order to confer the lacking information for the aviation industry and to provide the data to research institutes wishing to create stimulations of the sheet forming processes by using the FE modeling was the primary objective. Multiple experiments were carried out, the laws of materials were selected, and, for the purpose of correctly defining the behavior of the material, its parameters were adjusted. Another goal was to investigate the applicability of the forming process to this material. The shortened cones of multiple structures were formed, and the maximum forming angle was found. A mathematical model was created. It was

confirmed that the model can predict the evolution of force for the process as well as serve as a foundation for the final geometrical structure. In addition, the model helped to better understand the process itself.

The analysis of the publications testifies the presence of a number of necessary modeling studies to assess the risk of sheet metal piercing with a tool and the correct selection of technological parameters in order to make the forming process more efficient.

1.7. Force and thickness predictions

In the SPIF process, the forces acting on the metal sheet change its geometry, thus allowing the creation of products of various configurations. The forming process is highly nonlinear, in which, a significant deformation occurs due to plastic deformation because the acting force is greater than the tensile strength of the metal. In general, this method does not significantly change the thickness and surface properties of the sheet. The forming of sheet metal results in a high area-to-volume ratio. The planning of the shaping process is usually done through the 'trial-and-error' method. However, the optimal design of the process is complicated due to the many properties associated with the mechanical properties of the sheet, the geometry of the forming tool, and the technological parameters of the process. The process of virtual design using the FE method in the physical environment encounters problems related to, for example, the dispersion or friction of the material properties at the point of contact between the tool and the sheet, which can cause cracks and/or other unpredictable defects in the formed wall. Therefore, prediction methods based on artificial intelligence algorithms are also useful during the process design. The use of these methods reduces the amount of production defects and shortens the product's way to the market.

The paper [39] presents a method based on machine learning which serves the objective to predict the occurrence of defects in the performance of sheet metal SPIF due to the properties of the materials. The application possibilities of machine learning methods for forming the Square Cup and U-Channel in three different types of steel sheets were analyzed. It was identified that the ensemble models could be an effective alternative because they allow a better trade-off between the variance and the bias, and are expected to run real data from the sheet metal forming industry. The tensile flow behavior of the aluminum alloy AA5182-O sheet was experimentally obtained in the study [40] to determine the flow behavior of the sheet material while using two computational methods. It has been found that the *Genetic Algorithm (GA)* can solve material flow problems better than linear regression analysis without mathematical constraints. Hardening functions calculated by GA allowed a more accurate prediction compared to the experimental data. The AA5182-O flow stresses decreased to a minimum at mean strain rates (10 to 100 s^{-1}) and then increased with the increasing strain rates. It was found that, among the studied hardening models, only the *Artificial Neural Network (ANN)* could replicate this behavior. The flow stress values calculated by using the Voce hardening function were more consistent with the experimental data compared to the *Khan-Huang-Liang (KHL)* and *Johnson-Cook (JC)* models. The most accurate calculations of the stress values were obtained by using ANN, if

compared analytically with the experimental results, or if using FE simulation. However, the computational cost was high when the method was being used in the FE simulation compared to the KHL or JC hardening functions. The paper [41] presents a methodology and software related to the use of ANN to model SPIF processes for aluminum alloy sheets. The data obtained experimentally or selected from the literature was used for this purpose. The ANN models have been found to be useful when it is not possible to precisely define virtual models due to the complicated shape of the design, the use of new materials, and/or new requirements for the process. *Artificial Intelligence (AI)* methods are important for predicting the product dimensions and geometric accuracy. The paper [42] proposes a technique for the evaluation of geometric accuracy which is considered to be one of the most important quality indicators. As the largest shape deviations are found in the rounded parts of the product, roundness and positioning deviation are selected as the output variables. The *Deep Learning (DL)* and *Shallow Learning (SL)* algorithms were used to evaluate the accuracy of curvilinear surfaces. One of the objectives of this study is to evaluate the performance of the *Deep Belief Network (DBN)* algorithm using the Boltzmann machine approximation so that to form a DBN weight matrix. The tool path direction, the speed and the feed rate, the step depth, the sheet thickness, and the wall tilt angle were selected as the input data (Figure 1.21). DL has been found to be a beneficial tool for predicting the geometric accuracy of a formed product. Otherwise, the DL method is the most suitable because it achieves excellent operating accuracy to predict position deviation and roundness compared to the *Automatic Coding Method*. According to the findings of the article, the contribution of this study is that the DL techniques can be successfully applied to small data, and DL is better able to predict the geometric accuracy in the SPIF process compared to SL.

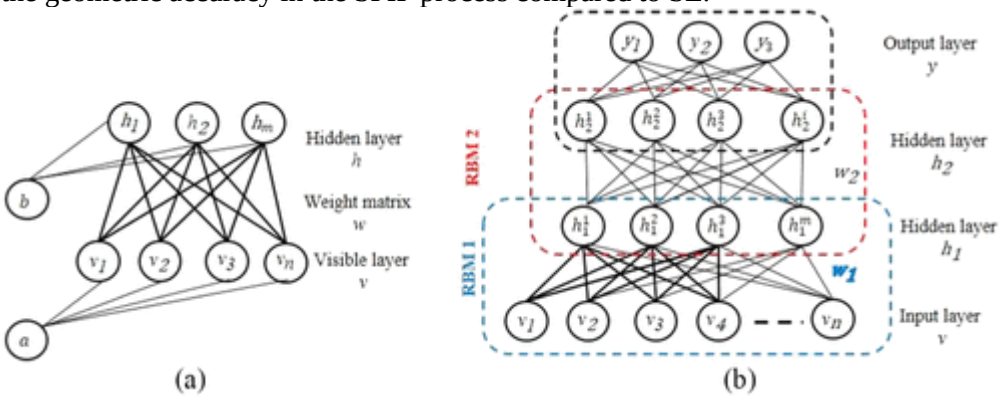

Fig.1.21 (a) Structure of the limited Boltzmann machine and (b) structure of DBN [42]

The results of SPIF-formed *Alclad* aluminum alloy sheets with stiffened ribs are presented in the article [43]. These stiffened sheets are widely used in the aerospace industry due to their excellent strength-to-weight ratio. Aluminum alloy sheets EN AW-7075-T6 and EN AW-2024-T3 were used as the test materials. The influence of forming parameters on roughness was determined by using ANN. An increase of the vertical step reveals the more pronounced ridges found on the inner surface. The

predicted ANN models were characterized by performance indices with R^2 values ranging from 0.657 to 0.979. The change in the surface roughness observed in the paper for uncoated and coated with a soft layer of technically pure aluminum showed that there is no significant difference between the experimental data and the results of the ANN model. Increasing the size of the vertical step increased the surface roughness value of uncoated *Alclad* sheets.

In the study [44], the SPIF process of calamine brass Cu67Zn33 and thin aluminum AA3003-0 alloys were selected as the input, i.e., the wall angle, the spindle speed, the step depth, the tool feed rate and the material type, and the vertical force component were involved as the model output. A multilayer perceptron ANN structure and a feed-forward back propagation algorithm were being used to train the model. As a result, the 6-14-1 model structure was obtained, and 0.215 mean absolute error showed an excellent level of agreement.

From this analysis, it is evident, that very little research has been done so far on the application of the machine learning methods in predicting the technological parameters of the SPIF process, and no comparative analysis of these methods has been found at all.

1.8 Formation of biomedical implants

There is a huge market for medical bone prosthesis. The traditional manufacturing process for biocompatible implants is more costly and time consuming, but, for custom-made items, SPIF is a valuable alternative. In this field, the scanning images of a particular damaged part of the reconstruction are numerically defined by using *Computer Tomography (CT)* scans and transmitted to a CNC machine processor which converts a sheet of material into an implant. Cranioplasty is the surgical repair of a bone defect in the cranium resulting from a previous surgery or injury by placing the custom-made biocompatible implant into the correct location in the cranium. The use of porous material scaffolds made of polymeric components to support the growth of bone cells and tissues is a long-standing area of interest. The use of biocompatible polymer sheets IF is still not widespread. During this process, a tool deforms the surface of the material sheet into the shape of the cranial or bone implant. The article [45] describes the forming process of an implant for a patient with foot orthosis based on 3D scans, thus illustrating the contribution of SPIF to the production of personalized medical devices. In this article, some adaptation was made in the light of the development of innovative techniques for adapting the ankle support. In this way, the SPIF process was chosen for sheet profiling, thus increasing the role of this technology when it is necessary to produce a single complex product. Fig. 1.22 demonstrates the scheme of this process. First, the ankle geometry was determined by using the laser scanning technique, which allows for a very fast scan without any discomfort to the patient compared to the contact-based methods. The second step is related to the formation of a ‘cloud of points’ from which, a continuous surface can be obtained by using the proper order which, of course, reflects the ankle CAD model. In the third stage, parts were created automatically by employing the CAD/CAM program, and the fourth step is related with implant manufacturing as well as the final step involving the dimensional control.

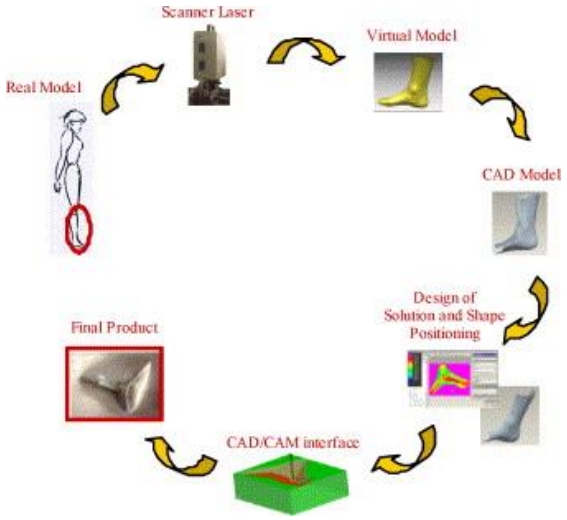

Fig. 1.22 'Round design' process cycle [45]

The technique used in the case of the study was again based on laser triangulation. The desired ankle model was developed in the CAD environment (Fig. 1.23).

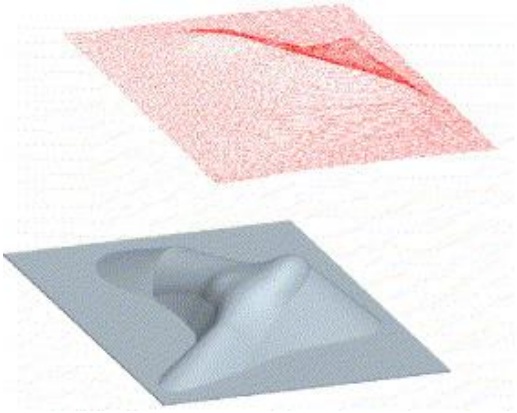

Fig. 1.23 The desired CAD model and the 'true' model [45]

The article [46] refers to the case where flat plates are used. They need to be reconstructed in the skull surgery and production. Cadaver test implants (Fig. 1.24) show that a skull model is properly fitted with the proper application of the function; hence, no adjustment is required during surgical procedures.

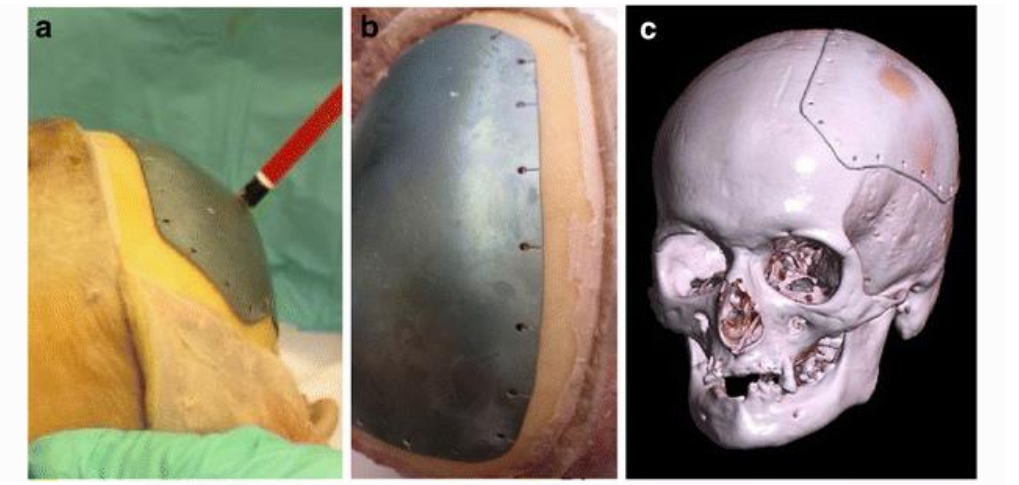

a) b) c)

Fig. 1.24 (a) Skull scanning; b) attaching the implant to the skull; c) reconstructed skull [46]

The article [47] is devoted to the research of a SPIF-formed implant from biocompatible polymer (PCL) sheet. As in the previously described article, a virtual model of the skull fracture geometry is obtained by scanning with the help of a computed tomography device. From the obtained image, a CAD model is created, with the help of which, the shaping process is carried out. Studies have shown that the two points forming could be used instead of single-point incremental forming to improve implant accuracy.

A strategy for improving forming accuracy is discussed in [48] by using the *Double-Side Point Incremental Forming (DSPIF)* method for a titanium sheet skull implant. This is achieved by matching the tool paths of the two forming tools to obtain the shape of the implant. In this way, the sheet strain does not exceed the specified tolerances. Such a forming strategy is called the peripheral support strategy, where the fixed support is replaced by a tool moving at the bottom of the sheet.

Forming processes may also be applied to the reconstruction of fractured clavicles [49]. As, in this case, it is much more difficult to obtain a virtual model of a fractured clavicle, thus X-ray techniques are used. Other problems are related to the strength, geometry, and characteristics of attachment to the human bone tissue, as human bones are subjected to a heavy load. The authors of the article have proposed replacing bulk generic clavicle implants by thin shelled, patient-specific titanium implants. The accuracy of the implant can be satisfied by compensating the tool path. The results of research of the formation of the base of a human denture implant are presented in [50]. This technology replaces the conventional based lost-wax technique, which is longer lasting because it is more manual work intensive. The proposed prosthesis is developed by forming a thin-walled X6Cr17 stainless steel sheet on a CNC machine according to the results of FE analysis and other advanced computer technologies (RP / CAD / CAM / CAE), which allowed optimizing the process parameters (Fig. 1.25).

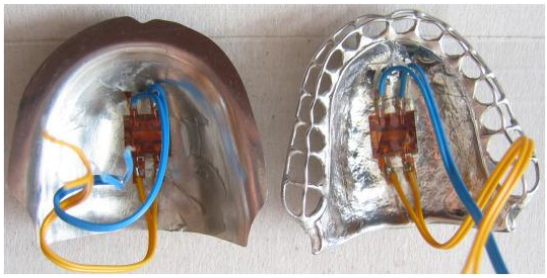

Fig. 1.25 Strain gauges attached to SPIF denture samples [50]

SPIF processes are still being rarely used to repair damage to human organs even despite the fact that SPIF implants can be formed very quickly, which is essential for saving the human life.

1.9 Polymer sheet SPIF

The incremental polymer sheet forming emerged as an alternative to the metal sheet SPIF. One of the main challenges in the forming of some thermoplastics is their higher brittleness compared to metals. Therefore, when forming polymer sheets, it is more difficult to extract the right angles and the greater depth. The analysis of various polymers, such as polyoxymethylene-POM, polyethylene-PE, polyamide-PA, polyvinyl chloride-PVC and polycarbonate-PC, according to their mechanical properties, can be used to solve this problem (Fig. 1.26). Cold formed polymers are denoted by the best formability. PA and PE polymers have been found to be flexible and suitable for forming sharp-angle products. The use of PVC polymer in the production of precision shaped products is recommended due to the low springback properties. PC polymer products do not fade for a long time and are suitable for the products with good surface quality. The flexibility of POM polymers is limited, thus making them unsuitable for SPIF technologies. PA polymers have the highest springback and are therefore used for low-precision products.

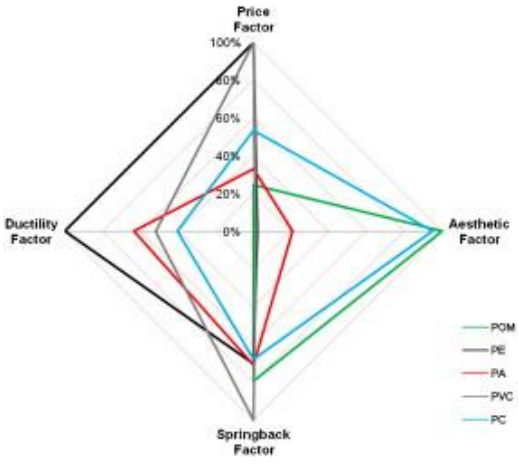

Fig. 1.26 Material evaluation chart [51]

It is clear that there are significant differences between the ability to form metal and polymer sheets [52]. If thin metal sheets are suitable for forming without the wrinkling or cracking of their surfaces, then, only thicker sheets of polymer are suitable for forming while still avoiding these problems. The formability of polymers is determined not only by the parameters of their sheets, but also by the type of polymer discussed in the analysis of the previous publication. In order to increase the viability of the industrial polymer sheet forming process, this technology needs to be improved by expanding the database (Figure 1.27).

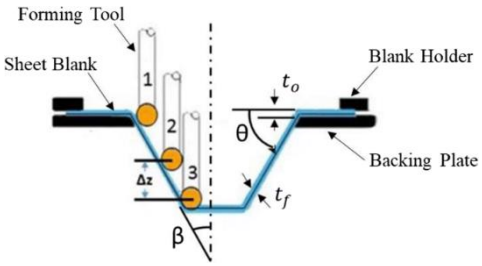

Fig. 1.27 Polymer SPIF [52]

The spifability of polymer, or SPIF formability, is limited by the following possible polymer defects (Fig. 1.28: circumferential crack, twisting, and oblique crack. The circumferential crack is associated with the formation of a crack in the wall rounding zone and is evaluated by material tensile tests. The twisting defect is associated with the wrinkling of the wall rounded zone caused by the rotation of the forming tool, and the oblique crack with the rupture of the wall caused by the high shear stress of the tool moving in a circle. It is obvious that the spindle of the CNC machine tool in which the tool is embedded has a great influence. The obtained research results show that the decisive role of the polymer forming process is played by the sheet material. Therefore, this finding was performed by the analysis of pressure-sensitive membranes. The results of the study support the PVC polymer forming possibilities at room temperature.

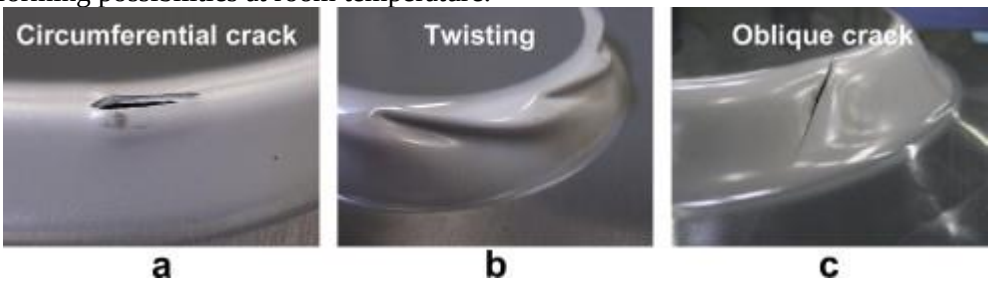

Fig. 1.28 Types of failure in formed polymer products [53]

In order to confirm the previous conclusion, a thermovisor camera was used to record the SPIF temperature of a polymer sheet [54] by varying the rotational speed of the CNC machine spindle. The 2 mm thick PVC sheets used for the tests were formed with a 10 mm diameter tool with a depth of 0.5 mm/rpm. The temperature

distribution is clearly visible in Fig. 1.29 depending on the speed of rotation of the tool. It can be concluded that the rotational speed of the tool not only determines the magnitude of the forming force, but also the formability of the material, as well as the roughness of the product surface, which is the result of the friction of the tool in the sheet causing its temperature increase.

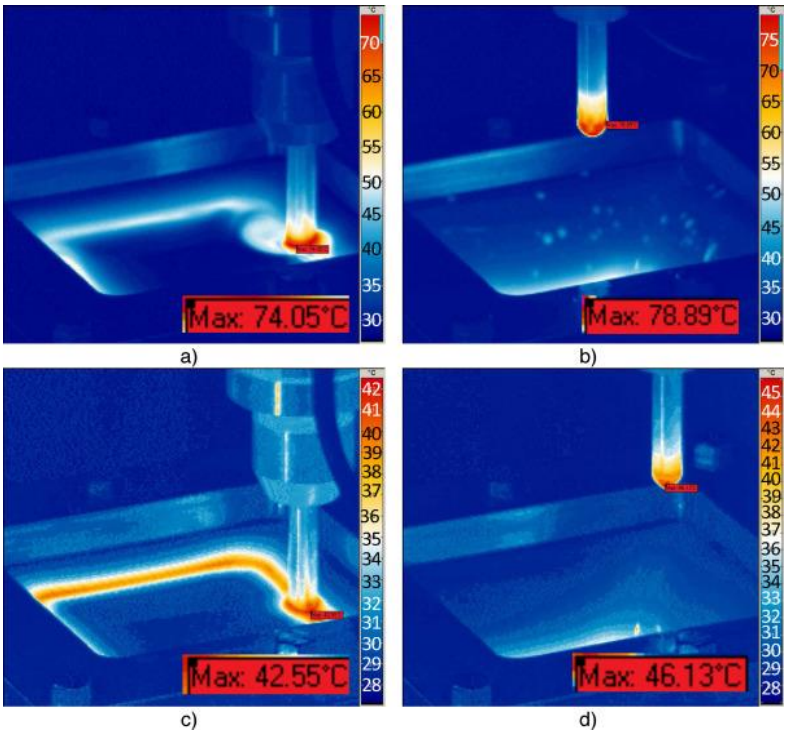

Fig. 1.29 Temperature distribution at spindle speed: a) 2000 rpm. at the beginning of the process; b) 2000 rpm. at the end of the process; (c) at the beginning of slow spindle rotation; and d) at the end of slow spindle rotation [54]

The article [55] presents the influence of the unidirectional tool trajectory on its rotation by estimating the area of contact between the tool head and the polymer sheet in the circular direction. A theoretical model was proposed, and the results of the experiments were presented. It was found that the wrinkles formed in the turn are influenced by the unidirectional trajectory of the tool movement. To avoid this, a spiral trajectory algorithm for the tool movement was proposed, which significantly increased the accuracy of the product. In Fig. 1.30, the visible grid is formed on the surface of the polymer, thanks to which, the strain of the formed part can be observed. The direction of the grid along the sliding direction of the tool indicates the shear stress due to friction.

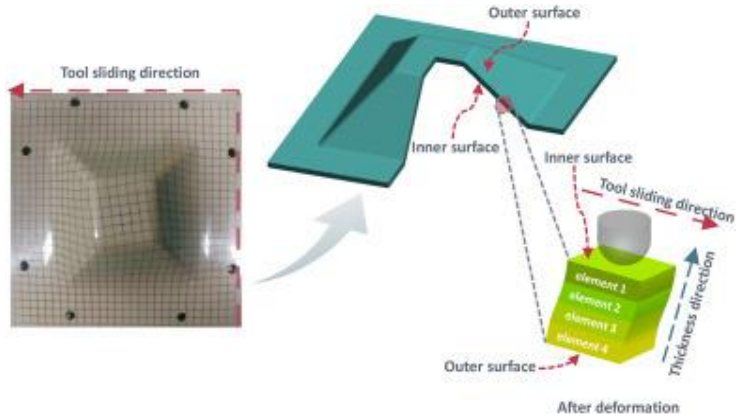

Fig. 1.30 Shear deformation of the formed part [55]

Recently widely used sandwich panels are an excellent heat-insulating material covered between two sheets of rigid shells, but their manufacture and use are limited by the required expensive tools. The paper [56] proposes the SPIF process as a mechanically feasible alternative to the formation of multilayer panels. The structure consists of two rigid outer plates separated by a lightweight material core that provides a higher stiffness-to-weight ratio than the monolithic material of equivalent dimensions, as shown in Figure 1.31. In addition to saving weight, they absorb vibrations, sound and shocks, and ensure buoyancy.

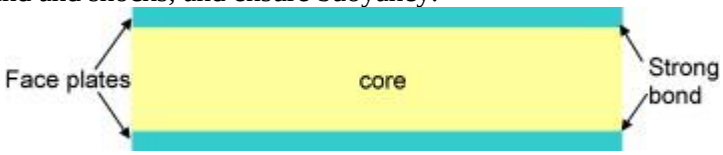

Fig. 1.31 Sandwich plate construction scheme [56]

The methods used to heat the entire polymer sheet are slow and inefficient as they require additional means to retain their deformations; more efficient spot heating tools are not being developed whose use would – in some cases – replace the expensive 3D printing technologies.

Conclusions of the chapter

The analysis of research publications assessing the outstanding issues mentioned in the review allowed to identify the aim and objectives of the dissertation.

The aim of the research is to investigate and develop robotized metal and polymer sheets single point incremental forming and to predict the technological parameters by machine learning algorithms.

To achieve this aim, the following objectives have been set:

1. To theoretically investigate the sheet metal forming limits under stretch-bending conditions and dynamic characteristics of a robotized process;
2. To validate and apply the developed and patented robotized environmentally friendly metal sheet incremental forming technology;

3. To perform comparative analysis of machine learning algorithms for predicting the effect of force on the robotized forming;
4. To theoretically and experimentally investigate the robotized polymer sheet single point incremental forming technology and to develop an efficient polymer heating method.

II. METAL SHEET SINGLE POINT INCREMENTAL FORMING INVESTIGATION

Introduction

A number of parameters relating to the SPIF technological parameters, such as the friction phenomena and material conformability, are involved in the metal forming process. These effects have not been sufficiently studied yet, especially with the use of metals. This work is part of an extended study to be conducted in the future. It attempts to pre-estimate sheet strains and stresses regarding aluminum alloys SPIF process. An *LS-Dyna* environment was created for the FE modeling of this process. This study proposes a new idea to reduce the friction force between the aluminum alloy sheet surface and the forming tool by using ultrasonic vibrations excitation with high frequency oscillations in the orthogonal direction induced by piezo-transducers clamped to the frame. The process improvements, such as a quick turnaround to market as well as the environmental friendliness of the process by substituting the usage of oil with vibrations has been achieved. A comparison of the friction coefficient for different forming methods has shown no significant difference between forming when the surface is lubricated and when the material is using vibrations. In order to analyze the plastic deformations, a mathematical model using numerical FE has been created.

2.1. Evaluation of friction interaction between the tool and sheet surfaces

In order to derive the frictional force between the aluminum alloy sheet and the tool (Fig. 2.1, a), the calculation diagram is presented in Fig. 2.1, b.

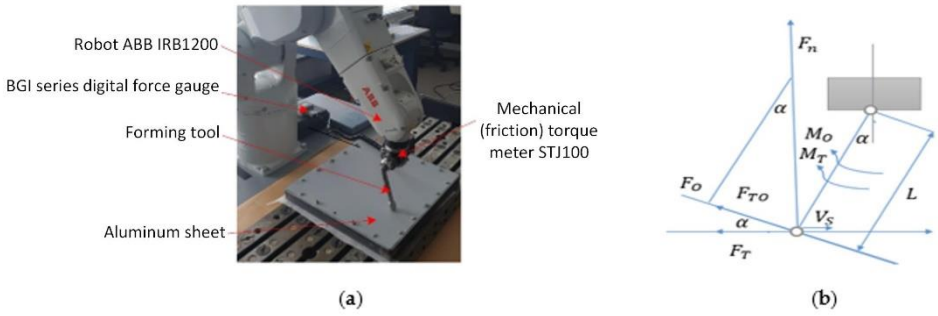

Fig. 2.1 Derivation of the friction force during the forming process: (a) experimental setup, and (b) mathematical scheme

To determine the pressure and friction torque, a roughness torque gauge was placed at an angle of 30°. The friction force was calculated according to the following formulas:

$$F_T = k_T F_N , \tag{2.1}$$

$$F_{TO} = F_T \sin\alpha , \tag{2.2}$$

$$M_O = F_O L , \tag{2.3}$$

$$F_N = \frac{F_O}{\sin\alpha} , \tag{2.4}$$

$$M_O + M_T = \left(F_O + F_{TO}\right) \cdot L . \tag{2.5}$$

where α is the angle between the surface of the material and the tool (30°); L is the length of the tool link connecting the sphere and the moment gauge (150 mm); M_0, M_T is the pressing force of the tool and the tool friction force generated angular momentums; F_0, F_{T0} is the pressure force of the tool and the friction force projection to the tool's link; F_N, F_T is the tool's sphere pressure and the friction force; v_s is the sphere movement speed of a steel tool on the surface of the analyzed sheet (mm/s); k_T is the friction force coefficient between the steel tool sphere and the sample sheet.

2.2. Dynamic analysis of sheet metal

The metal materials that are used in the *single point incremental forming process* have visible deformations when they are being contacted with the tool. The main difficulty of the SPIF process is to develop an easy way to evaluate the forming force components. Forces that are effective in the SPIF process can be impacted by altering the coefficient of friction between the material being formed and the forming tool. One of the most common methods to reduce the friction between the material and the tool in the contact area is the use of lubrication; however, the use oil has been proven to exert a negative impact on the nature. Hence, discovering an alternative which would minimize the forming forces that are related with the SPIF process dynamics is needed. In order to reduce the forming forces, a SPIF process, where the mechanical properties could be easily altered in the experiments when 3D scanning device from Fig. 2.2 is being used, needs to be created.

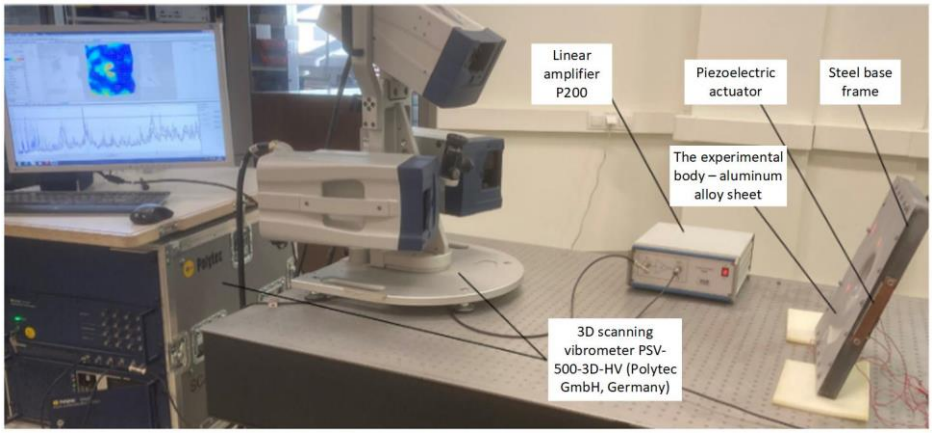

Fig. 2.2 Experimental setup for the analysis of vibration modes of an aluminum sheet

During the experiments, a 300x300x0.5 aluminum alloy *AW1050* sheet clamped to a 30x30 mm steel frame was used for the forming process. A finite element method from the *Comsol Multiphysics* software was used in order to derive the frequencies of the resonant modes. In order to substitute the material surface lubrication while using oil, the idea vibration so that to excite the surface of the material with 3D ultrasonic vibration was tested. To achieve this goal, the schematics of the experimental setup provided in Fig. 2.3 have been developed.

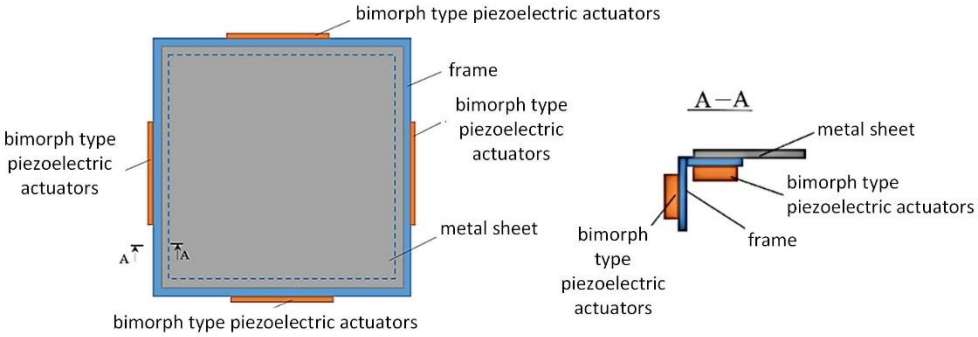

Fig. 2.3 Equipment setup for the excitation of ultrasonic 3D vibrations in the sheet

The experimental setup consists of an aluminum alloy sheet *1* clamped to a metal frame *2* which has an angled profile. Bimorph piezoelectric actuators are glued to the *3* and *4* positions of the frame on either side. The position where the piezoelectric actuators are being placed allows to create excitation of bending oscillations of the higher harmonics in the frame. As the frame is being excited, while the material is being clamped to it, the vibrations of the frame are exciting the aluminum alloy sheet as well. This method based on the aluminum alloy sheet being excited with ultrasonic 3D vibrations reduces the friction force between the sheet surface and the forming tool during the SPIF process. Reduced friction can have a positive impact on the lubrication conditions at the contact point, and, in some

instances, this allows completely eliminating the use of oil for the lubrication purposes. It is possible to use 8 piezo transducers on the metal frame to excite 3D vibrations in the aluminum sheet based on the scheme provided in (Fig. 2.4) by passing harmonic ultrasonic frequency electrical signals. In the experiment, the examined aluminum sheet is pressed against the frame excited by the piezoelectric transducers. Vibrations for the piezoelectric transducer are generated by using a power amplifier. The tool which is embedded in the robot hand is used to form the material with the movements of a robot hand. The tool is intentionally placed at a 30° degree angle, so that it would be possible to calculate the friction momentum and pressing by using the *BGI Digital Force Gauge* with the torque sensor *STJ100*. The gauge is connected to the *Sensor Controller Keyence LK G3001P* which is connected to the *Oscilloscope* which provides the outcomes to the computer screen.

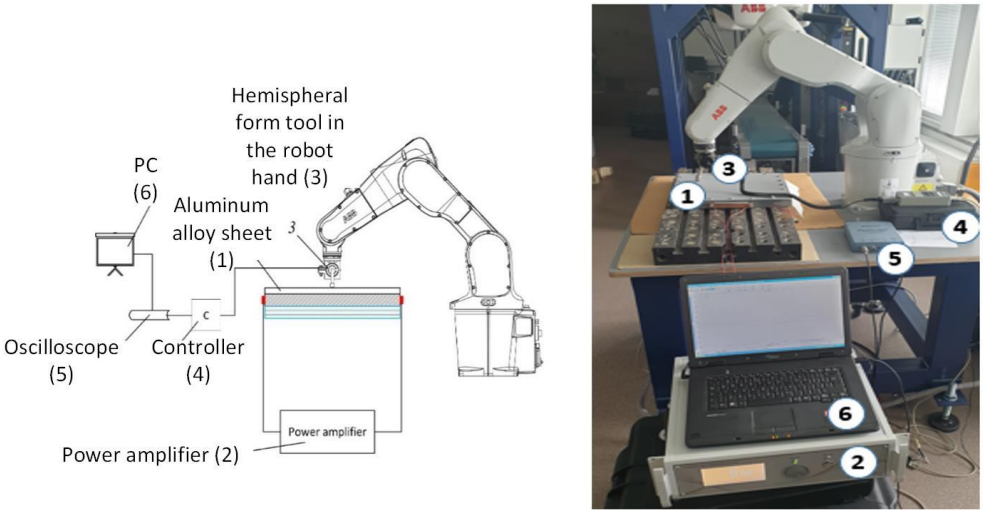

a) **b)**

Fig. 2.4 Experimental setup for sheet excitation

Experiments were being done on a 0.5 mm width aluminum plate. The analysis of vibrations was done by using a *Polytec* scanning vibrometer *PSV-500-3D-HV*. The results showed the friction force at the contact of the surface, and the forming tool is reduced most of all when the piezoelectric actuators are excited in the range from 25 to 35 kHz. The analysis of vibrations was done by using a *Polytec* scanning vibrometer *PSV-500-3D-HV*. Planar higher harmonic vibrations on the X and Y axes are dominant in this frequency range; they are not that easily suppressed when the tool contacts the material compared to the vibrations that are perpendicular to sheet surface vibrations on the Z axis (Fig. 2.5). As a result, when piezo actuators can be excited in the range of 30 to 33 kHz, oscillations are created on the X and Y axes.

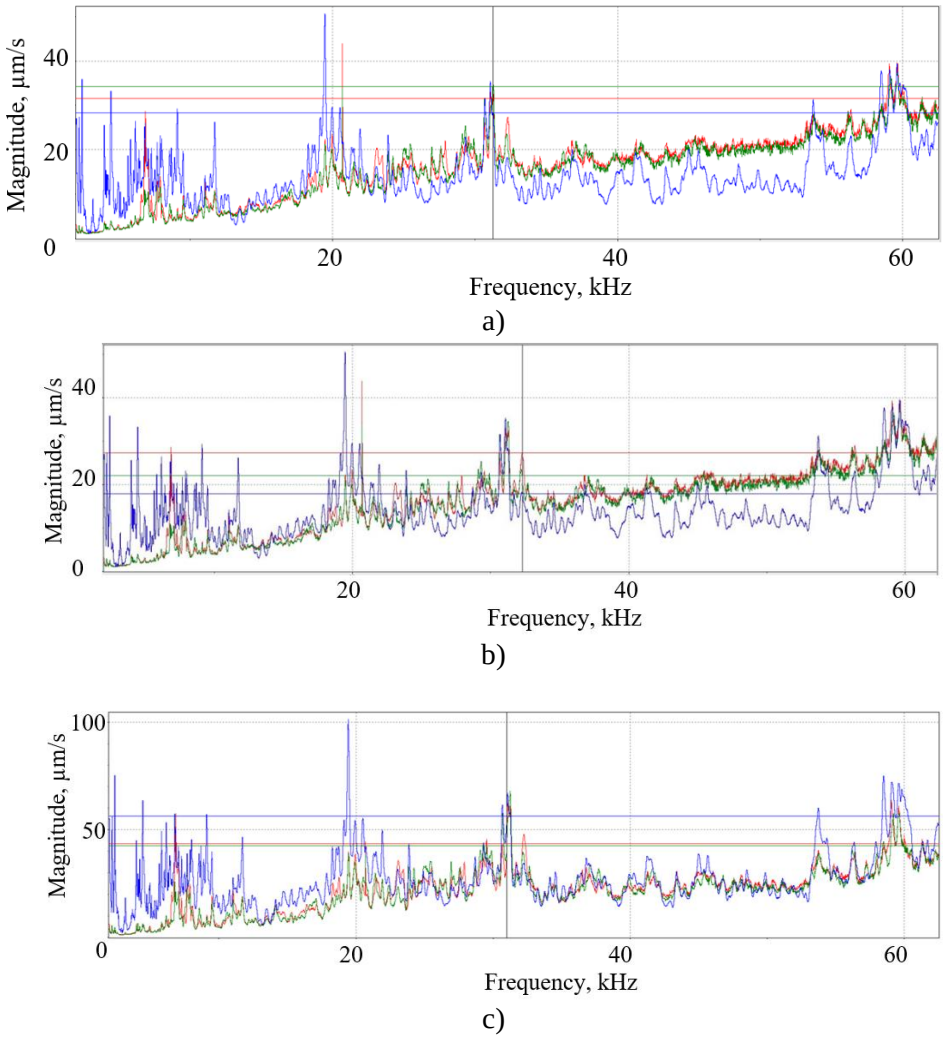

Fig. 2.5 Amplitude dependency from the frequency of the aluminum alloy sheet measured with *Polytec* 3D scanning vibrometer in the frequency band from 2 kHz to 60 kHz after excitation of two attached piezoelectric actuators (according to Fig. 2.4): (a) actuator *4* is excited, (b) actuator *3* is excited, (c) both actuators are excited, where *X* (red) and *Y* (green) are plane vibrations, *Z* (blue) represents the vibrations in the perpendicular direction to the sheet

When the tool is moving, deformations to the material are being created during the SPIF process. Therefore, the frequencies and amplitudes of the eigenmodes of this sheet are impacted by the forming depth of the tool's position. During the experiments, the influence of the tool located on the bottom and on the side (Fig. 2.6) of the sheet was being analyzed.

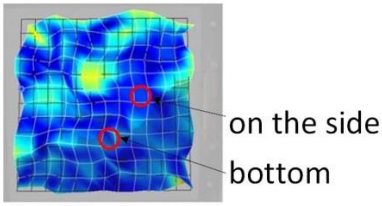

Fig. 2.6 Positions of the forming tool

As it is shown in the vibrograms (Fig. 3.3), regardless of the forming depth and location of the tool, the amplitude of the vibrations of the Z axis eigenmodes that are perpendicular to the surface of the sheet has a lower impact on the surface of the material, while the impact of the amplitudes on the X and Y axes on the 2D plane is most significant.

The results confirm that the ultrasonic excitation on the horizontal plane has a significant effect to the SPIF process.

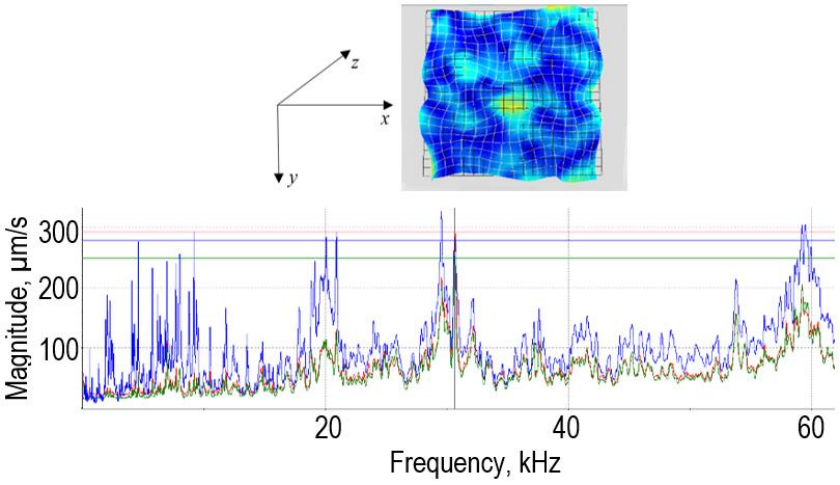

a)

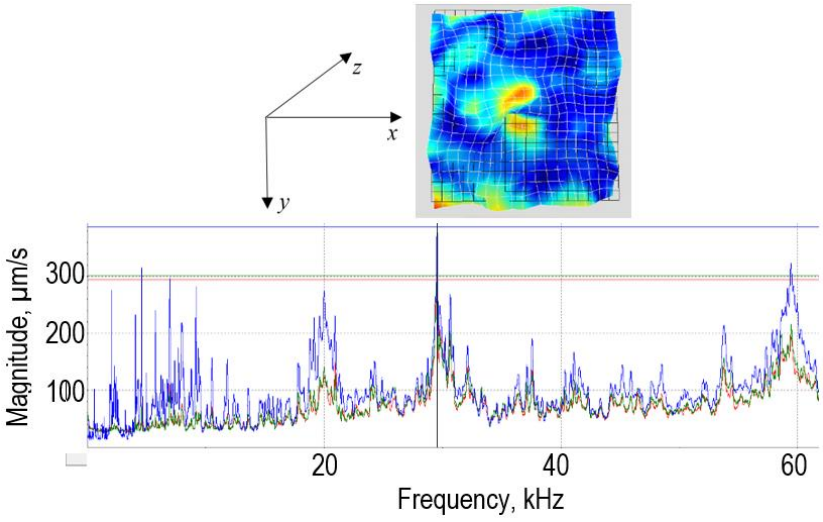

b)

Fig. 2.7 Impact of the forming depth and the tool location on the eigenmodes of the material: (a) tool located in the bottom position and (b) tool located on the side

The outcome of the friction force and the tool friction coefficient was registered when forming was being done on lubricated with oil, dry and ultrasonically excited surfaces within the range from 30 to 33 kHz, which reduces the friction force at the tool-workpiece metal contact pair. The outcome data is presented in Table 2.1.

Table 2.1 Friction coefficient and friction force comparison

Method	Friction Force	Friction coefficients
Without oil lubrication and vibration	3.2 N	0.5
With oil lubrication	1.6 N	0.1
With vibration	1.9 N	0.12

The experimental results from Table 2.1 prove that the coefficient of friction between the metal sheet and the forming tool is almost the same when the forming is done with lubrication on the surface with oil and when forming is done when the surface is excited with ultrasonic vibrations. Substituting oil with vibrations not only creates a forming process which is environmentally friendly, but it also speeds up the process as well because no cleaning of the material surface is needed after the forming process has been completed. The forming method using vibrations has been patented.

2.3. Mechanical testing of the material

In order to define the SPIF process, it is essential to understand the mechanical parameters, such as the cyclic bending and unbending, bending under stress, and the shear deformation process, as well as some other aspects. SPIF has higher forming limits compared to the traditional forming processes, such as stamping. The features that mainly affect the forming process are the drawing angle known as the step down,

sheet thickness, the tool size, and the properties of the material. Multiple sources suggest that, in order to increase the formability of the sheet, the size of the tool, the sheet thickness, and the step down per revolution should be decreased, while the change in the feed rate should not have high impact on the forming process [57]. In order to predict the fracture of the sheet, it is suggested to use the strain-based forming limit curve criterion. This criterion may be applied only when forming is done with the linear strain path [58]. However, if the strain path is not linear, using the strain-based forming limit criterion could lead to false failure predictions and incorrect assumptions on the formability of the material. Strain path changes do not impact the stress-based forming limits; they are rather used to portray the fracture limit with the necking limit based on the criterion of the maximum shear stress [59]. FE analysis was used to derive the stress state, the strain path, and the prediction of formability. In order to create a valid mathematical model for SPIF, multiple tests with different experimental setups were performed. First of all, the cupping test was done in order to calibrate the experimental results with the model. Secondly, the material model created in the previous step was reused for the SPIF simulation. With the aim of defining the plastic behavior of the ductile fracture of the formed material, the Erichsen cupping test was carried out based on the Standard *ISO 20482: 2013* (Metallic materials – Sheets and strips – Erichsen tensile test) on square aluminum plates. The Erichsen cupping test is used to determine parameters for fracture under the equi-biaxial state of stress. The point where the stress is highest is based on the apex of the dome when the parameters of the circumferential and radial strain and stress have the same value. The most important mechanical feature derived from the Erichsen cupping test is Erichsen Index (IE) which represents the depth of the sphere at the maximum force which can be used to define the plasticity of the material. The outcomes are impacted by the friction between the material's surface and the forming tool and the sheet thickness. For the Erichsen cupping test, the sample aluminum sheets was used (Fig. 2.8). A simulation was performed with a 10 mm radius forming tool that was hemispherically punching the material at a 5 mm/min speed.

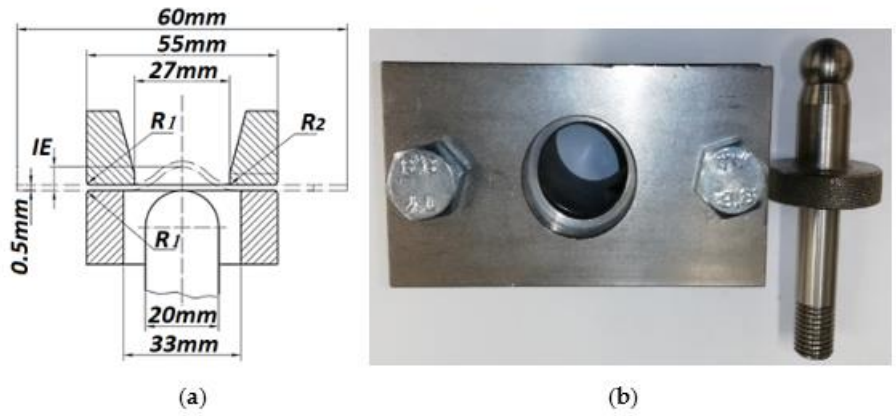

Fig. 2.8 Erichsen cupping test: (a) scheme; (b) test die

The force displacement response was derived from the displacement of the punch vs. the reaction force on the punch plot (Fig. 2.9).

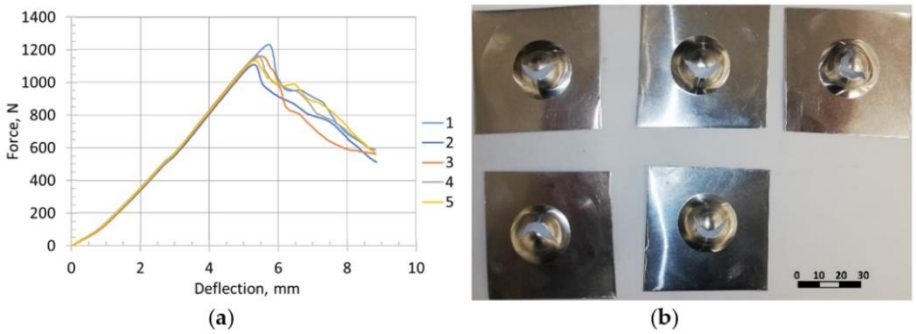

Fig. 2.9 Test results: (a) cupping curves for samples 1–5, and (b) samples 1–5 after the cupping test

During the experiment, the sheet was punched by using a hemispherical punch until a crack was visible, while deriving the depth of the cup as indicated by the circular scale at the same time. A stronger metal made from fine grain would have a fine shape of the cup and a flatter depth. However, a softer metal that is denoted by a coarse grain size would have a rough cup shape and a more prominent depth. 5 tests have been run with the results for the maximum load force. Testing was done with an aluminum alloy *EN AW1050A H24* sheet with a thickness of 0.5 mm. The mechanical parameters of the material of the sheet are listed in Table 2.2.

Table 2.2 Aluminum alloy *EN AW1050A H24* mechanical properties

	Modulus of elasticity, GPa	**Proof stress, MPa**	**Tensile strength, MPa**	**Elongation A, %**	**Strength coefficient K, MPa**	**Strain hardening coefficient n**
Data Sheet Values	71	>85	105–145	3–8		
Range for curve fitting				2 ÷ 40	140 ÷ 200	0.05 ÷ 0.2
Calibrated values LS-Opt & LS-Dyna				37.9	143	0.097

The Power-Law material model was used to define the relationship between the strain and the stress (Fig. 2.10). The *LS-Opt* software was used to derive the Power-Law variables, such as the failure strain, the hardening exponent *n*, and the strength coefficient *K* from the material's properties (the failure strain, the ultimate strength range, and the yield stresses). The stress and strain graph obtained as a result of the numerical simulation is shown in Figure 2.10.

$$\sigma = K\varepsilon^{n} = 143\varepsilon^{0.097}\,. \tag{2.6}$$

where ε is uniaxial strain.

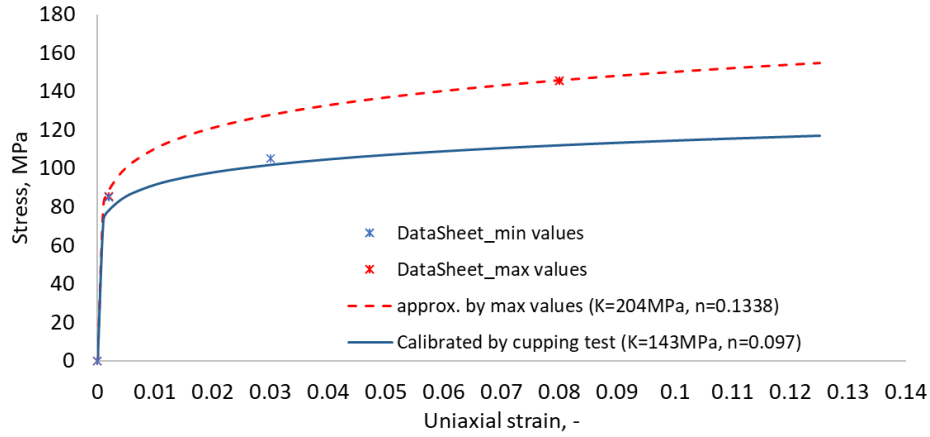

Fig. 2.10 Stress vs. strain relationship of the Power-Law model (the dashed curves represent the min and max range for the calibration of the material model; the solid line represents the calibrated Power Law function)

Even though the fracture strain directly depends to the stress state [60, 61], the value calculated in the uniaxial test could be different from the failure strain derived in the cupping test where the biaxial tension is dominates. The fracture strain is larger during the cupping test, if compared to the uniaxial tensile test. However, the strain path is non-linear when the incremental forming process is being applied [61]; as a result, both the uniaxial failure strain as well as the conventional forming limit plot criterion may impact failure prediction inaccuracies.

In order to create the stimulation of the cupping test and to validate the material model FE method, the *LS-Dyna* software was used. Four steps were run during the FE model: (1) a deformable aluminum sheet, (2) a rigid spherical punch, (3) a bottom holder, (4) a top holder. At the beginning of the modeling, a force of 10kN was used to compress the holders. Shell elements with 5 integration points through-thickness and a shear correction factor of 0.833 were used to model the aluminum sheet material model. The size of the shell elements that was used for the material model was 0.5–1 mm. The FE model (Fig. 2.11, a) given bellow consists of approximately 8500 or 5000 shell elements, respectively. To describe the contact between the aluminum sheet and the punch the keyword: **CONTACT_FORMING _ONE_WAY _SURFACE_TO_SURFACE* was used. The punching was done at a 1 m/s speed. The Power Law_Plasticity material model was used to describe the properties of the aluminum sheet. The following three parameters were used for the calibration: the failure strain ε_u, the strain hardening coefficient n, and the strength coefficient K. The results of the simulation are provided in Fig. 2.11.

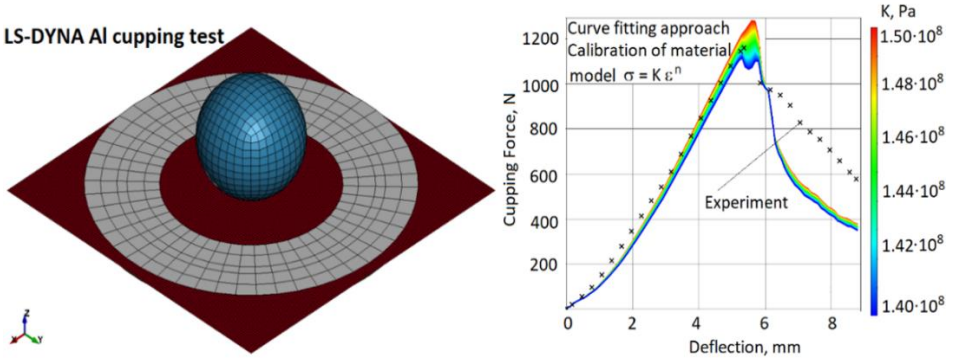

a) b)

Fig. 2.11 Cupping test model: (a) numerical model of the cupping test; (b) relationship between the force and displacement of the cupping experiment and the sensitivity of the simulation results to the strength coefficient *K* of the calibrated Power-Law material model (Strain hardening coefficient $n = 0.097$ and failure strain $\varepsilon_u = 0.38$)

After the curve fitting was done, the relationship between the force and displacement and the FE simulation prediction (Fig. 2.11, b) exhibited good correlation. The spherical punch deformation into the tested sheet is presented in Fig. 2.12. What is more, after comparing the fracture paths, it is visible that they are similar (Fig. 2.9, b, and Fig. 2.12). The fracture lines are almost symmetrical with a position between the corners and the center. However, during the experiments, only three diagonal fracture lines are present, while four lines are observed during the simulation. The difference in the number of the fracture lines may get manifested because of the anisotropy of the material.

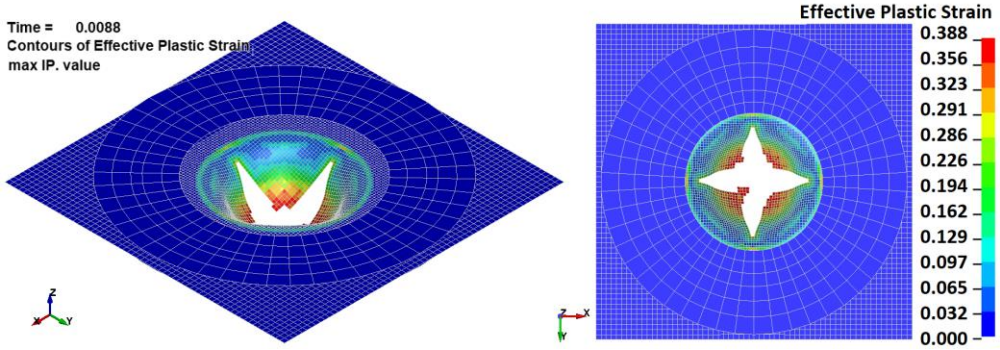

a) b)

Fig. 2.12 Simulation results obtained by Erichsen test: (a) isometric view, and (b) view at the sheet bottom

2.4. Investigation of the deformability of metal sheet

The comparison of the theoretically and experimentally obtained results of ultrasonically excited sheet dynamics are provided in Fig. 2.13 which show that the

frequency of the first mode for the theoretical model is 81.707 Hz, while the experimental value is 78.8 Hz, which is essentially the same.

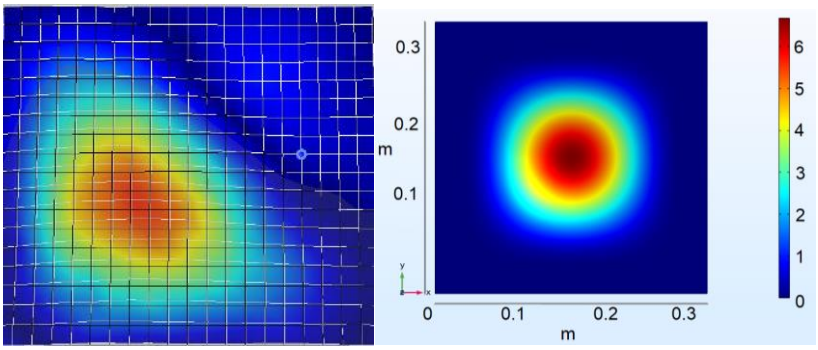

a) b)

Fig. 2.13 First modes of transverse oscillations of an aluminum alloy sheet mounted to a steel frame: (a) 1st mode at a frequency of 78.8 Hz, and (b) 1st mode at a frequency of 81.707 Hz

The SPIF process was modeled by using the FE method from the *LS-Dyna* software. There were two parts used in the model of the forming process: a forming tool and an aluminum sheet (Fig. 2.14). The forming tool was added to the model as a 20 mm diameter body (circle). The aluminum sheet model was reused from the cupping test model, i.e., integrated shell elements were used, 5 integration points through the thickness were added, a thickness stretch allowed linear variation of the strain through the thickness, and a shear correction factor of 0.833 was used. 20000 shell elements were used in the FE. The main variables used for the FE method were reused from the cupping test. The elasto-plastic features of the sheet material were defined by using the Power Law plasticity material model. The contact definition between the tool and the sheet was also reused from the cupping test model. The aluminum sheet holder was simulated with fixed nodes (25 mm wide around all 4 edges). The major diameter of the helix was 140 mm.

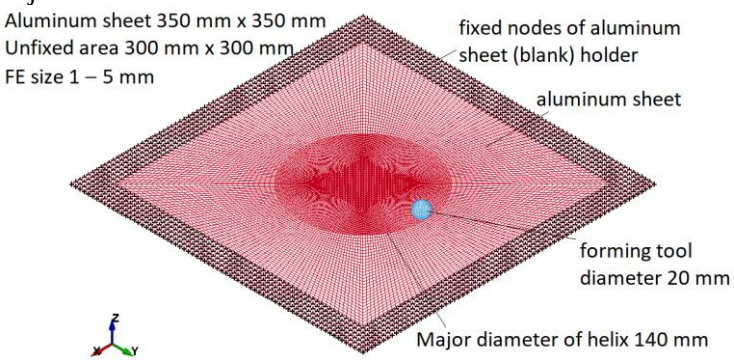

Fig. 2.14 SPIF simulation model

3 continuous functions of tool displacements were used to define the load: f(x), f(y) and f(z). All the functions had a variation of 0.5 mm horizontal and vertical

displacement per revolution. 2 m/s speed was used to define the tool movement. Fig. 2.15 shows the trajectories of the forming tool-path.

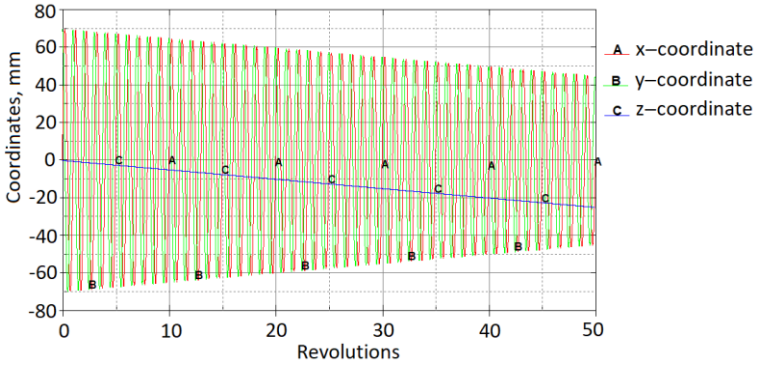

Fig. 2.15 Displacements of loading curves in the *XYZ* directions

Multiple simulations were executed by changing the friction coefficients from *0* to *0.5*. The simulation results are provided in Fig. 2.16 which shows the *X* force component dependence from the number of tool revolutions.

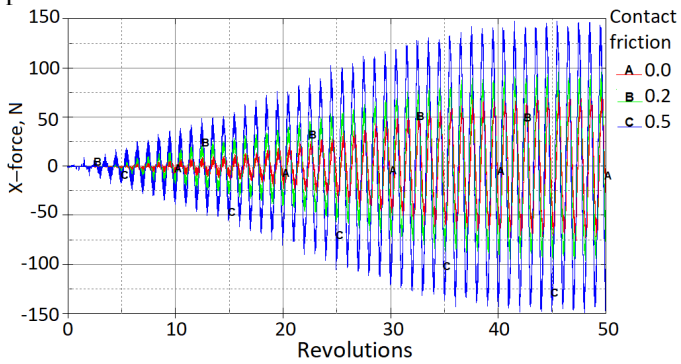

Fig. 2.16 Rotations vs. X-contact force with different friction coefficients at the contact

In comparison, there is no significant impact on the vertical *Z* force component (Fig. 2.14, a). The influence of the friction on the resultant force is presented in Fig. 2.17, b.

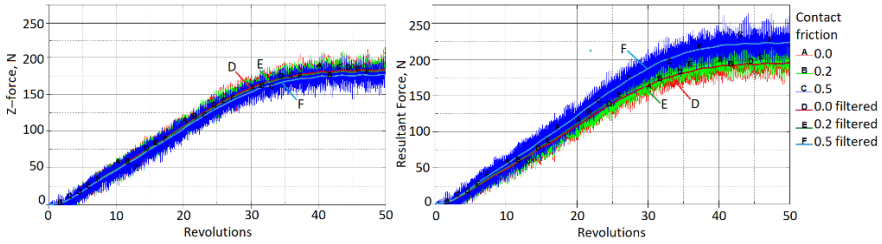

a) b)

Fig. 2.17 Rotations vs. contact force: (a) z-force (vertical force); (b) resultant force

After the SPIF process has been completed, the reduced thickness of the formed material wall is expected. With each SPIF iteration, the thickness of the material is reduced, and it can be defined through the thickness reduction ratio which directly impacts the forming limit. It is important to be able to predict the thickness of the deformed zone so that the thinning ratio could be defined. The shell thickness reduction results during the SPIF process for aluminum alloy sheet are shown in Fig. 2.18. The sine law can be used to define the relation between the forming angle α and the wall thickness:

$$t_f = t_0 \sin(90 - \alpha) \tag{2.7}$$

where t_0 is the thickness at the start of the forming process, t_f is the thickness at the end of the forming process, α is the forming angle between the final deformed surface and the initial flat surface.

The forming angle captured in the simulation is 47° at the beginning of the SPIF process; therefore, deriving from the sine law, this would result in the reduced thickness of 0.34 mm. In comparison, the minimum thickness for the simulation was 0.335 mm. Three cases (A, B, C) with multiple forming angles of 47°, 30°, and 17°, respectively, after a forming depth of 25 mm, show the outcome of the thickness reduction. There is a good correlation between the SPIF simulation results and the sine law.

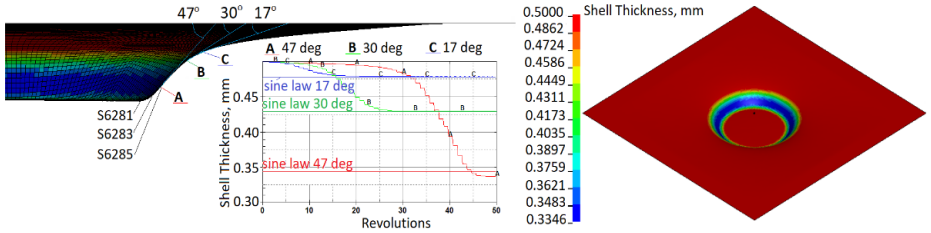

a) b)

Fig. 2.18 Reduction of shell thickness: (a) cases with the forming depth of 25 mm, and the forming angles of 47°, 30°, and 17°; (b) shell thickness distribution after the forming depth of 25 mm

The distribution of the strain when the forming depth reaches 25 mm is presented in Fig. 2.19, a. The forming tool contacts the aluminum sheet at approximately 35 revolutions. As a results, after the material contacts with the tool, the effective strains start increasing significantly (Fig. 2.16, b).

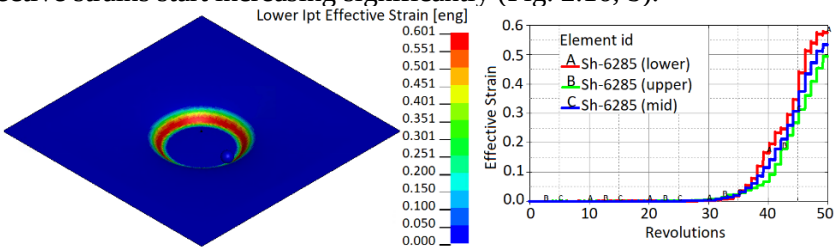

a) b)

Fig. 2.19 Strain distribution: (a) after a forming depth of 25 mm; (b) evolution in finite element

It is visible that, after the start of the SPIF process, the sheet thickness starts decreasing, which correlates with the effective plastic strain changes (Figs. 2.18 and 2.19). One of the main causes of the SPIF process failure is the thinning of the forming sheet which is related to the forming angle α which represents one of the geometrical limits of the SPIF process [62]. As shown in Fig. 2.19, the effective strain values (the maximum effective strain of 60%) are much higher compared to the values from the material data since the tensile failure strain constitutes 3–8%, and the values of the failure strain calibrated by the cupping test make up 38%.

This proves that predicting the failure in the incremental forming process can be challenging as more process parameters should be used to retrieve the correct results. The SPIF cross sections for the aluminum alloy sheet per iteration are presented in Fig. 2.20.

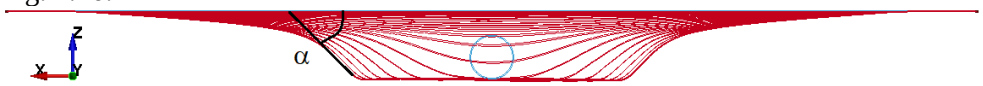

Fig. 2.20 Cross sections of aluminum forming sheet per iteration

In order to compare the evolution of stress triaxialities during the cupping test and SPIF (Fig. 2.21), it should be noted that, during the cupping test, the stress triaxiality is stable and equal to 2/3, which relates to the equi-biaxial tension stress state, while the stress triaxiality during the SPIF process varies from −0.6 to 0.6. This confirms that the stress state during the SPIF process varies from the plane-strain compression up to the plane-strain tension. Throughout the SPIF process, formability can be improved because, at the plane-strain tension state, the failure strain of the material has a lower value compared with the failure strains at the other stress states.

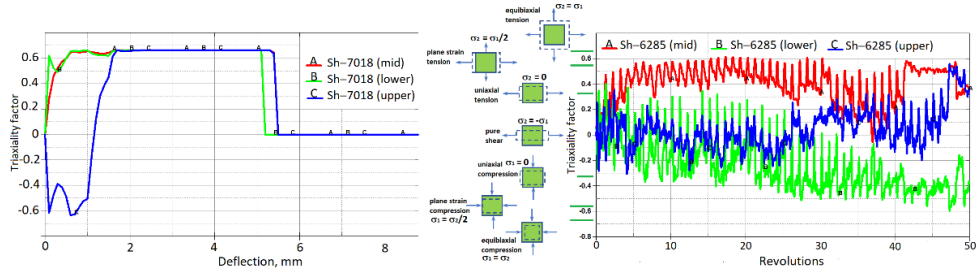

Fig. 2.21 Stress evolutions in contact with tools: (a) cupping test; (b) SPIF process

The deformation issue during the SPIFF process is still not fully clear. As direct experimental evidence is missing, multiple researchers have claimed that deformation is caused by through-thickness shear, while others state that stretching is the main cause [63, 64]. If the out-of-plane shear dominates, the principal strains are not in the plane [65]; as a result, the usage of shell elements could be limited as shell elements usually do not allow obtaining the through-thickness shear properties in the simulation results. If the shell elements are fully integrated with the thickness stretch, the *LS-Dyna* software allows the logging of through-thickness shear strains and shear stresses. In order to evaluate the material behavior regarding the SPIF, 3 elements

(S2681, S2683, S2685; see Fig. 2.18, a) along the *X* axis were chosen. The strain distribution through the thickness is presented in Fig. 2.22.

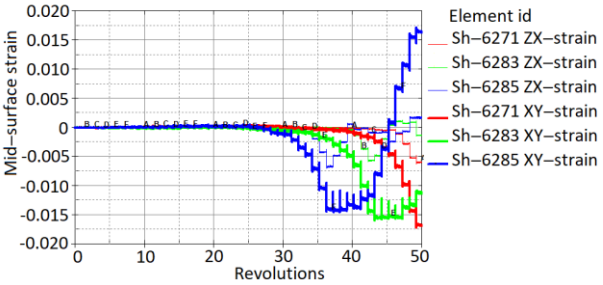

Fig. 2.22 Variation of in-plane and out-of-plane shear strains during the SPIF process

Conclusions of the chapter

1. A method which reduces the frictional force between the sheet surface and the forming tool by using the excitation of the material with ultrasonic oscillations in two orthogonal directions in the sheet plane has been created.
2. A numerical model of the tool-workpiece interaction process has been developed as a non-linear model due to the large plastic deformations of the sheet by the virtue of estimating the boundary conditions occurring between the tool and the sheet at the point of contact.
3. The single point incremental forming process has been modeled by using the explicit FE method in the *LS-Dyna* software which captures through-thickness shear strains and shear stresses as well as punching during the Erichsen test.

III. PREDICTION OF FORMING PROCESS PARAMETERS USING ARTIFICIAL INTELLIGENCE ALGORITHMS

Introduction

By replacing the eco-unfriendly lubrication with oil on the contact surface between the metal sheet and the forming tool, an innovative vibrationally excited metal sheet method is demonstrated. It shows the best modes of the ultrasonic excitation of a metal sheet. An approach which is based on various machine learning (ML) algorithms was used to predict the SPIF process forces. The input features that are related to the process parameters, mechanical features, and the sheet thickness were considered. Given the assumption that the input function variability can be defined by using the normal distribution, the sample dataset was produced. The ability to apply machine learning methods in an industrial environment stems from their ability to find the balance between the variance and the model bias and their actually good performance.

3.1. Materials and methods

The metal materials that are used in the SPIF process have visible deformations when they are being contacted with the tool. The main difficulty of the SPIF process is to have an easy way to evaluate the forming force components. Forces that are effective in the SPIF process can be impacted by changing the friction coefficient between the material being formed and the tool. One of the most common methods to reduce this friction is by using lubrication. However, such a lubricant as oil has proven to exert a negative impact on the nature. Hence, discovering an alternative which would minimize the forming forces that are related with the SPIF process dynamics is needed. In order to reduce the forming forces, a SPIF process where the mechanical properties could be easily altered in the experiments when the 3D scanning device from Fig. 3.1 is being used needs to be created.

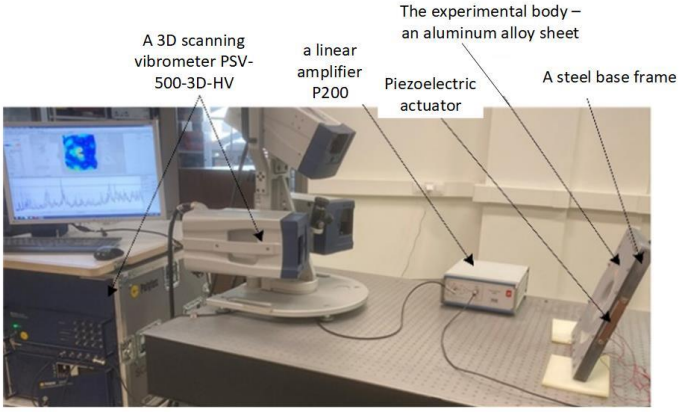

Fig. 3.1 Experimental setup for the analysis of vibration modes of an aluminum sheet

3.1.1. Experimental analysis of aluminum sheet dynamics

As the aluminum alloy sheet is being formed by using the tool movements, deformations are created; therefore, the forming process parameters exert great influence on the frequencies and amplitudes of the material's eigenmodes. In order to better understand this impact, the ultrasonically excited aluminum sheet experiments have been carried out for two locations of the tool (Fig. 3.2).

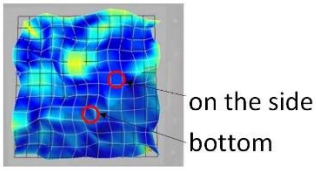

Fig. 3.2 Measurement points on the vibrating sheet surface

As it is shown in the vibrograms (Fig. 3.3), regardless of the forming depth and the location of the tool, the amplitudes of the vibration eigenmodes in the perpendicular to sheet surface direction (the Z axis) had a lower impact on the surface

of the material, while the impact of amplitudes in X and Y axis directions on the 2D plane were most significant.

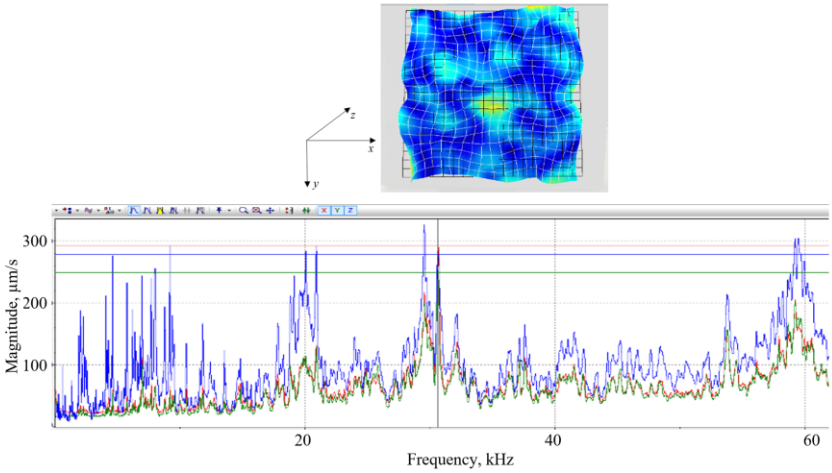

a)

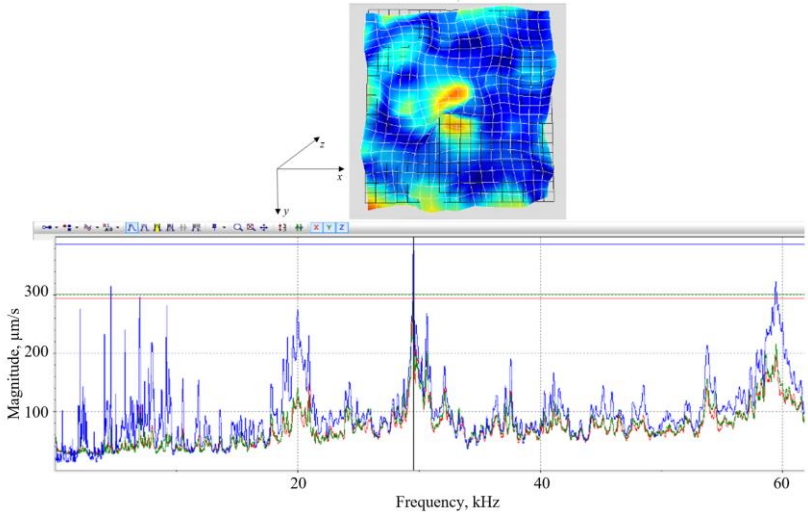

b)

Fig. 3.3 Amplitude-frequency characteristics of an aluminum alloy sheet excited in the frequency range of 0.5 to 60 kHz: X (red) and Y (green) are lateral vibrations, Z (blue) is the normal direction, respectively: (a) tool on the bottom and (b) tool on the side

Excitation of the material with the frequency between 28 to 36 kHz, when the amplitudes in the XY axis are dominant compared to the Z axis vibrations, proved to be the most efficient strategy during the experimental analysis. It was proven that ultrasound vibrations improve the forming process by significantly reducing technological friction on the aluminum alloy sheet. In addition, the usage of ultrasonic vibrations has made it easier for the tool to move on top of the sheet surface. There

are numerous examples and researches where ultrasonic vibrations are used to reduce the friction in metal-to-metal contacts. Vibrations make the stick phase of the contact vanish, while causing the sliding effect during contact. The force that is required to create movement becomes close to zero when the macroscopic velocity of the contact partners becomes smaller compared to the vibration velocity. These results confirm that ultrasonic excitation of the material on the 2D plane has a high impact on the effectivity of the forming process. The mechanical properties of aluminum alloy AW1050 that was tested in this study are provided in Table 3.1.

Table 3.1 Mechanical features of aluminum alloy *AW1050*

Mechanical Property	Value	Unit
Density	2,71	kg/m3
Electrical Resistivity	0.282x10-6	Ωm
Elongation A	12 Min	%
Hardness Brinell	34	HB
Melting point	650	°C
Modulus of Elasticity	71	GPa
Proof stress	85 Min	MPa
Tensile strength	105–145	MPa
Thermal Conductivity	222	W/mK
Thermal Expansion	24x10-6	/K

3.1.2. Experimental analysis of robotized incremental aluminum alloy sheet forming

In order to create the process where the forming force could be easily controlled and predicted, ultrasonic vibrations were used to excite the aluminum alloy sheet. An experimental setup developed for evaluating the forming force is presented in Fig. 3.4. The aluminum alloy sheet is ultrasonically excited in two orthogonal directions on the sheet plane. The vibrations of the transducers are being generated with the power amplifier 2. The robot's hand is used to move the tool which has the sphere at the end which is used to form the material. In order to be able to measure the friction momentum and pressing, the tool is intentionally mounted at an angle of 30° degrees, with the Mechanical momentum sensor *STJ100* 3 which is connected to a controller *BGI 4* (*Mark-10 Corp*., USA), The results received by the mechanical moment sensor are transmitted through the sensor controller BGI which is connected to the oscilloscope *PicoScope 3424* 5 (*Pico Technology Ltd*., UK) and the computer (6).

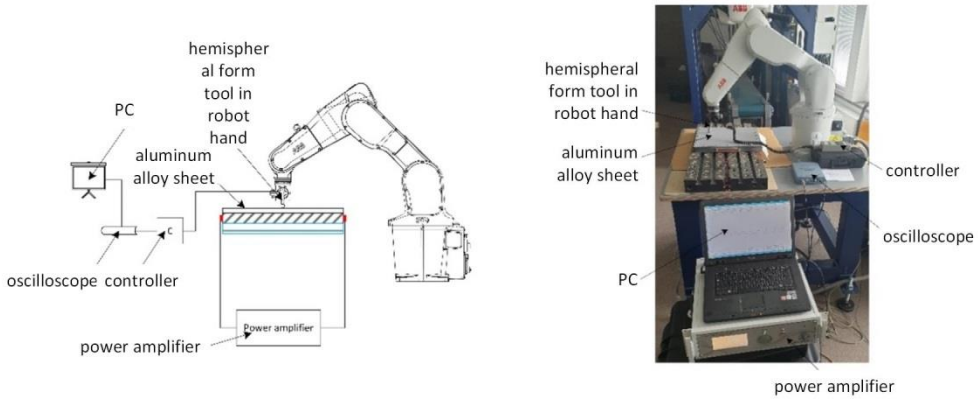

a) b)

Fig. 3.4 Experimental setup for metal sheet vibrational forming

The input details used to configure the forming process path trajectory are provided in Table 3.2.

Table 3.2 Parameters used to define the path (trajectory) of the forming tool

Parameter	Value	Unit
Forming depth	25	mm
Helix type	Right-handed	-
Lead angle	45	°
Major diameter of the helix	140	mm
Maximum possible depth	2	mm
Minor diameter of the helix	9	mm
Possible step size downwards interval	0.1–1.0	mm
Possible step size to the center interval	0.1–1.0	mm
Tool diameter	8.5	mm
Vertical tool path	0.5	mm
Horizontal tool path	0.5	mm
Type of trajectory	Helix – Circle	-

The parameters that are used in the SPIF process for an aluminum sheet are provided in Fig. 3.5.

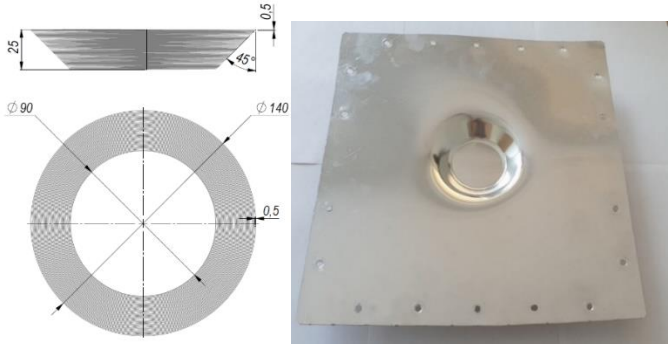

a) b)

Fig. 3.5 Incremental aluminum sheet forming: (a) geometric parameters used in the forming process; (b) output of the material after the forming process

Fig. 3.4 shows the experimental setup where a Torque sensor *STJ100* which was connected to the digital force gauge (*Mark-10 Corp*., USA) was used to determine the mechanical friction on the aluminum alloy sheet surface. The torque sensor had the speed rate of the tool 1200 mm/min and a sensitivity factor of 6 Nm/V. The coefficient and the force of friction were measured when the forming was done on the dry surface, for the surface lubricated with oil and with the surface excited with ultrasonic vibrations; the coefficients are given in Table 3.3.

Table 3.3 Friction coefficient and friction force values when using different forming methods

Forming method	Friction Force	Friction Coefficient
Without vibration and lubrication	3.2 N	0.5
With lubrication	1.6 N	0.1
With vibration	1.9 N	0.12

The results in Table 3.3 prove that, when the surface is ultrasonically excited, the coefficient of friction is almost the same as the coefficient of friction of the surface lubricated with oil. Substituting oil with vibrations not only creates a forming process which is environmentally friendly, but it also speeds up the process as well because no cleaning of the material surface is needed after the forming process has been completed. In addition, in order to prove that the material surface after forming is still intact, the surface roughness was measured after incremental forming had been done by using ultrasonic vibrations and without them. To determine the surface roughness, a surface roughness tester *TR200* (*BeijingTIME High Technology Ltd.*, China) was employed. The results after the forming process without using ultrasonic vibrations varies from R_a = 0.30–0.33 μm, and, after forming with ultrasonic vibrations, varies from R_a = 0.18–0.25 μm. The forming method using vibrations has been patented.

3.2. Experimental data exploration

The dataset used for training has to be analyzed in order to determine primarily if the collected training data has no data quality issues which could have impact on the accuracy of the prediction models. Missing values and data outliers have to be

detected as training error-based models where some values are missing may not work with some machine learning methods, or it could produce false predictions. As shown in Table 3.4, two types of parameters are being used: categorical binary and continuous numeric. Data investigation shows that the *Wall angle* and the *Tool end diameter* values are constants; therefore, they have to be removed from the training dataset.

Table 3.4 Collected data input parameters

No.	Input parameter	Value (min, max)	Unit
1	Forming depth	0 ...26	mm
2	Sheet thickness, (Θ,°)	0.5, 0.8	mm
3	Step depth, (Δz)	0.25, 0.5	mm
4	Step width, (Δx)	0.25, 0.5	mm
5	Tool End diameter	20	mm
6	Tool type	not rotating/ rotating sphere on the end	-
7	VFC Dry friction	4.91, 343.35	N
8	VFC Oil lubricated	1.96, 341.39	N
9	Wall angle	45, 45	°
	Output parameter		
1	VFC Vibro excitation	4.91, 338.45	N

where VFC is the Vertical Force Component.

Firstly, when analyzing the collected dataset, it is needed to assure that there are no data quality issues that may reduce the accuracy of the prediction models that are to be built. Finding the missing values and outliers is very important as some models cannot be used if these issues are present, and it could compromise the accuracy of the prediction results if a model is used without any considerations. After analyzing the data, it was proven that there are no outliers present and that all the missing data has been identified and replaced with the actual values for the training data set. After making sure that there are no data quality problems left, the training data set containing 5 input parameters is used in the further processing. A data set contains raw properties that are coming directly from the forming process dataset, along with 1 target variable vertical force component (VFC) with vibro excitation of the sheet (Table 3.5).

Table 3.5 Input and output parameters for the training dataset

Input parameters				
Forming depth	Step depth, (Δz)	Step width (Δx)	Sheet thickness, (Θ,°)	Tool type
Output parameters				
VFC Vibro excitation				

The forming process was done by using 3 different forming techniques – without using any oil, with oil applied on the material's surface, and while using ultrasonic vibration excitation. The vertical force component dependency from the forming depth with the sheet thickness 0.5 is shown in Table 3.6.

Table 3.6 Vertical force dependency from the forming depth and the forming method when the sheet thickness is 0.5 mm

	s=0.5 mm, steps 0.5 and 0.5 mm, velocity varied to 100%		
Forming depth, mm	**Vertical force, N**		
	Vibro excitation	**Oil Lubricated**	**Dry friction**
0	73.58	80.93	98.1
2	79.46	115.76	98.1
4	99.08	100.55	112.82
6	112.82	117.72	116.74
8	137.34	127.04	138.32
10	154.51	141.07	144.21
12	156.96	146.17	159.41
14	161.87	148.33	166.28
16	161.87	149.6	166.08
18	165.79	151.86	167.75
20	166.28	152.35	169.22
22	167.26	152.84	169.71
24	167.75	153.23	171.18
25	168.24	153.33	173.15

As the next step, calculating the correlation coefficients *r* to test the linear dependency between the two parameters is needed. Spearman's correlation coefficients [66] range from *-1* to *1*. When the Spearman coefficient is r=0, it is assumed that the variables are not related to each other. When the Spearman coefficient is close to *+1* or *-1*, the correlation coefficient between the two variables is said to be the strongest. The plus/minus sign of the coefficient shows if the relationship between the two variables is positive or negative, e.g., if r=1, then the analyzed parameters have perfect positive relationship between each other. When the a coefficient is close to *0*, we can assume that the correlation between two variables is weak. After analyzing the results, it was visible that the Step width and the Step depth have the correlation coefficient r=1 between each other because the values of these parameters were the same. It makes sense to skip one of these two features in the training process. To calculate the Spearman's correlation coefficient, Formula (3.1) has been used:

$$r = \frac{\frac{1}{n}\sum_{i=1}^{n}\left(\left(R(x_i)-\overline{R(x)}\right)\cdot\overline{R(y_i)-\left(R(y)\right)}\right)}{\sqrt{\left(\frac{1}{n}\sum_{i=1}^{n}\left(R(x_i)-\overline{R(x_i)}\right)^2\right)\cdot\left(\frac{1}{n}\sum_{i=1}^{n}\left(R(y_i)-\overline{R(y_i)}\right)^2\right)}} \tag{3.1}$$

where $R(x)$ and $R(y)$ are the ranks of the x and y parameters; $\overline{R(x)}$ and $\overline{R(y)}$ are the average ranks.

Results show that the binary variable *Tool type* and the target variable *VFC Vibro Excitation* do not have a high correlation coefficient because this parameter has only two available values (a non-rotating sphere; vs. a rotating sphere); hence, it has to be removed from the training dataset.

The final dataset after the analysis and management of the data quality issues has 6 features received directly from the sources. The final features and their correlation coefficients *r* are described in the Spearman correlation matrix (heatmap) and are shown in Fig. 3.6.

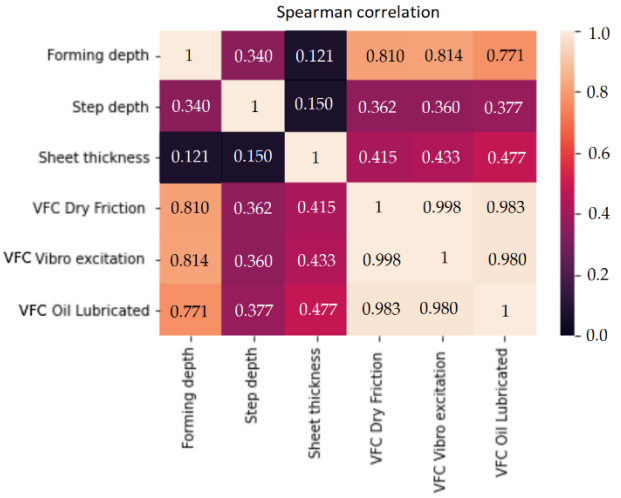

Fig. 3.6 Spearman correlation matrix

The *Results* show that the correlation coefficient of vibrational friction is the most important with the value, r=0.998, while the *sheet thickness* and the *step depth* have medium correlation values r=0.433 and r=0.360. Thus, it makes sense to use 6 input parameters for the training process of VFC prediction.

3.3. Machine learning based prediction

When trying to improve processes in the field of mechatronics, the issue of the lack of experimental data is common. In order to solve the issue of the lack of data, *Machine Learning* (ML) algorithms can be used to predict the variables that are hard to get during the manufacturing processes. The usual machine learning methods (e.g., the decision tree, linear regression, etc.), k-fold for cross-validation [67], feature selection, regularization, ensemble learning, or, the generation of synthetic data [68, 69] are being used to predict the variables. It has been proven by many studies that the *artificial neural network* (ANN) can be used to predict data with a high accuracy level even if a large data sample is not present [70, 71]; in addition, the *Support Vector Machine* (SVM) or *Random Forest* (RF) ML algorithms are being utilized as well. 5 supervised machine learning methods were compared in order to predict the vertical force component for this study: *Gaussian Process Regression* (GPR); *Decision Trees* (DT); *SVM*; *K-nearest neighbors algorithm* (KNN), and *ANN*, which had the highest accuracy (based on the Root Mean Square Error (RMSE)) (Fig. 3.7, a), however this method has the lowest efficiency as its training time is the slowest. After performing the *k*-fold cross-validation procedure, it is visible that the RMSE values have no significant difference compared to each other. What is more, it is visible that the

accuracy of the ANN and GPR ML models is almost the same, but it takes significantly longer to train the ANN model. On average ANN takes 12.68 seconds to be trained, which lasts longer than GPR (Fig. 3.7, b). The same algorithm could have a shifting training time and accuracy on each iteration, regardless if the training has been done on the same dataset. In order to make the variance, lower hyperparameters of machine learning algorithms have to be tuned.

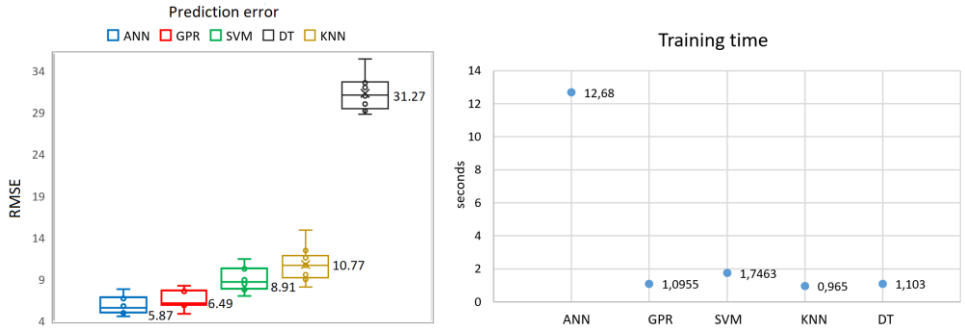

a) b)

Fig. 3.7 Prediction results when different machine learning methods are used: ANN, GPR, SVM, KNN, DT: (a) root mean square error comparison; (b) training time comparison

First of all, in order to start the training of the ML model, hyperparameters have to be set manually. Even though hyperparameters cannot be learned by the predictor itself, they define the training data and are evaluated automatically. Examples of the hyperparameters could be the function and the kernel scale of SVM, or the minimal leaf size in a decision tree. However, weights in the ANN prediction method are model parameters that are derived during the training process. Setting the correct hyperparameters is extremely important as they affect both the performance and the accuracy significantly. Finding the proper values of the hyperparameters can be done by using the hyperparameter tuning algorithms [72]. During hyperparameter tuning, the optimal model is created which has reduced the predefined error value and increased the accuracy of the independent data.

3.3.1. Hyperparameter optimization

During the study, Bayesian optimization was used to tune hyperparameters for GPR, DT, SVM, KNN and ANN models [73]. Hyperparameter tuning could also be done by using the random search or the grid search. The most basic hyperparameter tuning algorithm is the grid search. In theory, the algorithm is supposed to be the best in finding the point in the domain, however, it is not practical to use it as the search is time-consuming and exhaustive. The random search method is superior to the grid search when it comes to performance, as it only checks the randomly selected subset of data, rather than scanning through all the possible variants of the hyperparameter values. Compared to the methods that are using random search over the hyperparameter domain, it has been proven that Bayesian optimization ensures better performance and quality as it involves using the outcomes from the previous iteration to conclude which is the following hyperparameter set to be selected for the

improvement of the model accuracy. This process is a lot more efficient if compared to both the grid search and the random search, and it proves to be best for getting the correct values of the hyperparameters. In order to get the next set of hyperparameter values, the acquisition function is used during the parameter tuning process when the Bayesian optimization method is being applied. Theoretical studies introduce multiple variations of acquisition functions; for instance, the enthropy search, the upper confidence bound, the probability of improvement, the expected improvement, although the final two are used most frequently. Generally, the expected amount of improvement is evaluated by using the expected function:

$$El(x) = E[\max(0, f' - f(x)] \tag{3.2}$$

where $f'min$ is the minimum of $f(x)$; *x*- is the given sampling point.

In order to improve the optimization performance, it has to be assured that both the correctly selected acquisition function and the surrogate model are being used to get the approximation of the main target function. In this study the Gaussian process (GP) is being applied, which is typically the most common choice. Generally, the Bayesian optimization process can be summarized as a sequence having five iterations: (1) acquiring the posterior distribution; (2) choosing the surrogate model; (3) using an acquisition function; (4) adding the additional data to the set of observations; (5) return to step *2*.

During the process of predicting VFC while using the GPR model, four hyperparameters had to be tuned, such as the basic function, the sigma value, the kernel scale, and the kernel function. The most significant hyperparameter in the GPR model is the kernel function as it directly influences almost all of the generalization parameters of the model. In order to define the range sigma value σ, Equation 3.3 is used.

$$\sigma = [\min;\ \max] = [0.0001;\ \max(10 \times \sqrt{\sum_{i=1}^{n} \frac{(y_i - \bar{y})}{n-1}}] \tag{3.3}$$

where $\bar{y}$ is the sample average (the output sample average), y_i is the *i*-th value in the output sample, and *n* is the size of the sample.

The range of the kernel scale directly depends on the kernel function (Table 3.7). In most of the cases, the number of the kernel scale *l* should be the same as the number of inputs for the no-isotropic kernel function. While, for the isotropic kernel functions, the kernel scale l is calculated from a range of values derived from the below-presented Equation (3.4):

$$l = [\min;\ \max] = [0.001(\max(\mathrm{X}) - \min(\mathrm{X}))\,;(\max(\mathrm{X}) - \min(\mathrm{X}))] \tag{3.4}$$

where max (*X*) is the maximum value from the input variable matrix, min(X) is the minimal value from the input variable matrix.

Table 3.7 Hyperparameters of the GPR method

	Sigma	**Basic function**	**Kernel function**	**Kernel scale**
Value Range	[0.0001; 948.39]	Constant; Linear; Zero;	Isotropic and No-isotropic Matern 3/2 and 5/2; Isotropic and No-isotropic Rational Quadratic; Isotropic and No-isotropic Squared Exponential	[0.33943–339.43]

During the study, in order to evaluate the prediction accuracy, three different methods have been used: the Mean Squared Error (MSE), the Root Mean Square Error (RMSE), and the Mean Absolute Error (MAE) [74]. MSE measures the average of the squared difference between the actual values of the target variable and the model predicted target values. The lower is the MSE value, the more accurate the predictions of the model are. RMSE can be expressed as the square root of the MSE, where the main difference is that MSE estimates the variance of the prediction errors, while RMSE estimates the standard deviation of the prediction errors. Same as with MSE, a lower value of the RMSE measure signifies a better accuracy of the predicted model.

$$RMSE = \sqrt{MSE}, \text{ where} \qquad MSE = \frac{1}{n}\sum_{t=1}^{n}|y_t - \hat{y}_t|^2, \tag{3.5}$$

where n is the sample size, y_t is the actual target value at point t, and $\hat{y}_t$ is the predicted target value at point t.

The results of RMSE and MSE may be trivial when large errors are being identified. In comparison, MAE is not as biased for the higher values and most of the time it recognizes larger errors. The lower value of MAE shows that the prediction model is more accurate. MAE can be derived from Equation (3.6):

$$MAE = \frac{1}{n}\sum_{t=1}^{n}|y_t - \hat{y}_t| \tag{3.6}$$

Fig. 3.8 presents the hyperparameter optimization process where the value of MSE is being used to confirm the accuracy of the model. The red dot represents the minimal value of MSE during multiple iterations of the tuning process. Meanwhile, the blue line describes the computed MSE value. The line with the darker blue dots represents the minimal error received during the training process.

$$minMSE = \min\left(MSE^i\right), i = \overline{1,n}, \tag{3.7}$$

where n is the number of iterations.

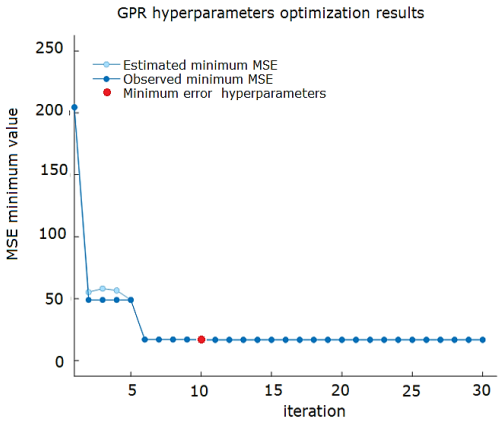

Fig. 3.8 Minimum MSE during the optimization process of GPR hyperparameters

Cross-validation has been done to compare the results of the actual and predicted values of the target variable (VFC). Fig 3.9 presents the cross-validation results where the blue dots represent the actual results, and the red dots represent the predicted

results of the target variable. The errors are depicted by using the vertical red dashed lines; however, as the errors are really small, most of the actual and predicted value points overlap with each other.

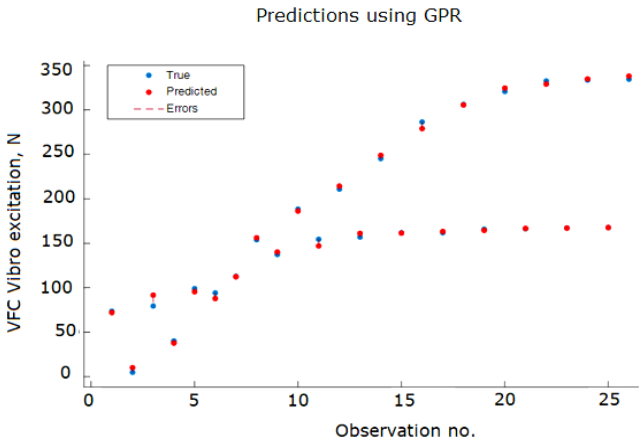

Fig. 3.9 Predicted vs. actual values of the GPR algorithm

The best-scoring candidates $RMSE = 5.6891$, $MSE = 31.238$ and $MAE = 3.872$ have been reached when the linear basic function, the non-isotropic rational quadratic kernel function (Equation 3.8) uses the sigma value of 0.0002.

$$k(x_a, x_b) = \sigma^2 \left(1 + \frac{\|x_a - x_b\|^2}{2\alpha\ell^2}\right)^{-\alpha} \quad (3.8)$$

where σ^2 is the overall variance, ℓis the length scale parameter, α is the scale-mixture ($\alpha > 0$).During the process of predicting VFC by using the SVM model, four hyperparameters have been selected for the tuning process: the kernel scale, the kernel function, the epsilon, and the box constraint (Table 3.8).

The array of the values of the three hyperparameters was chosen according to the experiments. 7 distinct kernel functions have been inspected: Linear, Cubic, Quadratic and 3 Gaussian (medium, fine, coarse. The results have shown that the Gaussian functions had the lowest accuracy compared to the other kernel functions.

Table 3.8 Hyperparameters of the SVM method

	Epsilon	**Box Constraint**	**Kernel function**	**Kernel scale**
Value Range	[0.01; 1000]	[0.001; 500]	Linear, Gaussian, Quadratic, and Cubic	[0.001; 100]

The most accurate prediction outcomes for the training data where RMSE = 9.124, MSE = 83.253 and MAE = 6.403 were reached by applying the function ε=0.105, constraints = 111.25 (Fig. 3.10).

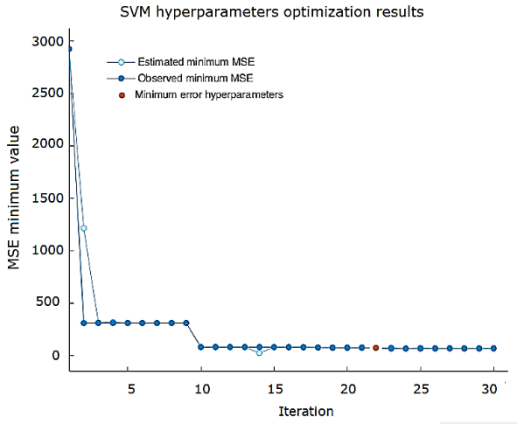

Fig. 3.10 Minimum MSE during the SVM hyperparameters optimization process

The analysis has shown that the minimum MSE depends on the different hyperparameters and can vary over a wide range. There were cases where MSE values almost reached 3000. A comparison of the actual and predicted values is shown in the prediction plot in Fig. 3.11.

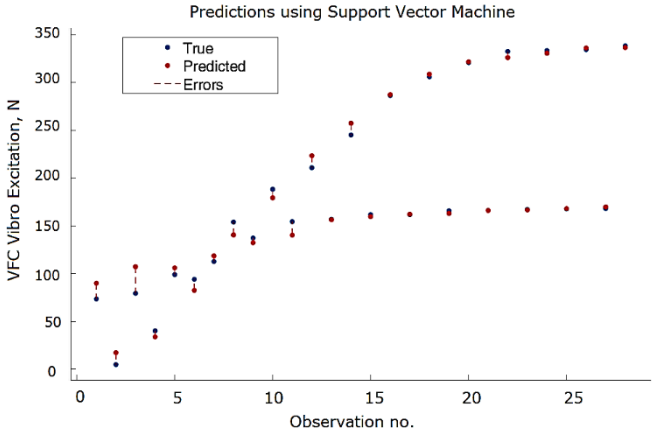

Fig. 3.11 Predicted vs. Actual values of the SVM algorithm

During the process of predicting VFC when using the ANN model a simple feedforward network has been used – the multilayer perceptron (MLP) – as shown in Figure 3.12.

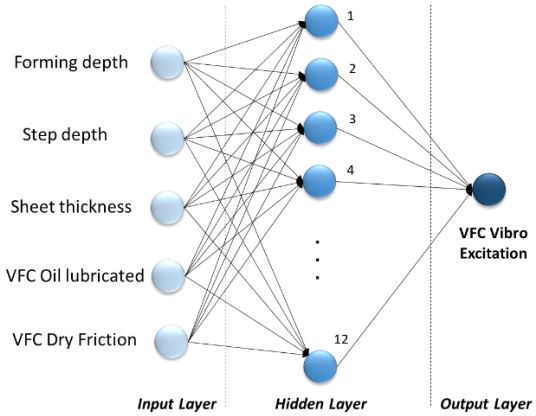

Fig. 3.12 Architecture of the used multilayer perceptron

In order to have accurate predictions, four hyperparameters had to be optimized for the ANN hyperparameter tuning process: the hidden layers activation function, the hidden layer size, the number of the hidden layers, and the strength of regularization (Table 3.9). During the optimization process, the 3 most usually used activation functions were examined: the Hyperbolic tangent (Tanh), the Sigmoid, and the Rectified Linear Unit (ReLU). Primary cross validation outcomes have been used to define the range of the regularization strength. The size of the training data was the main factor when choosing the value ranges of the number of the hidden layers and the size of the hidden layer.

Table 3.9 Hyperparameters of the ANN model

	Number of hidden layers	**Hidden layer size**	**Activation function**	**Regularization strength**
Value Range	[1; 3]	[10; 100]	Sigmoid, Tanh, ReLU	[0; 0.001]

The prediction results using the ANN method have presented the highest accuracy where *RMSE*=4.5337, *MSE*=20.573 and *MAE*=3.528 were received when ANN was used with a single hidden layer while being used with the function ReLU, twelve neurons, and the strength of regularization *0*. The results are shown in Fig. 3.13. The comparison of the predicted target value outcomes with the actual data when the ANN method is being used is presented in Fig. 3.14.

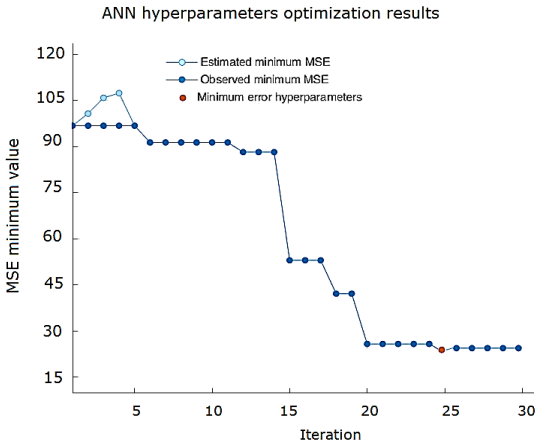

Fig. 3.13 Minimum MSE during the optimization of ANN hyperparameters

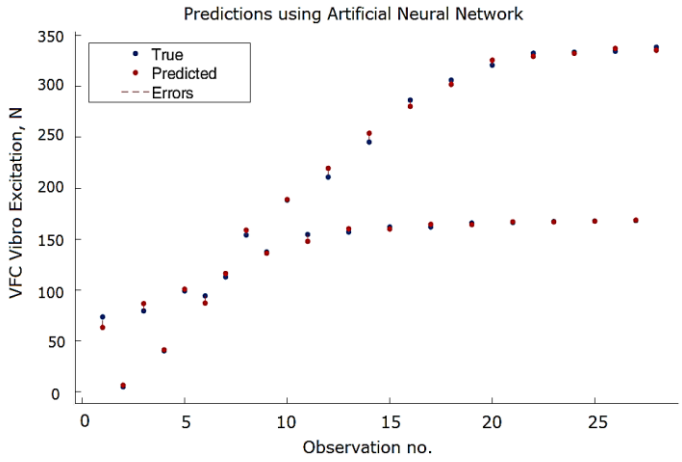

Fig. 3.14 Predicted vs. actual datapoints of the ANN method

During the process of predicting VFC by using the decision tree model, the minimum leaf size was the single hyperparameter that was added in the hyperparameter tuning. It represents the minimum number of training data points that are needed to be used in the leaf node. The size of the training data is the main factor when choosing the leaf size, and, according to our example, the search range for this hyperparameter is between *1* and *15*. The most accurate prediction results received for the DT method are shown in Fig. 3.15; the best outcome was reached when a decision tree having the minimum leaf size with the value of *4* was trained. However, the accuracy of the decision tree was the weakest compared to the ANN, GPR and SVM machine learning methods. As shown in Fig. 3.16, as the accuracy is not as good compared to the previous models (GPR, ANN, SVM) in most of the predictions, the distance between the predicted VFC vibration excitation value and the actual values is significantly higher.

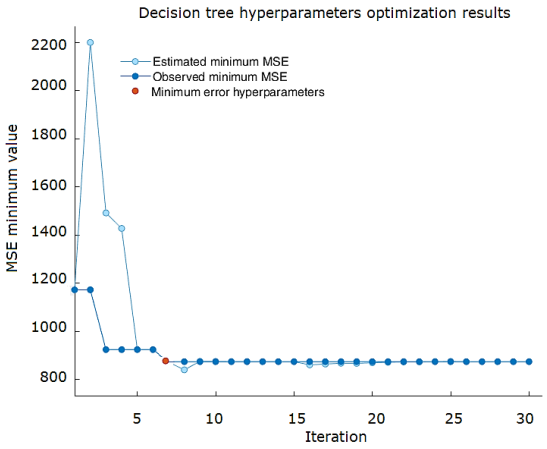

Fig. 3.15 Minimum MSE during the optimization process of DT hyperparameters

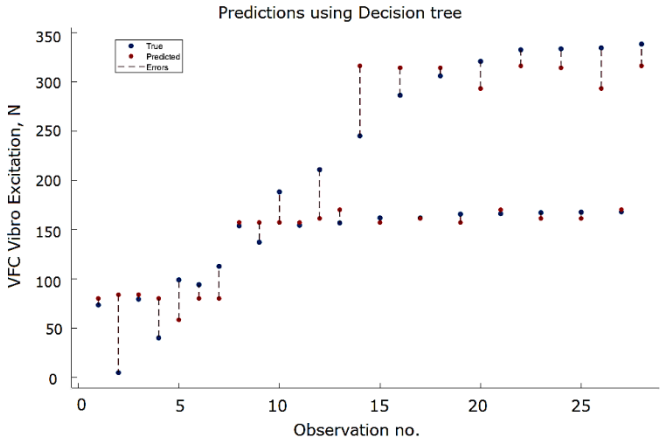

Fig. 3.16 Testing data results of the DT model

During the process of predicting VFC by using the decision tree model KNN method, two hyperparameters were added into the tuning process as presented in Table 3.10. The first hyperparameter is the employed distance function (the most common ones are Manhattan, Euclidean, Minkowski), and the other one is K (the number of neighbors that have to be checked).

Table 3.10 Hyperparameters of the KNN method

	K	**Distance metric**
Value Range	[1; 10]	Manhattan, Euclidean, Minkowski (*p*=1,*p*=1.5,*p*=2,*p*=*Infinity*)

The Euclidean distance, for the *n*-dimensional space, is expressed by applying the below presented Equation (3.9):

$$d_{Eucl}(x,y) = \sqrt{(x_1 - y_1)^2 + (x_2 - y_2)^2 + \ldots + (x_n - y_n)^2} = \sqrt{\sum_{i=1}^{n}(x_i - y_i)^2} \quad (3.9)$$

where $(y_1, y_2, \dots, y_n)$ are the target values of the *y* and $(x_1, x_2, \dots, x_n)$ of the *x* data instances.

The Manhattan distance can also sometimes be called the taxicab geometry, or the city block distance, along with some other names. It is mainly used to calculate the distance between points x and y on a uniform grid, e.g., a city block, where there may be multiple paths between the points x, y that possess the same Manhattan distance. Formula (3.10) should be used when calculating the Manhattan distance between *x* and *y*.

$$d_{Manh}(x, y) = \sum_{i=1}^{n} |x_i - y_i| \quad (3.10)$$

where *n* is the sample size, x_i is the target values of the x data instance, and y_i is the target value of y data instance.

The formula (Equation 3.10) could be altered by replacing 'p' so that to obtain the distance between x and y in an alternative approach. Therefore, the Minkowski distance can also be defined as the *L*p norm distance:

$$d_{Mink}(x, y) = (\sum_{i=1}^{n} |x_i - y_i|^p)^{1/p} \quad (3.11)$$

where p is the Minkowski metric order.

The value of p represents different calculation approaches: when $p = 1$, it can be defined as the Manhattan distance; when $p = 2$, it can be defined as the Euclidean distance, when $p = \infty$, it can be defined as Chebyshev's distance. When $p = 1$, a good balance is provided between the values.

In our study, the best accuracy when predicting VFC with the KNN method was received with *RMSE*=6.0757, *MSE*=36.915 and *MAE*=3.528. The Manhattan distance was chosen for 2 neighbors, *K*=2 (Fig. 3.17).

Determining the correct value of *K* is the most important part when training a prediction model with the KNN method as, when selected optimally, it makes the effect of noise go down. The *elbow method* technique can be used to select the best K value. The unique values of *K* are being passed to the training process with the same data, and the difference in the accuracy of the model with the different *K* is initially observed. When performing hyperparameter optimization for the KNN method, the RMSE results are shown in Fig. 3.18.

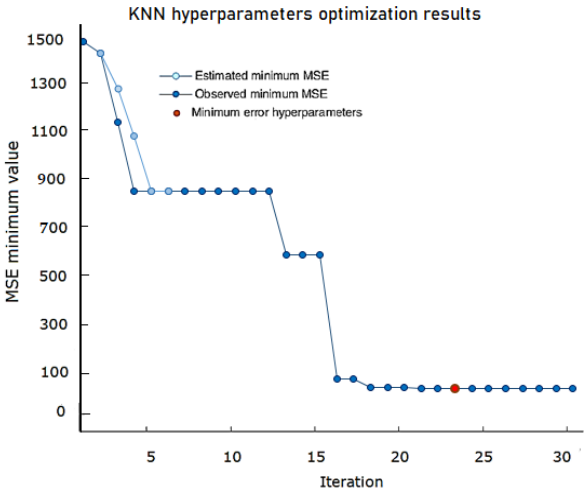

Fig. 3.17 Minimum MSE during the optimization process of KNN hyperparameters

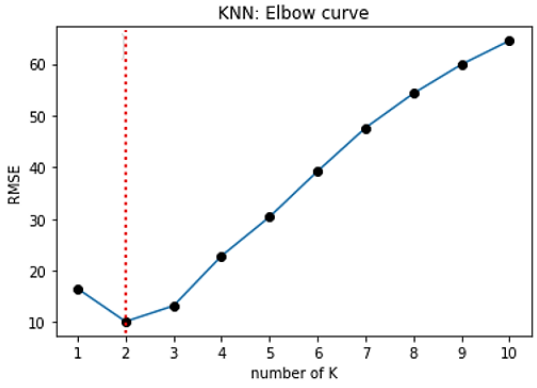

Fig. 3.18 K optimization for KNN method with Elbow curve.

The graph presented in Fig. 3.18 shows that, at first, the RMSE value decreases when K=*2*; however, it starts increasing with the following iterations. This proves that *K* value has to be *2*, i.e., it is the optimal *K* value for the KNN method with the provided data set. The curve depicted in Fig. 3.18 is named the elbow curve as its shape resembles an elbow, which is applied to optimize the *K* value.

Another method to evaluate the fitness of the model is by calculating R^2 (the coefficient of determination) which represents the regression score that indicates the difference of the predicted values to the fitted regression line. The measure shows the quality of regression predictions approximation compared to the real data. When $R^2 = 1$, then we have an indication that the predicted data fits the actual data perfectly.

$$R^2 = \frac{SSR}{SST} = \frac{\sum_{i=1}^{m}(y_i - \hat{y}_i)^2}{\sum_{i=1}^{m}(y_i - \bar{y})^2} \tag{3.12}$$

where *SST* is the total sum of squares, *SSR* is the sum of the squares of residuals, y_i is the actual target value, $\hat{y}_i$ is the predicted target value, and $\bar{y}$ is the average.

The R^2 value ranges from 0 to 100% (or from 0 to 1.0). The R^2 value which is close to 1 represents the good model accuracy. However, maximizing R^2 should not be the goal, as a higher R^2 is linked with a lower model stability and adaptability when new training data is passed through the model. Having adjusted the R^2 value close to R^2 is preferred. The results of the 5 prediction models for the R^2 values are shown in Fig. 3.19. From the presented plots, it has been proven that the DT algorithm yielded the lowest result (R^2=0.878) compared to the other options.

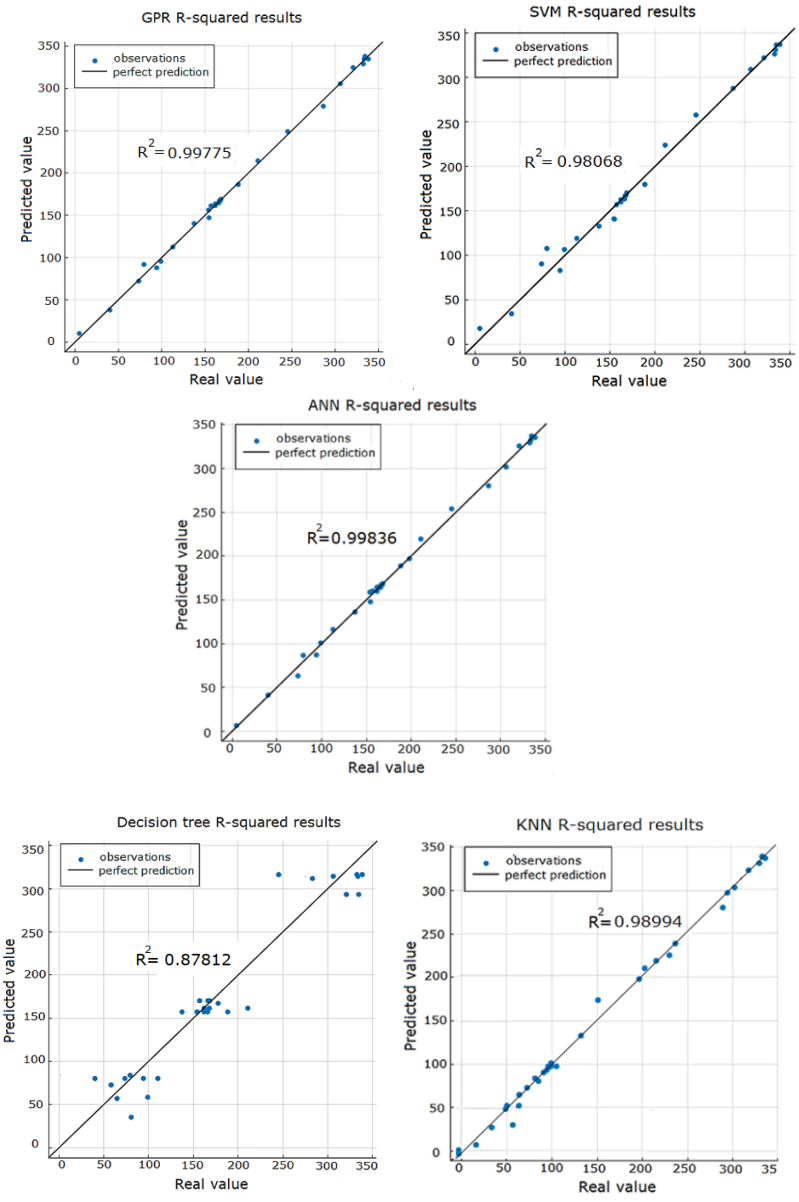

Fig. 3.19 R-squared comparison for each method

To summarize the experimental results of five different prediction methods, ANN and GPR had the highest accuracy for VFC Vibro excitation prediction with the smallest prediction error (RMSE) of 4.5337 and 5.6891, respectively (Fig. 3.20). In addition, it is visible that the DT algorithm is not applicable for the training data set used in the experiments causing highest prediction errors (around 30%) even when the hyperparameter optimization is being used. After comparing the Standard deviation (ST) without the DT model which had the standard deviation value *ST=0* for all 5 iterations, the GDR method had the smallest standard deviation value, i.e., *ST*=0.201. The ANN model scored *ST*=0.616, KNN yielded *ST*=0.78, and SVM offered the largest standard deviation value *ST*=2.531.

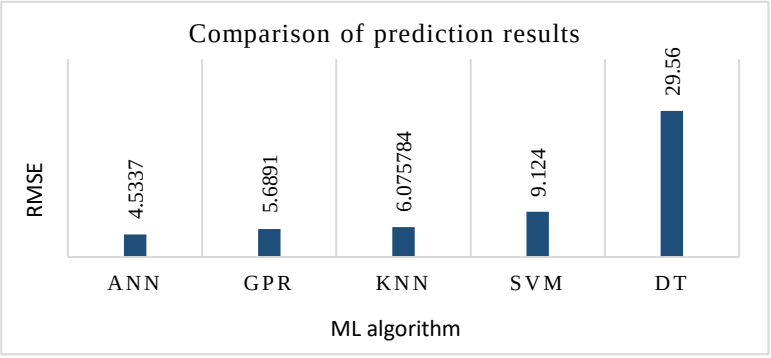

Fig. 3.20 Prediction results comparison of the root mean square error for the methods used in the study

Conclusions of the chapter

1. According to the experimentally predicted values of the vertical forming force component for ultrasonic metal sheet excitation, algorithms of machine training methods for predicting these forces have been formed.

2. It has been demonstrated that the machine learning methods ANN, SVM, GPR, KNN, and DT are suitable to predict the forming force even on a small data set and that they reach good generalization performance on the test data samples.

3. The GPR and ANN models have been found to be the most accurate, although their learning times differ significantly, but this has lower importance than the prediction accuracy results, especially given that the ANN model is 20% more accurate.

IV. RESEARCH OF ROBOTIZED POLYMER SHEET INCREMENTAL SINGLE POINT FORMING

Introduction

This chapter presents an experimental and mathematical model for determining the incremental forming parameters of polymer sheets, while focusing on the heating methods which ensure high-quality finished product results. A new method of heating a sheet by a forming tool is introduced in which a freely rotating sphere at the tip of a tool is heated by a laser and supported in a magnetic ring.

4.1. Thermal modeling of polymer sheet

During the study, the mathematical analysis outputs of the sheet forming process features – the heating temperature relationship with the displacement of the polymer sheet from gravity – were carried out. The *Ansys Transient Thermal* as well as the *Transient Structural analysis* was used to create a mathematical FE model. The materials sheet properties that were used in the model are provided in Table 4.1. Both theoretical analysis and experiments were done by using the same material.

Table 4.1 *PVC Trovidur ESA-D* sheet properties and the geometric parameters [75]

Parameter	Value	Unit
Linear thermal coefficient	70	10^{-6}/K
Compressive strength	65.4	MPa
Density	1.41	g/cm^3
Elongation at break	30.3	%
Sheet width	300x300	mm
Modulus of elasticity in tension	2643	N/mm^2
Notched Impact strength	9.09	mJ/mm^2
Tensile stress at yield	47.75	N/mm^2
Sheet thickness	3	mm
Vicat-softening temperature	75	°C

The mathematical modeling was carried out in two steps: firstly, the temperature dissipation on the sheet was calculated as an output of the transient thermal analysis. Secondly, the dissipation of temperature that was calculated in the first step was reused as an input variable 'the thermal load' in the transient structural analysis. As a result of the analysis, the displacement of the sheet was calculated. In the first step of mathematical analysis, the polymer sheet whose features are listed in Table 4.1 was excited with convection; its surface area features the 25 mm offset from all edges, which represents the area heated by the thermal gun during the SPIF process. The surrounding temperature and the other primary conditions were used by adding a second convection with different values on the surface of the sheet. The scheme of the mathematical model is shown in Fig. 4.1, a, with the boundary conditions defined in Fig. 4.1, b.

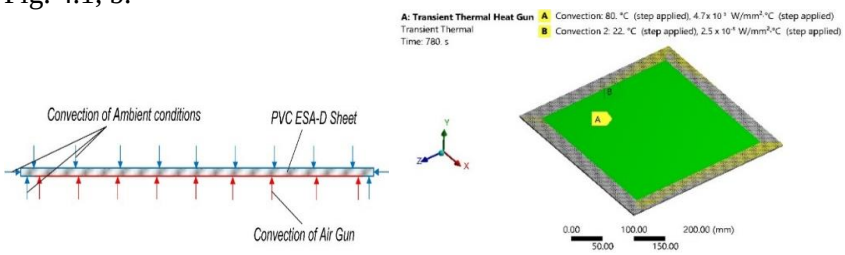

a) b)

Fig. 4.1 Transient thermal computational research: scheme (a); numerical model with boundary conditions (b)

The finite element method mathematical simulation data is outlined in Table 4.2. The total duration to get the results from the first and second steps was 780 s. The first step was divided into 50 sub-steps and took 5 seconds to run. Meanwhile, the second step was divided into 100 sub-steps, and it took 776 s to calculate the results.

Table 4.2 FE mathematical analysis data at the first stage

Parameter	Value	Unit
Coefficient of convection of the surface area of a heat gun	47	W/m2
Coefficient of convection of the remaining surface area	25	W/m2
Temperature of convection of the heat gun surface area	80	°C
Temperature of convection of the remaining surface area	22	°C
Mesh elements method	Hex Dominant	-
Finite elements	3600	-
Nodal points	25803	-
Calculation time	780	s

The results of the simulation analysis provide the temperature distribution of the upper surface of the sheet, where the ambient convection was added, and therefore this surface is opposite to the heating surface after 2 s of the start of heating, as presented in Fig. 4.2, a. After 780 s from the start of the heating process, the surface temperature distribution is shown in Fig. 4.2, b.

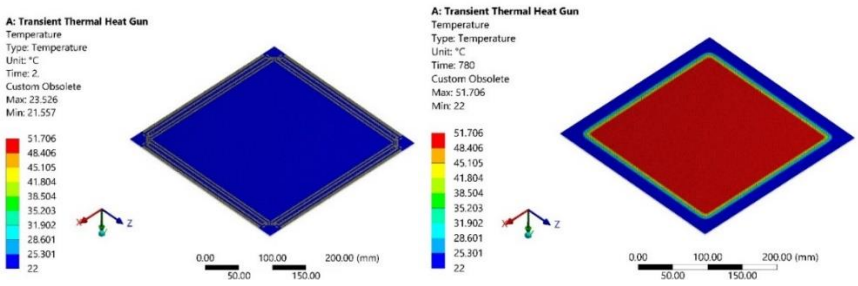

a) b)

Fig. 4.2 Temperature distribution at the opposite side to the heating surface: (a) heating duration 2 s; (b) heating duration 780 s

The simulation results by heating the polymer sheet from the upper side are presented in Fig. 4.3.

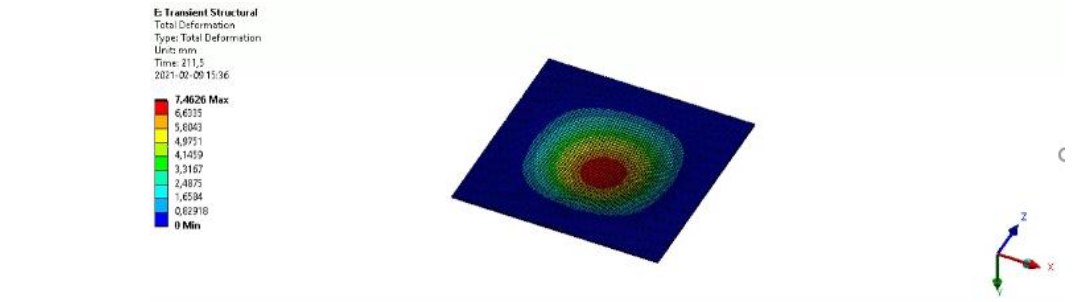

Fig. 4.3 Temperature dissipation from the upper side to the heating surface when the heating duration is 211 s

The maximum and the average temperatures during the period of time are shown as a result of a numerical simulation on the opposite surface to the heating of the sheet and are shown in Fig. 4.4. It is visible that the speed of the change in the temperate is high at the beginning of the heating process, but it stops changing afterwards.

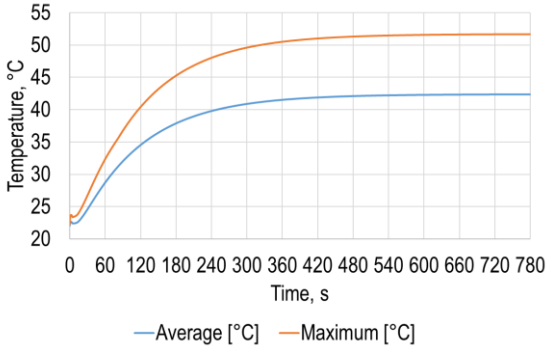

Fig. 4.4 Maximum and average temperatures of the opposite to the heating surface vs. heating duration

The outcome of the analysis has proven that the temperature dissipation on the opposite side of the heating surface is close to the heating area surface. Therefore, selecting the correct heating flow surface and the geometry has a significant importance in the SPIF process. As shown in Fig. 4.3, when the heating duration reaches 780 s, the maximum temperature of the surface at the opposite side is 51.7 °C, while the average temperature is at 42.4 °C. The results of the temperate change analysis during the period of time could be used to define the heating moment when the forming process should be started as well as the temperature required for the SPIF process.

The results of the previous analysis were used as the input parameters for the transient structural analysis simulation. The next stage of simulation was carried out by using these results as the input loads for the transient structural analysis. During this stage, the polymer sheet was fixed by using the same heating gun side on the 25 mm offset from the sheet edge on the same side as the heating gun. The earth gravity vector was perpendicular to the surface.

The structural analysis simulation scheme is shown in Fig. 4.5, a, and the numerical model with the applied boundary conditions is presented in Fig. 4.5, b.

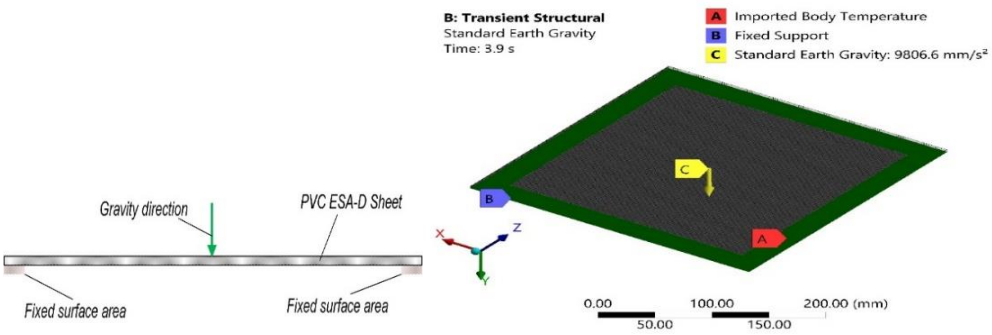

a) b)

Fig. 4.5 Transient structural simulation: scheme (a); numerical model with boundary conditions (b)

The finite element method simulation data from the transient structural analysis step is given in Table 4.3.

Table 4.3 FE numerical analysis parameters

Parameter	Value	Unit
Gravity acceleration	9806.6	mm/s^2
Input load	Temperature	°C
Mesh elements method	Hex Dominant	-
Finite elements	3600	-
Nodal points	25803	-
Calculation time	780	s

The total deformation results after the PVC sheet was heated for 780 s are shared in Fig. 4.6, a. For comparison, the same instance of Von Mises stress is depicted in Fig. 4.6, b.

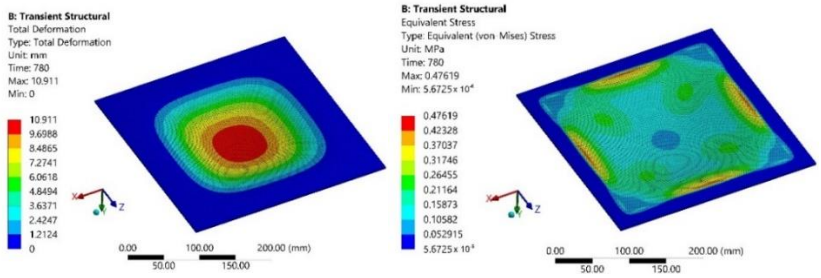

a) b)

Fig. 4.6 Results of a model where the heating duration is 780 s: strain (a); stress (b)

The maximum and the average deformation of the sheet during the period of time are shown as the results of the simulation in Fig. 4.7.

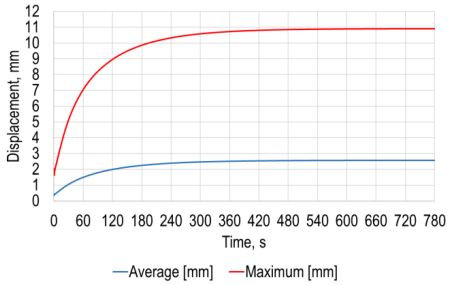

Fig. 4.7 Maximum and average deformation vs. heating duration

As it is shown in the plot above, the average deformation of the PVC sheet is 2.6 mm, while the maximum is more than 10.9 mm. As a result, the correct forming forces as well as the initial forming depth need to be selected when performing the SPIF process.

4.2. Validation of numerical simulation results

In order to validate the mathematical modeling outcomes, the experiments using the input parameters and the same setup should be executed. The scheme of the experimental setup is presented in Fig. 4.8, a, and the actual experimental setup is presented in Fig. 4.8, b. *PVC ESA-D* polymer sheet *1* was used in the experiments and it was clamped to frame *2* with the 25 mm offset area from its edge in the same way as in the numerical analysis. The hot air blowing system *CT-850D* (*Acifica, Inc.*, San Jose, USA) *6* was used to generate heat by blowing hot air to the bottom of the surface. The laser displacement meter *Kyence LK-G82/3001* (*Keyence Corporation*, Neu-Isenburg, Germany) *3* was used to determine the surface displacements. The signal from the displacement meter would be passed to the digital oscilloscope *PicoScope-6403* (*Pico Technology Ltd.*, Cambridgeshire, UK) *5*. During the heating process, the polymer sheet surface temperature was being measured by using the thermal imaging camera *FLIR T450sc* (*FLIR Systems Inc.*, Wilsonville, USA) *7*.

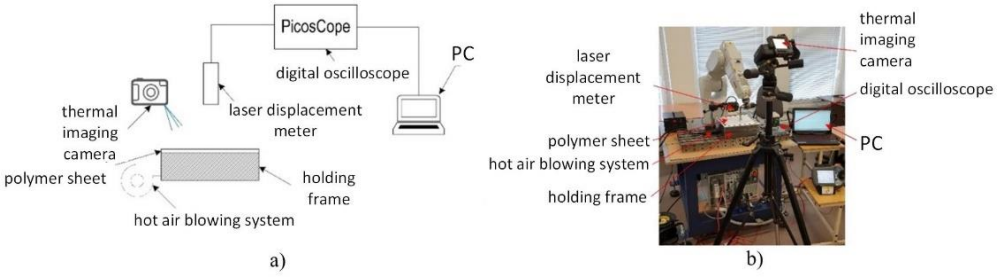

Fig. 4.8 Polymer heating experimental setup (a) scheme; (b) setup

The heating device on the opposite side to the sheet surface is shown in Fig. 4.9.

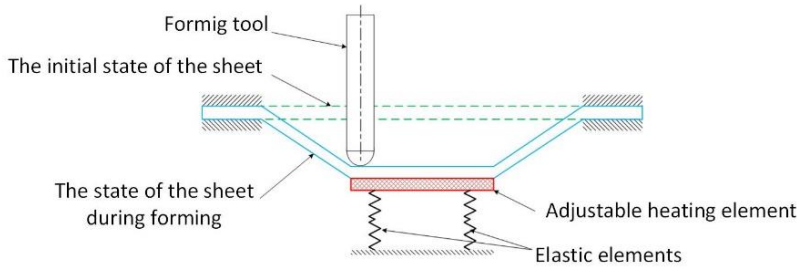

Fig. 4.9 Polymer sheet heating equipment experimental setup

The PVC sheet displacement and PVC sheet surface temperature experimental results were compared with the theoretical model results in Fig. 4.10. It is visible that the polymer sheet's maximum temperature is 25.8 °C when the heating duration is 2 s; meanwhile, when the heating duration is 780 s, the maximum temperature is reached at 45.5 °C. What is more, it is visible from the figure below that the surface displacement value starts increasing when the temperature reaches 31 °C.

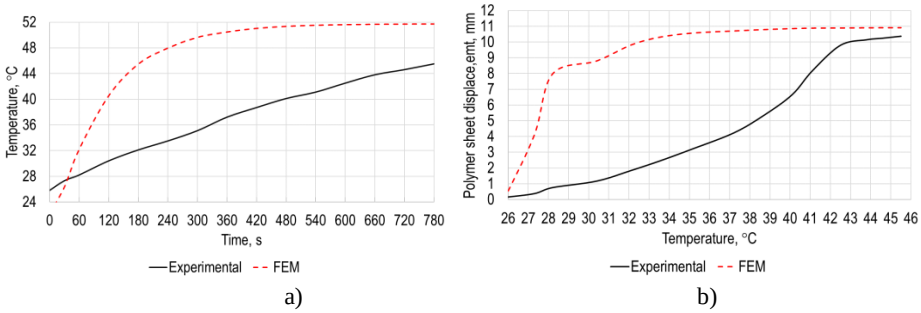

Fig. 4.10 Comparison of theoretical and experimental validation results: (a) temperature vs. time; (b) displacement vs. temperature

As we can see from the results, the experimental output values are close to the theoretical model output values as shown in Fig. 4.4 and Fig. 4.7. During the start of the heating process, the temperature is lower because the heating area where the blowing hot air is being applied is smaller compared to the heating used in the numerical model. This confirms that there is no need for multiple experiments in the manufacturing process as mathematical models can be used to define the input parameters for the SPIF process in the early stage.

The temperature distribution outputs of the experiments are shown in Fig. 4.11.

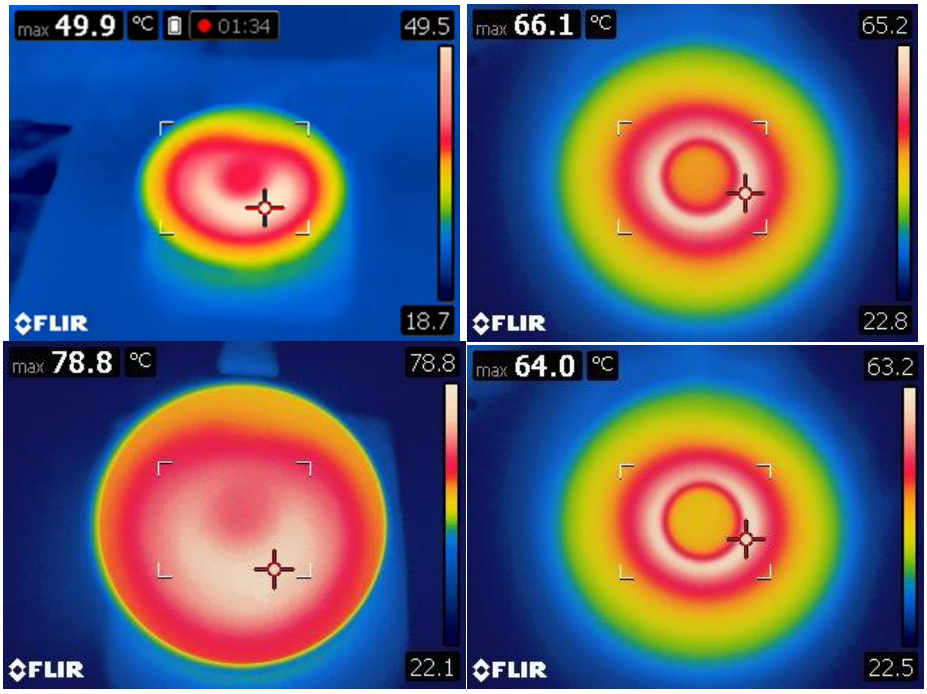

Fig. 4.11 Temperature distribution during the polymer SPIF process

4.3. Development of a polymer point deformation device

In order to eliminate self-deformations that happen as a result of earth gravity which were obtained both experimentally and theoretically, as shown in Fig. 4.7 and Fig. 4.10, b, the usage of backing plates is typical. However, the usage of backing plates is associated with such negative effects as the price to produce the formed material increases, and the forming process duration is reduced because the backing plate has to be created for each new form that needs to be shaped. These downsides could be eliminated if, instead of deformation plates, a forming tool itself could be heated. Additionally, this would make the heating of the material process much faster. To prove the efficiency of the tool, a numerical simulation, such as the one demonstrated in previous example, has been created.

In order to define the numerical model with the newly developed tool, the heating temperature relationship with time and the displacement relationship with temperature need to be analyzed. In this simulation, heating at a specific point is modeled, while, in the second step, the heating was modeled as the air flow from a heat blowing system. The Ansys Transient Thermal and the Transient Structural analysis was used for the computational FE model for the same material with the same features as in the previous example. Same as previously, the mathematical simulation was implemented in 2 steps. The polymer sheet was excited by using a blowing heat flow derived as the heat power changing in time, which relates to the point heating source. The features that are used for the heat flow are described in Table 4.4, and the heat flow power dependency from the time plot is presented in Fig. 4.13.

Table 4.4 Excitation heat flow parameters

Time, s	Heat flow power, W
0	0
0.18	4.5
3	2.2
50	0.05
120	0

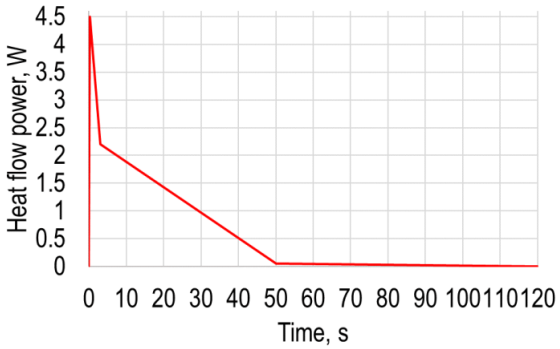

Fig. 4.13 Excitation heat flow plot

The surrounding temperature and convection have been reused from the previous example. The transient thermal analysis scheme is presented in Fig. 4.14, a, and the numerical model with the applied boundary conditions is presented in Fig. 4.14, b. The results of the FE numerical simulation were presented in Table 4.5.

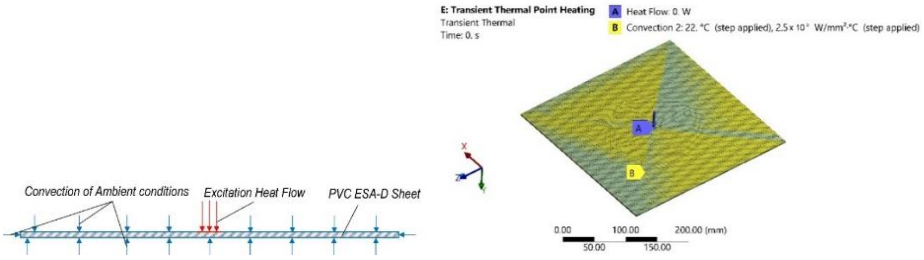

a) b)

Fig. 4.14 Transient thermal numerical simulation: (a) scheme; (b) numerical model with boundary conditions

The total duration to get the results from the first and the second stage was 120 s. The first stage was divided into 50 sub-stages and took 3 seconds to run. Meanwhile, the second stage was divided into 100 sub-stages, and it took 120 s to calculate the results.

Table 4.5 Numerical analysis data of the first stage

Parameter	Value	Unit
Coefficient of convection of the remaining surface area	25	W/m2
Coefficient of convection of the remaining surface area	22	°C
Geometry of heat flow	Ø10 mm circle	-
Magnitude of heat flow	Tabular	W
Mesh elements method	Hex Dominant	-
Finite elements	15.124	-
Nodal points	103.231	-
Calculation total time	120	s

The temperature distribution of the bottom surface of the sheet is the final output to the simulation results. The temperature distribution when the heating duration is equal to 3 s is shown in Fig. 4.15, a. The temperature distribution of the same surface when the heating duration is 120 s is shown in Fig. 4.15, b.

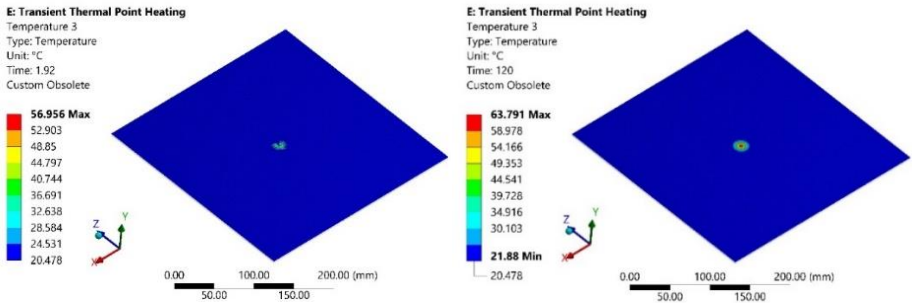

a) b)

Fig. 4.15 Temperature distribution on the opposite side to the heating surface of the sheet: (a) heating duration 3 s; after the start of heating (ba); after the heating duration 120 s from the start of heating (b)

As it is visible from the results of the simulation (Fig. 4.16), the relationship between the temperature and the heating time as well as the relationship between the displacement and the heating time has been generated. The change in temperature is nonlinear, and it becomes constant with time.

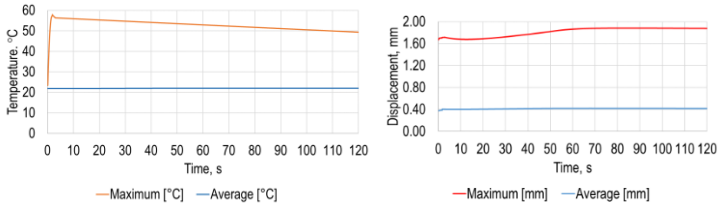

a) b)

Fig. 4.16 Simulation results: (a) maximum temperatures vs. heating time; (b) maximum strain vs. heating time

As it is shown in the results (Fig. 4.16), the average and maximum temperature of the polymer sheet has a significantly higher value compared to the previous modeling case shown in Fig. 4.4. This suggests that only a small part of the sheet is being heated. From the temperature dependency on the time plot, it is visible that the average temperature when the heating duration is 120 s is 22.1 °C, and the maximum values is 49.3 °C at the same point in time. Meanwhile, the maximum temperature at the same 120 s point in time is 57.9 °. The smaller heating zone and the shorter duration prove to have a higher effectivity as a result, and the process with the developed tool is respectively more effective compared to the heating with a hot air blowing system. The results of this analysis can be used when deriving the input parameters for the heat flow power for the forming process.

The following step of the numerical model was carried out identically to the process defined in Section 4.1, and the scheme of the same process as in Fig. 4.4 can be reused, whereas the only parameter that differs is the heating time of 120 s. The total deformation results after the PVC sheet was heated for 120s are represented in Fig. 4.17, a. For comparison, the same instance of Von Mises stress was depicted in Fig. 4.17, b.

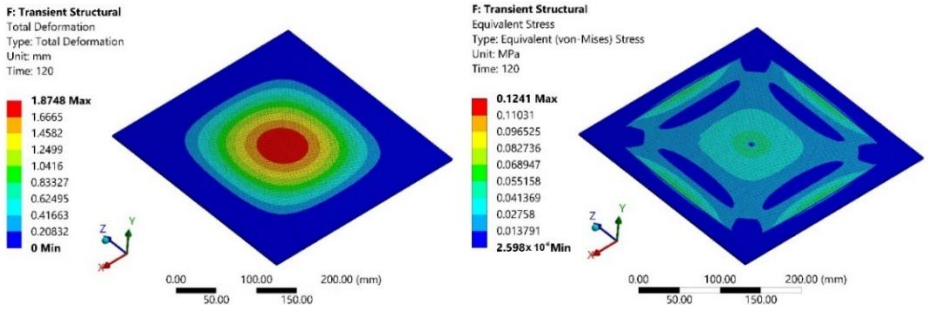

a) b)

Fig. 4.17 Modeling results of the second stage model after 780 s from the start of heating: total strain (a); equivalent stress (b)

The results of the maximum deformation with the impact of the earth gravity vs. time are depicted in Fig. 4.16, b. It is visible that the maximum deformation of the PVC sheet is higher than 1.9 mm, while the average deformation of the pvc sheet is higher than 0.42 mm. The average and maximum deformation is lower when compared to the ones that were listed in Section 2. This proves that the forming process can be improved by using the innovative forming tool where point-heating is implemented.

The tool for which the point heating is available has been created, and an application for the patent has been submitted (Fig. 4.18).

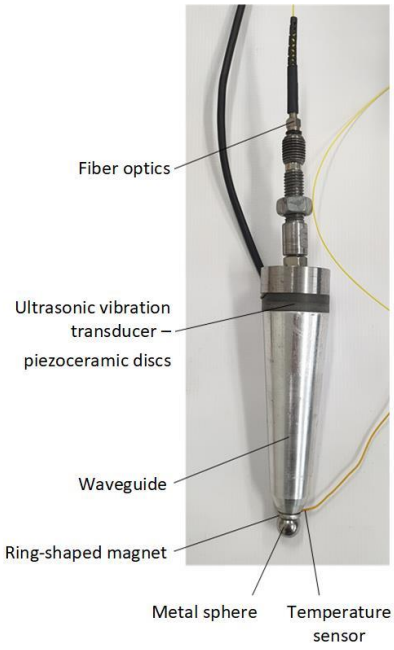

Fig. 4.18 Forming tool for polymer sheet

The polymer sheet material is being formed by using the 3D free-rotating metal sphere *1* which is attached to the ring-shaped magnet *2*. The waveguide *3* is added inside the tool and is excited by using the ultrasonic vibration transducer *4* which reduces the friction of the metal ball against the ring-shape magnet and creates its free rotation. The laser beam which is created by fiber optics is heating the metal sphere, and, in order to control the temperature feedback mechanism, the temperature sensor 6 is used.

The impact of ultrasonic vibrations is covered in the paper [76] where piezoelectric actuators are used to excite the material. It is explained that vibrations reduce the friction force in the area where the tool is contacting the surface of the material. Coulomb's friction law modification may be used to define the vibration friction contact. The local point heating device usage in the forming process is depicted in Fig. 4.19.

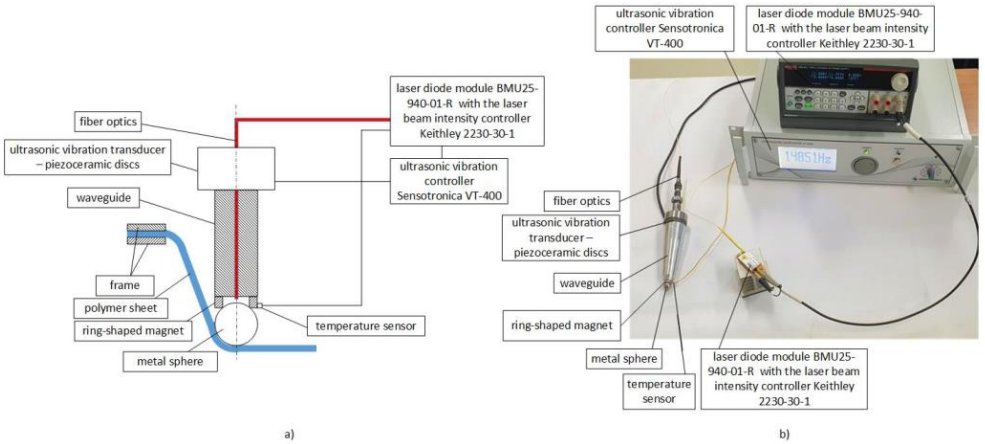

a) b)

Fig. 4.19 SPIF process where laser heating is used: (a) scheme; (b) device

When the tool with the laser point heating is used, significant improvement of plasticity and reduction in the deformation force is noticed. This process completely substitutes the usage of a backing plate, thereby assuring that the forming process has improved. No additional supporting structure is needed when the material that needs to be formed is unique or features a complicated shape. In addition to heating, the ultrasonically excited tool reduces the friction between the forming tool and the polymer sheet.

4.4. Investigation of thermal effects on polymer deformation

The mathematical simulation outcomes need the experimental validation when using the input parameters and the same setup. The scheme and the experimental setup for the forming process using point heating can be found in Fig. 4.20.

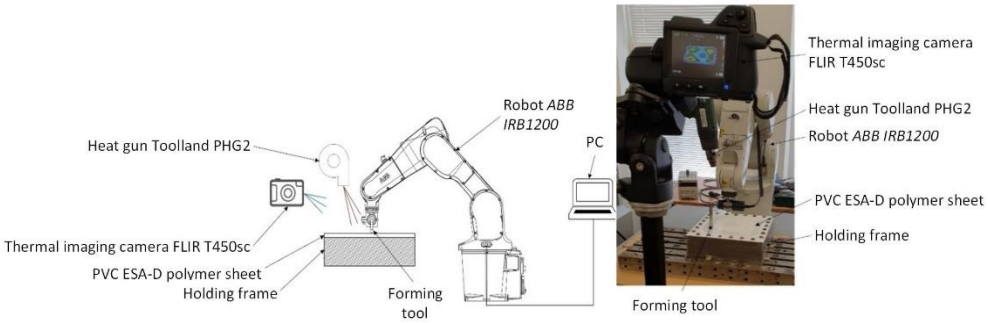

a) b)

Fig. 4.20 Experimental setup of robotized polymer sheet SPIF: (a) scheme; (b) setup photo

In the experimental setup diagram, the *PVC ESA-D* polymer sheet is attached to the holding frame. A robot *ABB IRB1200* (*ABB Robotics & Discrete Automation*, Västerås, Sweden) with its hand movements is moving a tool which is in contact with

the material surface and which creates formations on the sheet. A hot air gun *Toolland PHG2* (*Tooland Inc.*, San Carlos, USA) is used to heat the surface of the polymer sheet. In order to control the heat during the SPIF process, a thermal imaging camera *FLIR T450sc* (*FLIR Systems Inc.*, Wilsonville, USA) is used.

Table 4.6 Forming process parameters

Parameter	Value	Unit
Feed rate	100	mm/s
Major diameter of the geometric figure	150	mm
Maximum surface temperature	60	°C
Minimum surface temperature	40	°C
Minor diameter of the geometric figure	90	mm
Radial step	0.5	mm
Radius of the forming tool sphere	8.5	mm
Step down	0.5	mm
Total forming depth	30	mm

Fig. 4.21 presents the temperature distribution of the polymer sheet surface when using (a) a process where a hot air gun is used for heating and (b) a process where the innovative tool with laser point heating is used. The minimum values of the temperature that were measured near the contact of the tool with the polymer sheet are in range from 40 °C to 60 °C). While forming the polymer sheet, one should never exceed the temperature of 75 °C in order not to puncture the material.

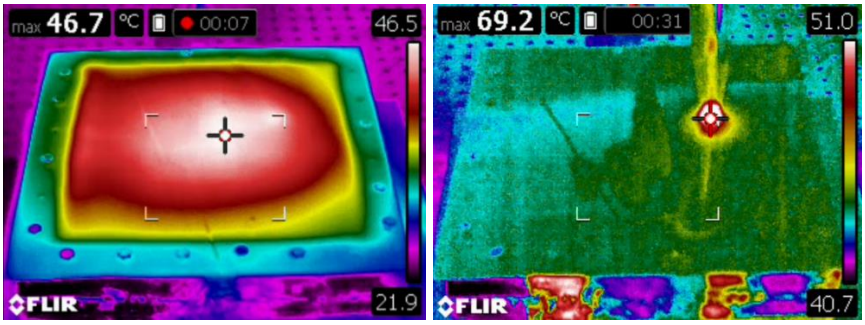

a) b)

Fig. 4.21 Thermal images of polymer sheet: a) heated with air gun; b) heated with advanced heating device

Fig. 4.22 represents 4 different shapes that were formed by using the polymer sheet SPIF process. The parameters that were used for the processing are listed in Table 4.6.

a) b) c) d)

Fig. 4.22 The output of PVC ESA-D polymer sheet SPIF process (a) spatial circular shape; (b) spatial square shape; (c) spatial flower shape; (d) spatial star shape

4.5. Comparison of polymer forming tools

The robot *IRB1200 M2004* was controlled by using the standard version of the *ABB* controller *IRC5 M2004*. However, its analog inputs are not present in the controller. In order to to be able to use the controller *IRCS M2001*, a *DeviceNet* network adapter *CREVIS NA-9111* with the analog input channels extension *PicoScope-3424* (*Pico Technology Ltd*., Cambridgeshire, UK) was used. A Torque sensor *Mark-10 STJ100* which was also used elsewhere in the experiment can provide the analog output of ±1 V at the full scale, and the extended analog input offers a dynamic range of 0–10 V (*PicoScope-3424*). Thus, in order to be able to take full advantage of the dynamic range of the 12 bits analog input, the signal was amplified five times, while at the same time providing the positive offset voltage. The scheme of a robotized feedback system is shown in Fig. 4.23.

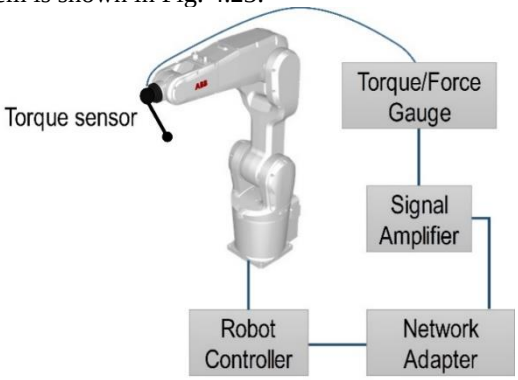

Fig. 4.23 Feedback system for robotized polymer sheet forming process

Forming experiments using a 2 mm thick *PVC Trovidur ESA-D* polymer sheet were conducted. The formed workpiece had a cone shape with a major diameter of 140 mm and a minor diameter of 80 mm, and the depth of 30 mm. The experiments were carried out with three different forming tools at 0.5 mm vertical and horizontal steps with the Ø17 mm and Ø10 mm diameter free-rotating tools and a Ø10 mm rotating laser heated to 46 °C sphere in a magnetic ring.

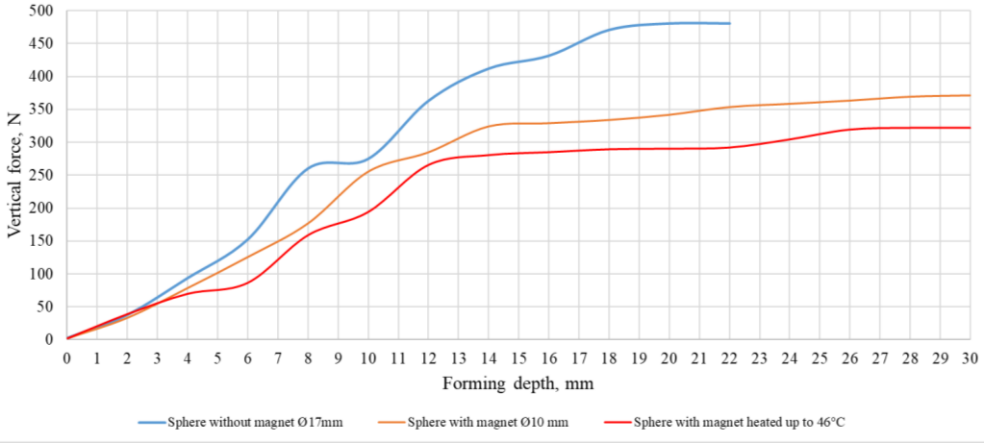

Fig. 4.24 Forming force vs. Forming depth, using three different forming methods

From the forming results where different forming tools were being used (Fig. 4.24), it is visible that the lowest vertical force to form the material is needed when the forming is done with a tool specified in the third option (i.e., both migration and heating is present). Meanwhile the largest vertical force to form the material is needed for the first case, where the tool is not excited with vibrations and is not heated additionally.

The most important thing during the polymer sheet SPIF process is to make sure that the quality of the material and the sample surface is not reduced while the temperature is being raised. Polymer materials usually have the thermal transitions while being heated, which provides insights into their morphology. When heating is applied to a material, it becomes softer, and the strength of the sheet is getting lower. In order to form the material in the desired shape, the material has to be heated first. Once the material has been heated, the forming tool movement creates surface deformations. As the path can be easily defined in the 3 D space, the process can be applied for various shapes. The main goal was to understand the mechanical behavior of the polymer sheet while forming friction when the heating is involved and at the same time making sure that the quality of the material does not suffer. Heating the tool during the forming process provides increased plasticity of the sheet at the contact zone with the less detrimental deformation force that keeps the stiffness at the same value; hence, the backing plate can be eliminated from the process.

Conclusions of the chapter

1. A numerical model of the tool-workpiece interaction process has been developed as a non-linear model due to the large plastic deformations of the sheet, while estimating the boundary conditions occurring between the tool and the sheet at the point of contact. The possibilities of the metal sheet formability have been investigated, and the criteria for its piercing have been determined. The obtained results show that the effective strains achieved during the incremental forming are much higher than those indicated in the material data sheet as the tensile deformation

values are 3–8%, and the values of the failure strain calibrated by the cupping test constitute 38%.

2. The results obtained with the help of the developed numerical metal sheet forming model are close to those obtained experimentally with a deviation of up to 5%. The developed and patented robotized metal sheet SPIF equipment allows reducing the friction force on the sheet surface by replacing the environmentally unfriendly lubrication with ultrasonic sheet excitation in two orthogonal directions on its plane. The coefficient of friction of the metal sheet surface under the ultrasonic excitation is close to that of the lubricated surface: 0.12 and 0.10, respectively.

3. A prediction of the vertical forming force component for ultrasonic metal sheet excitation while using such machine learning algorithms as ANN, SVM, GPR, KNN, and DT has been performed while optimizing the Bayesian hyperparameters and obtaining the architecture, and ultimately achieving the best possible result by combining four hyperparameters of the technological input network. When summarizing the results of the modeling accuracy, the ANN and GPR models were found to be the most efficient, although their learning times differed significantly, but this factor is less important than the prediction accuracy results given the aspect that the ANN model is 20% more accurate.

4. The results of the numerical simulation of various heating methods of polymer sheets have been confirmed by using the developed and patented robotized polymer sheet incremental forming stand. The results show that the proposed and patented solution for heating the polymer sheet at the point of the contact with the forming tool while using laser beam energy shortens the heating time and reduces the deformation of the sheet by more than 6 times from 780 s to 120 s, and from 2.6 mm to 0.42 mm, respectively. The experimental studies of the robotized polymer sheet SPIF have confirmed that the proposed local heating method reduces the forming forces and the heating time of the sheet, and the forming process can be performed without the support of the polymer sheet with a backing plate.

SANTRAUKA:

Temos aktualumas

„Pramonė 4.0“ yra nauja pramonės revoliucija, o šios naujos koncepcijos priėmimas suteikia didžiules galimybes įgyvendinti Žiedinės ekonomikos veiksmų plano iniciatyvas švaresnei ir konkurencingesnei Europai, kartu žadant pagerinti bet kurio gamybos proceso kokybę, lankstumą ir efektyvumą. Remiantis naujausia Pramonės savaitės ataskaita „Gamybos ateitis: 2020 ir vėliau“, gamintojai pradeda tolti nuo masinės gamybos. Dabar jie gamina labiau pritaikytus ir pagal užsakymą pagamintus produktus. Dėl šio pokyčio tradiciniai lakštų formavimo procesai ima atrodyti vis mažiau perspektyvūs. Tradiciniai metodai yra ekonomiški tik tada, kai gamintojai gamina dideles identiškų dalių partijas. Laipsniškas lakštų formavimas yra šios problemos sprendimas. Tai leidžia pasiekti kokybišką lakštų formavimą be papildomų išlaidų, susijusių su įprastiniais lakštų formavimo procesais. Medžiagų lakštų, kaip vieno taško laipsniško formavimo (angl. *single point incremental forming* (SPIF)), naudojimas užsienyje vis dar nėra plačiai paplitęs. Tokia technologija Lietuvoje dar nesukurta, todėl nenaudojama. SPIF mechanikos sudėtingumas ir ypatingos sąlygos, tokios kaip lenkimas veikiant įtempiams, ciklinis lenkimas ir išlenkimas, taip pat šlyties deformacijos, kurios prisideda prie bendro formuojamumo gerinimo, reikalauja naujų mokslinių tyrimų ir metodų kūrimo. Be matematinių modelių, disertacijoje kuriama robotizuota lakšto SPIF įranga, siūlomi du inovatyvūs metodai, dėl ultragarso sumažinant įrankio trintį ant lakšto paviršiaus, tuo eliminuojant aplinkai kenksmingą tepimą, bei lokalų lazerinį kaitinimą, leidžiantį atsisakyti lakšto parėmimo. Kadangi tradiciškai SPIF proceso metu formavimo įrankio trintis su ruošiniu sumažinama sutepus kontaktinius paviršius, šiame moksliniame darbas siūlomas novatoriškas trinties mažinimo sprendimas vibruojant ruošinį, kuris ne tik leidžia išvengti aplinkai kenksmingų tepimo skysčių naudojimo, bet ir sutrumpina gaminio pagaminimo laiką bei pagreitina jo patekimą į rinką. Siūlomas naujoviškas PVC polimero lakšto SPIF šildymo būdas, siekiant išlaikyti polimerinės plokštės standumą aplink šildomą įrankio sritį ir pašalinti atraminės plokštės poreikį. Tokiu būdu galima sutrumpinti gamybos laiką ir pagreitinti gaminio patekimą į rinką. Šio tyrimo motyvas yra susijęs su naujos, nebrangios ir iki šiol retai naudotos technologijos kūrimu dėl nenuspėjamų polimerinių lakštų šiluminių deformacijų. Būtent šios deformacijos iš dalies nulemia kuriamo gaminio kokybę, o galimybė jas kontroliuoti sukeltų jų plitimą pramonėje, pakeičiant kur kas brangesnį 3D spausdinimą. Gamybos kaštai taip pat sumažinami naudojant darbe siūlomus robotus, o ne brangias CNC stakles SPIF procesui. Šis mokslinis darbas skirtas MTEP – vienam iš svarbiausių „Pramonės 4.0“ etapų, kai pirmą kartą Lietuvoje kuriami ir išbandomi skaitmeniniai ir fiziniai metalų ir polimerų SPIF procesai. SPIF yra nesuvaržyto lakšto deformavimo procesas, kurio metu lakštinė medžiaga palaipsniui deformuojama. Jėga veikia lakštinę medžiagą naudojant įrankį sferiniu antgaliu. SPIF yra giluminio ištempimo proceso alternatyva. Didelis SPIF pranašumas yra tas, kad šis procesas gali būti ekonomiškas net ir mažos apimties gamybos metu. Gaminio dizainą galima pakeisti labai greitai ir paprastai, su minimaliomis išlaidomis. Tai neįmanoma naudojant giluminį ištempimą, kai keičiant dizainą reikia pagaminti

brangų naują štampą. Europos „žaliasis susitarimas“ turės tapti augimo strategija, kartu siekiant klimato pokyčių stabilizavimo tikslų. Todėl pramonės politika privalės sudaryti sąlygas patekti į greitai augančias rinkas, pasitelkus inovacijas ir naujas technologijas išsaugant darbo vietas. Tai leistų ne tik pasiekti žaliojo kurso tikslus, bet ir sumažinti Europos Sąjungos priklausomybę nuo importo bei sustiprinti jos strateginę autonomiją.

Apibendrinti metalų ir polimerų SPIF procesų tyrimo rezultatai šiame darbe leido išryškinti kiekvieno proceso privalumus ir pateikti sprendimus šios technologijos tobulinimui. Tirtiems formavimo procesams pateikiama holistinė SPIF koncepcija iš skaitmeninio komponento modelio, taikant dirbtinio neuroninio tinklo architektūrą. Sukurta tinkama tinklo įvesties ir išvesties struktūra. Tinkamam mokymui sukurti subalansuoti duomenų rinkiniai. Susijusi tinklo topologija buvo identifikuojama, apmokoma ir išbandoma. Ištirta skirtingų mokymo algoritmų, tinklo konfigūracijų ir mokymo rinkinių įtaka. Mašininio mokymosi algoritmų lyginamoji analizė, skirta numatyti jėgos poveikį robotizuotam formavimui, leido identifikuoti efektyviausius algoritmus.

Šiame tyrime pristatomi MTEP rezultatai bus prieinami *Future Smart Factories* kūrėjams; be to, tai palengvins reikalingų produktų tiekimą kritinėmis sąlygomis, kurias lemia globalizacijos procesai.

Tyrimo tikslas ir uždaviniai

Šio tyrimo tikslas – ištirti ir sukurti robotizuotą metalo ir polimero lakštų vienataškio prieauginio formavimo technologiją bei prognuozuoti formavimo jėgas mašininio mokymosi algoritmais.

Norint pasiekti užsibrėžtą tyrimo tikslą, keliami šie uždaviniai:

1. Teoriškai ištirti metalo lakšto taškinio laipsniško formavimo proceso stiprumines ir dinamines charakteristikas bei sukurti aplinkai nekenksmingą technologiją.
2. Eksperimentiškai validuoti ir pritaikyti sukurtą ir patentuotą aplinkai draugišką robotizuotą metalo lakšto laipsniško formavimo technologiją.
3. Atlikti lyginamąją mašininio mokymosi algoritmų analizę, skirtą prognozuoti jėgos poveikį robotizuotam formavimui.
4. Teoriškai ir eksperimentiškai ištirti robotizuotą polimero lakšto taškinio laipsniško formavimo technologiją ir sukurti efektyvų polimero kaitinimo būdą.

Tyrimo metodai

Atliekant tiriamąjį darbą, kuris pristatomas šioje disertacijoje, buvo vykdomi tiek teoriniai, tiek eksperimentiniai tyrimai. Virpesių teorija buvo pritaikyta skaitmeniniam modeliavimui, kuris atliktas baigtinių elementų metodu su komerciniais „Ansys“, „Comsol Multiphysics 5.1.“ ir „Ls-Dyna“ programiniais paketais, panaudojant robotą, pjezoelektrinius keitiklius, 3D skenuojantį lazerinį Doplerio vibrometrą (Polytec Inc.) bei „PicoScope“ techninę ir programinę įrangą tyrimo metu gautiems signalams apdoroti. Teorinės išvados buvo patvirtintos

eksperimentiniais tyrimais, atliktais Kauno technologijos universiteto Mechatronikos institute.

Ginamieji teiginiai

1. Trinties koeficientas tarp dviem kryptimis vibruojamo lakštinio metalo paviršiaus ir formavimo įrankio yra identiškas tepamų paviršių trinties koeficientui.
2. Taškinis kaitinimas leidžia išlaikyti polimerinio lakšto standumą aplink šildomą įrankio sritį ir nereikalauja atraminės plokštės.
3. Dirbtinio intelekto metodų panaudojimas formuojančių jėgų prognozavimui leidžia paspartinti produkto kūrimą.

Mokslinis naujumas

1. Sukurtas skaitinis metalo lakšto vienataškio laipsniško formavimo (angliškai SPIF) modelis leido įvertinti kontaktinę formavimo įrankio ir lakšto sąveiką, nustatyti lakšto pradūrimo jėgas bei įvertinti sienelės plonėjimo procesą formuojant.
2. Pasiūlytas ir sukurtas polimero lakšto kaitinimo ir formavimo metodas leido suformuluoti sąlygas tinkamiausiam gaminio formų išgavimui.
3. Nustatyta, kad ANN ir GPR modeliai yra veiksmingiausi prognozuojant formavimo jėgą santykinai mažame duomenų rinkinyje ir užtikrina gerą apibendrinimo našumą bandomiesiems pavyzdžiams.

Praktinė reikšmė

1. Sukurtos ir ištirtos naujos Lietuvoje robotizuoto metalo ir polimero lakštų laipsninio formavimo technologijos.
2. Sukurta ir patentuota ekologiška metalo lakštų formavimo technologija, kuriai įrankio ir ruošinio kontaktinių paviršių tepimas pakeistas lakštinio metalo vibraciniu sužadinimu.
3. Sukurtas ir patentuotas lakštų formavimo įrankis, dėl kurio polimero standumas aplink įrankio kontaktinę sritį nemažėja, todėl nebereikia atraminės plokštės, kas leidžia paspartinti ir atpiginti produkto kūrimo procesą.

Darbo rezultatų aprobavimas

Disertacijoje pristatytų tyrimų rezultatai publikuoti trijuose „Web of Science“ žurnaluose, skelbti keturiose tarptautinėse konferencijose ir trijose patentinėse paraiškose.

Disertacijos struktūra ir apimtis

Disertaciją sudaro įvadas, keturi skyriai, bendrosios baigiamojo darbo išvados, literatūros sąrašas ir autorės publikacijų sąrašas.

Pirmajame disertacijos skyriuje apžvelgiama mokslinė literatūra apie „Pramonę 4.0“, jos samprata.

Apžvelgiama literatūra, susijusi su vienataškiu laipsnišku lakšto formavimu (angliškai SPIF), medžiagos perskirstymu šio proceso metu, formavimo įrankio trajektorijos generavimu, proceso modeliavimu bei taikymais, taip pat ir biomedicinoje.

Antrajame skyriuje pateikiami teoriniai metalo lakšto formavimo proceso rezultatai, kurie validuoti eksperimentiniais tyrimais.

Trečiajame disertacijos skyriuje pateikiami lakšto formavimo jėgos prognozavimo metodai ir rezultatai, atlikta įvairių mašininio mokymo algoritmų efektyvumo analizė.

Ketvirtajame skyriuje pristatomi polimero lakšto formavimo proceso teorinių ir eksperimentinių tyrimų rezultatai.

Išvadose pateikiami teorinių ir eksperimentinių tyrimų metu gauti rezultatai.

I. LITERATŪROS ŠALTINIŲ APŽVALGA

Laipsniškas lakštų formavimas (arba SPIF, taip pat žinomas kaip vieno taško laipsniškas formavimas) yra lakštinio metalo arba polimero formavimo technika, kai iš lakšto formuojamas galutinis produktas, atliekant mažų laipsniškų deformacijų seriją. Straipsnyje [1] pateikiama teorinė analizė, modeliuojant SPIF pagrindus, paaiškinami skaitiniai ir eksperimentiniai rezultatai, kuriuos galima rasti literatūroje. Pagrindiniai SPIF proceso modelio komponentai, tokie kaip (i) lakštinio metalo ruošinys, (ii) ruošinio laikiklis, (iii) atraminė plokštė ir (iv) besisukantis vieno taško formavimo įrankis, pateikti 1 pav. Modelis pagrįstas membranine analize su dvikrypte kontaktine trintimi plokštumoje, o dėmesys skiriamas ekstremalios deformacijos technikai naudojamai SPIF procesuose.

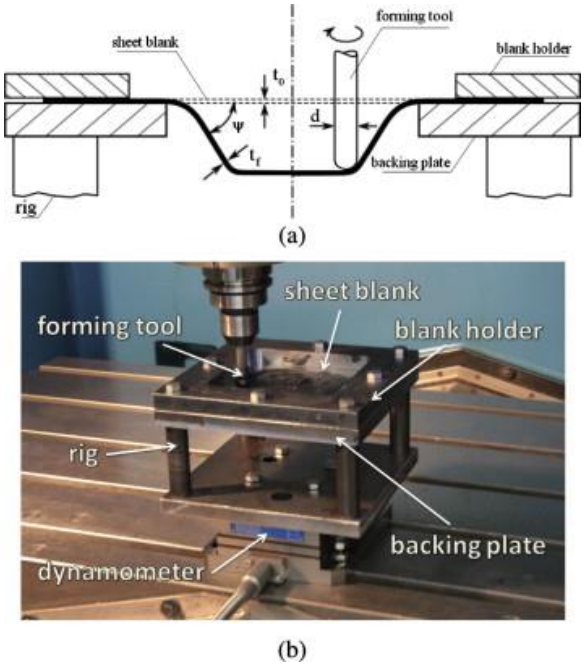

1 pav. (a) Scheminis SPIF vaizdas ir (b) eksperimentinis stendas [1]

Metalo profilio rėmas naudojamas lakšto tvirtinimui SPIF proceso metu. Atraminė plokštė palaiko lakštą, o jos anga apibrėžia SPIF įrankio darbo sritį. Įrankis

naudojamas laipsniškai formuoti lakštą, o jo judėjimo trajektorija sukuriama kompiuterinio skaitmeninio valdymo (CNC) apdirbimo centre. Įrankis turi pusrutulio formos antgalį, kuris dengia deformacijos sritį, taip sumažindamas trintį ir abrazyvinį dėvėjimąsi sąsajoje su metalo lakštu. Įrankis pagamintas iš įrankinio plieno. Įrankis gali būti sukamas staklių suklyje arba suktis laisvai. Procesui būdingos nedidelės investicijos, o įrankis gali būti pakartotinai naudojamas išgaunant įvairias gaminių formas.

Asimetriškas ir sudėtingas gaminių konfigūracijas galima suformuoti vienu įrankiu [2]. Vienas populiariausių pramoninių šios technologijos pavyzdžių – „Ford“ įmonėse įdiegta „Rapid free form technology“. Tyrimas [3] orientuotas į asimetrinių dalių formavimą naudojant CNC technologiją, nereikalaujant brangaus štampavimo. Čia yra tradicinių ir šiuolaikinių formavimo metodų palyginimas, bandant iliustruoti skirtingų laipsniško metalo lakšto formavimo metodų raidą. Tyrime [5] eksperimentais ir baigtinių elementų (FE) analize tirta formavimo proceso parametrų – įrankio tipo, įrankio dydžio, pastūmos greičio, trinties įrankio ir lakšto kontakte, lakšto plokštumos anizotropijos – įtaka formuojamumui. Nustatyta, kad formuojamumas pagerėja naudojant tam tikro dydžio sferinį įrankį su mažu pastūmos greičiu ir maža trintimi. Dėl plokštumos-anizotropijos formuojamumas skiriasi priklausomai nuo įrankio judėjimo krypties. Lazerinis SPIF (LASPIF) procesas pateiktas [9], leidžia generuoti tinkamus temperatūros laukus. 2 pav. pateikta LASPIF schema leidžia kaitinti lakšto dalį pasirinktoje vietoje šalia įrankio kontakto srities ir dinamiškai sekti formavimo įrankio judėjimą. Naudojant LASPIF procesą titano lakštams (0, 6 mm storio) formuoti, formavimo proceso kampai buvo žymiai padidinti iki atitinkamai 56° ir 64°, palyginti su 32° ir 57° kambario temperatūroje.

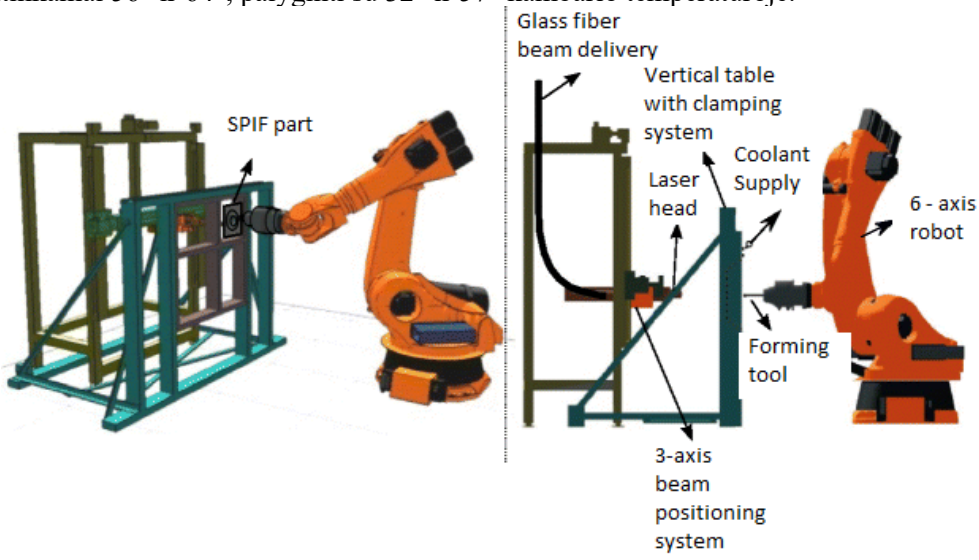

2 pav. Eksperimentinis LASPIF stendas [9]

LASPIF taip pat leidžia padidinti tikslumą, pasiekiamą sumažinus tamprųjį grįžtamąjį ryšį, nes tai yra dinaminio temperatūros gradiento pranašumas dėl vietinio šildymo.

Elektrinis karštasis laipsniškas formavimas (EHIF) siūlo alternatyvų vietinio lakštų šildymo būdą. Pagal varžinio šildymo dėsnį, elektros srovei tekant per lakštą, metalo lakštas šildomas lokaliai [10]. Skirtingų proceso parametrų įtaka 1 mm storio AZ31 formuojamumo gerinimui buvo ištirta ir gautas didžiausias šios medžiagos formavimo kampas esant apie 64°.

Vystant SPIF technologiją pasiūlyti hibridiniai deriniai, kuriems buvo sukurti dizaino ir formavimo sprendimai įrankių trajektorijos generavimui. Tam panaudotos kompiuterinio projektavimo (CAD) / kompiuterinio proceso planavimo (CAPP) / kompiuterinės gamybos (CAM) (CAX-Citrix Application Experience) aplinkos, siekiant pasiūlyti įrankio trajektorijos sprendimus, derinančius tempimo formavimą su SPIF, taip pat ir su LASPIF. Norint pritaikyti šiuos procesus, CAX platformoje buvo sukurtos ir įdiegtos naujos CAM funkcijos [26]. Reikalavimai CAX aplinkos SPIF kūrimui kartu su lakštų formavimu yra sukurti skaitmeniškai valdant trajektorijas tiek tiesiogiai CAX sistemoje, tiek nuskaitant mašinos duomenis rankinio tempimo formavimo modulio darbo režimais. Tempimo formavimas nesuteikia galutinės gaminio geometrijos, todėl būtinas tolesnis SPIF. SPIF formavimo plotų nustatymas pagrįstas tempiamojo formavimo proceso baigtinių elementų modeliavimu, kuris integruotas į CAD/CAM sprendimą. Po to atliekamas įprastas įrankio trajektorijos planavimas (3 pav. raudonai pavaizduotoms sritims).

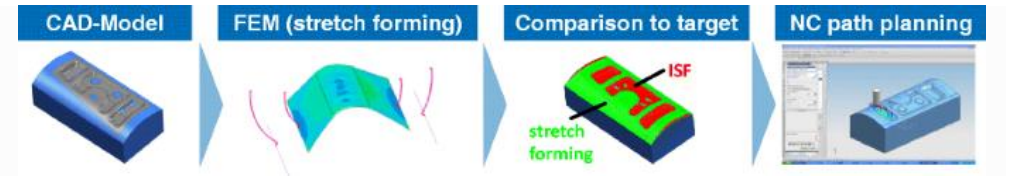

3 pav. CAD / CAM grandinė hibridiniam tempimo formavimui ir SPIF [26]

SPIF operacijų baigtinių elementų (FE) analizė paprastai taikoma gaminio geometrijai numatyti. Dauguma SPIF modeliavimo tyrimų yra pagrįsti tomis pačiomis hipotezėmis: ploni lakšto elementai, trinties sąlygos tarp įrankio ir lakšto, standus įrankis, lakšto sukietinimo jėgos dėsnis ir kt. Šie modeliai dažniausiai yra veiksmingi numatant galutinę formą, bet veikiant jėgai prognozavimo rezultatai dažnai pervertinami. Norint apriboti įrankio trajektorijos paklaidas, formavimo jėga turi būti tiksliai nuspėjama. Pagrindiniai veiksniai, nustatyti kaip svarbiausi formuojant jėgų prognozę FE modeliuojant, yra šie: baigtinių elementų tipo pasirinkimas, medžiagos šlyties įvertinimas, bandomosios medžiagos plastinės deformacijos modelis ir galiausiai lakšto ribinių sąlygų modeliavimas. Perspektyvus yra ultragarso panaudojimas SPIF proceso efektyvumo didinimui [28].

Formavimo procesas yra netiesinis dėl didelių metalo lakšto deformacijų, kurios įvertinamų plastiškumu, taip pat dėl evoliucinių kraštinių sąlygų, esant kontaktui tarp įrankio ir lakšto. Lakšto formavimo procese dalyvauja daug kintamųjų, susijusių su medžiagos savybėmis, įrankio geometrija ir proceso parametrais. Dėl to proceso

sąlygų optimizavimas yra gana sudėtingas, ypač gaminant komponentus, kuriems reikia kelių etapų, taigi ir daugiau nei vieno įrankių rinkinio. Todėl virtualus metalo lakšto formavimo komponentų bandymas FE metodu dažniausiai atliekamas remiantis iš anksto nustatytomis medžiagos savybėmis ir proceso parametrų reikšmėmis, pavyzdžiui, trinties koeficientu. Tačiau net ir naudojant FE eksperimentinio bandymo ar gamybos metu gali atsirasti nenuspėjamų defektų, kurie gali būti susiję su medžiagos savybių sklaida, įrankio geometrija ir proceso parametrais. Norint prognozuoti defektus, reikalingi ir kiti dirbtiniu intelektu pagrįsti virtualūs metodai, siekiant išgauti informaciją apie SPIF procesą, kurį veikia medžiagų savybių ir proceso parametrų pasiskirstymas. Motyvacija – sumažinti kaštus ir laiką, sugaištą gaminant brokuotus gaminius iš lakšto, t. y. prisidėti prie formavimo proceso efektyvinimo. Straipsnyje [39] pateikiamas mašininiu mokymusi pagrįstas metodas, skirtas prognozuoti lakštinio metalo SPIF defektų atsiradimą dėl medžiagų savybių pokyčių ir proceso parametrų sklaidos. Pateikiama empirinė mašininio mokymosi metodų veikimo analizė, atsižvelgiant į mokymosi modelius.

Straipsnyje [42] pasiūlyta gilaus mokymosi technika, skirta SPIF proceso geometriniam tikslumui skleisti. Geometrinio tikslumo numatymas yra vienas iš svarbiausių gaminio kokybės rodiklių. Atitinkamai apvalumas ir padėties nuokrypis yra du rodikliai, skirti matuoti geometrinį tikslumą ir pateikti du išvesties kintamuosius. Sekliojo mokymosi ir gilaus mokymosi metodai yra tiriami ir lyginami, kad būtų galima numatyti geometrinį tikslumą SPIF. Taigi, šio tyrimo tikslas yra pristatyti ir įvertinti „Deep Belief Network“ (DBN) veikimą, pagrįstą sekos mokymu, naudojant ribotą „Boltzmann“ mašinos (RBM) metodą pradinei DBN svorio matricai. Tikslus numatymas yra glaudžiai susijęs su SPIF proceso parametrų mokymu. Šie įvesties kintamieji buvo įvertinti šešiais parametrais: įrankio trajektorijos kryptimi, žingsnio gyliu, lakšto storiu, greičiu, pastūma ir formuojamos sienelės posvyrio kampu (4 pav.). Šių tyrimų rezultatai rodo, kad gilus mokymasis gali būti galingas įrankis ieškant geometrinio tikslumo prognozių SPIF

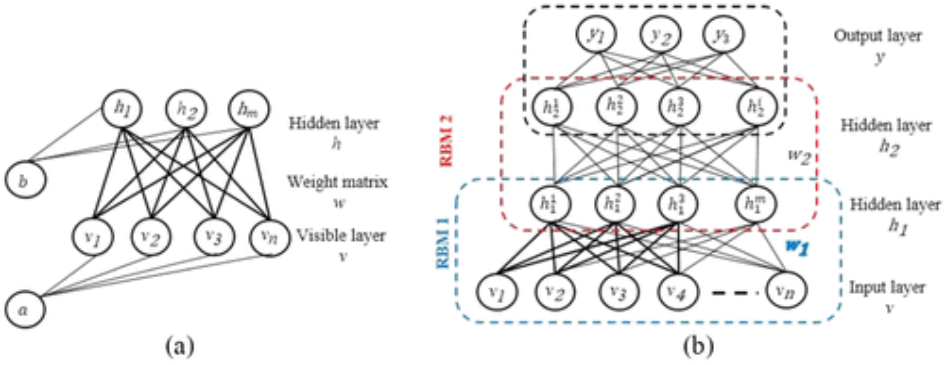

4 pav. (a) RBM ir (b) DBN struktūra [42]

Tyrime [44] buvo naudojamas dirbtinis neuroninis tinklas (ANN), siekiant numatyti mažiausią jėgą, reikalingą SPIF lakštams iš plonų aliuminio AA3003-0 ir kalamino žalvario Cu67Zn33 lydinių formuoti. Kaip įvestis buvo pasirinkti apdirbimo

parametrai, t. y. žingsnio gylis, įrankio pastūmos greitis, suklio greitis, sienelės kampas, metalo lakšto storis ir medžiagos tipas, o kaip modelio išvestis buvo pasirinkta minimali vertikalios jėgos komponentė. Modeliui parengti buvo naudojama daugiasluoksnė perceptrono ANN struktūra ir grįžtamojo atgalinio ryšio algoritmas.

SPIF, kaip vienetinei gamybai tinkamas procesas, tinka pacientų medicinos prietaisams formuoti. Gamybos procedūra baigiama išmatuojant matmenų tikslumą. Straipsnyje [45] aprašoma, kaip SPIF gali būti pritaikytas gaminant implantą, skirtą pacientui su pėdos ortoze, pagrįstą 3D skenavimu, taip iliustruojant SPIF tinkamumą kuriant individualizuotus medicinos įtaisus. Šiame straipsnyje buvo atsižvelgta į naujoviškų kulkšnies atramos pritaikymo metodų kūrimą. Tokiu būdu lakštų profiliavimui pasirinktas SPIF procesas, didinant šios technologijos vaidmenį gaminant individualizuotus produktus. Pagrindinė idėja susideda iš „ciklinio dizaino“, kai ciklas prasideda ir baigiasi paciento kūno dalies skanavimu (5 pav.).

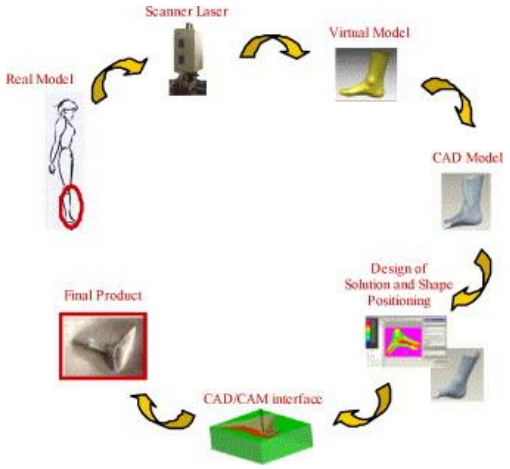

5 pav. „Ciklinio dizaino“ proceso schema [45]

Pirmiausia kulkšnies geometrija suformuota naudojant trimačio lazerinio skenavimo techniką. Ši technika leidžia atlikti labai greitą nuskaitymą be jokio diskomforto pacientui, palyginti su kontaktiniais metodais. Antrąjį žingsnį sudarė skaitmeninis kulkšnies duomenų formatas kaip „taškų debesis“, iš kurio galima gauti ištisinį paviršių CAD modelio pavidale. Trečiame etape buvo sukurta formavimo programa naudojant CAD / CAM sistemą. Tiesą sakant, gali būti naudojama technika, panaši į frezavimo procesą, vaizduojant sferinio antgalio įrankį. Reikėtų pažymėti, kad visa ši procedūra yra visiškai automatizuota. Kitas žingsnis yra gamyba. Lakštas deformuojamas pagal suprojektuotą įrankio trajektoriją ir parametrus. Paskutinis žingsnis apima suformuotos dalies matmenų identifikavimą, naudojant lazerine trianguliacija pagrįstą techniką.

Straipsnyje [46] kalbama apie atvejį, kai rekonstrukcinėje kaukolės chirurgijoje naudojamos plokštelės, iš kurių formuojami implantai. 6 pav. pavaizduota, kad

titaniniai kaukolės implantai gali būti pritaikomi šiam tikslui, nes atliekant tokias chirurgines procedūras jų koreguoti nereikia.

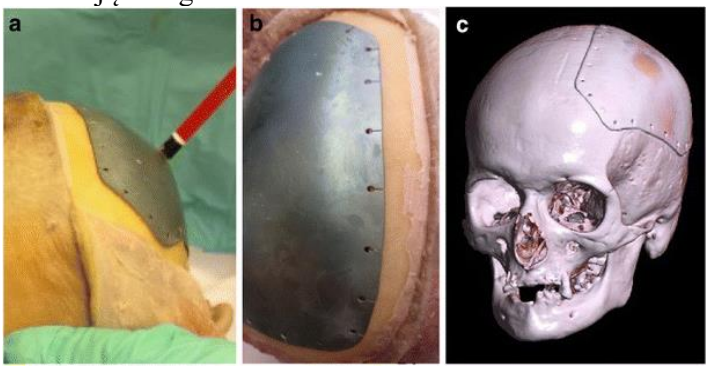

6 pav. (a) Kaukolės tyrimo implanto rezultatai (šaltinis: KU Leuven, 2017), (b) SPIF implanto pritaikymas kaukolės rekonstrukcijai, (c) kaukolė su implantu [46]

Laipsniškas polimero lakštų formavimas atsirado kaip alternatyva metalo lakštų SPIF. Vienas iš pagrindinių iššūkių formuojant kai kuriuos termoplastus yra didesnis jų trapumas, lyginant su metalais. Todėl juos formuojant sunkiau išgauti stačius kampus, didesnį gylį. Tai turi įtakos polimerų tinkamumui šiam procesui. Todėl reikia sukurti metodus, kaip pagerinti polimerinių lakštų formavimą. Siekiant supaprastinti polimerų parinkimą SPIF pritaikymui, voratinkliniu grafiku pristatomi medžiagų parinkimo kriterijai, pagrįsti plastiškumo, atspindžio ir spalvų kitimo charakteristikomis bei žaliavų kaštais (7 pav.) [51].

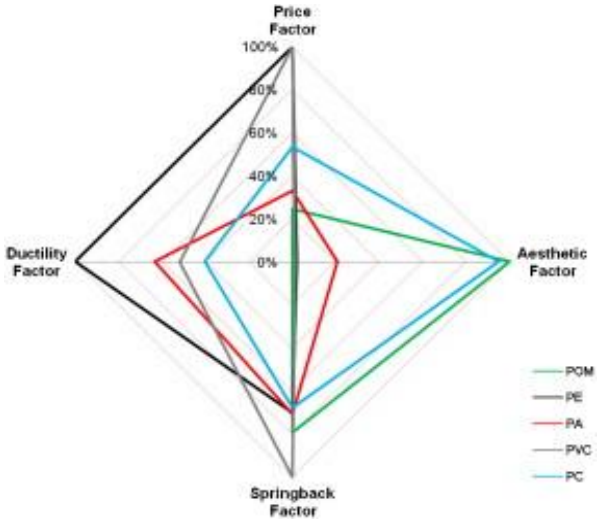

7 pav. Polimerinių medžiagų vertinimo lentelė [51]

PE ir PA pasižymėjo dideliu lankstumu ir yra tinkami dalims su dideliais sienelių kampais. PVC turi mažą spyruokliškumą ir turėtų būti naudojamas, jei

reikalingas didelis gaminių tikslumas. SPIF metu PC parodė tik nedidelį spalvos pasikeitimą ir rekomenduojamas esant aukštiems paviršiaus kokybės reikalavimams. POM buvo pats blogiausias iš visų tirtų polimerų, nes jo plastiškumas labai ribotas. Jo naudojimas neturėtų būti svarstomas gaminant SPIF gaminius. PA parodė maksimalų spyruokliškumą, kuris sumažina detalių tikslumą, nebent būtų naudojama modifikuota įrankio trajektorija.

Literatūros šaltinių apžvalga leido suformuluoti tyrimo tikslą ir uždavinius.

II. METALINIO LAKŠTO VIENATAŠKIO LAIPSNIŠKO FORMAVIMO TYRIMAS

Įvadas

Šiame skyriuje bandoma iš anksto įvertinti aliuminio lydinių lakštų deformacijas ir įtempius SPIF metu. Šio proceso FE modeliavimui buvo sukurta „LS-Dyna“ aplinka, eksperimentiniais metodais analizuojamos SPIF deformacijos jėgos. Siūlomas naujoviškas būdas sumažinti trinties jėgą tarp formavimo įrankio ir lakšto paviršiaus sužadinant ruošinį aukšto dažnio svyravimais dviem statmenomis lakšto plokštumos kryptimis. Naudojant skaitinį FE modelį ištirtos lakšto skerspjūvio mažėjimo tendencijos priklausomai nuo plastinės deformacijos laipsnio.

2.1. Trinties jėgos tarp įrankio ir metalo lakšto nustatymas

Siekiant nustatyti trinties jėgą tarp įrankio ir aliuminio lydinio lakšto atlikti skaičiavimai.

2.2. Formavimo proceso vertinimo metodika

Metalinės medžiagos SPIF proceso metu deformuojamos įrankio ir lakšto kontakto srityje. SPIF metu susidarančias jėgas galima valdyti keičiant įrankio ir ruošinio trinties koeficientą. Tepimas yra svarbus veiksnys SPIF procese, mažinantis trintį įrankio ir ruošinio sąlyčio srityje, tačiau tepalo naudojimas yra susijęs su aplinkos problemomis. Todėl būtina ieškoti kitų būdų, kaip sumažinti formavimo jėgas, susijusias su proceso dinamika. Tuo tikslu aliuminio lydinio pavyzdį bandyta sužadinti ultragarso virpesiais. Šiam tikslui sukurta eksperimentinė sąranka parodyta 8 pav. Tiriamas lakštas 1 prispaudžiamas prie rėmo ir sužadinamas dviem pjezoelektriniais keitikliais. Galios stiprintuvas 2 naudojamas pjezoelektrinio keitiklio vibracijai generuoti. Roboto ranka, suteikdama judesį įrankiui su pritvirtinta sfera, palaipsniui deformuoja lakštą. Įrankis pritvirtintas 30° laipsnių kampu, kad mechaninis impulso matuoklis STJ100 (BGI serijos skaitmeninis jėgos matuoklis su sukimo momento jutikliu „STJ100“, „Mark-10 Corp.“) 3 galėtų matuoti ir spaudimo, ir trinties momentą. Matuoklis prijungtas prie jutiklio valdiklio „Keyence LK G3001P“ 4, kuris yra prijungtas prie osciloskopo („PicoScope 3424“) 5, kuris įrašo iš mechaninio momento jutiklio gautus rezultatus į kompiuterį 6.

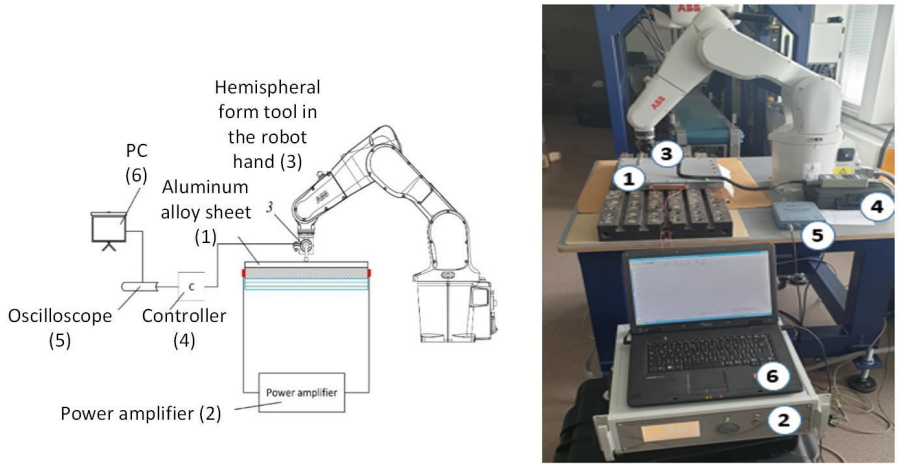

a) b)

8 pav. Eksperimentinė metalo lakšto sužadinimo įranga: 1 – aliuminio lydinio lakštas, 2 – galios stiprintuvas, 3 – pusrutulio formos įrankis roboto rankoje, 4 – jutiklio valdiklis „Keyence LK G3001P“, 5 – osciloskopas „PicoScope 3424“, 6 – kompiuteris

Mechaninis (trinties) sukimo momento matuoklis „STJ100“ (BGI serijos skaitmeninis jėgos matuoklis su sukimo momento jutikliu „STJ100“, „Mark-10 Corp.“, JAV) eksperimento metu išmatavo, kad jautrumo koeficientas yra 6 Nm/V. Įrankio trinties koeficiento ir trinties jėgos matavimo ant sausų, suteptų ir ultragarsu apdorojamų ruošinio paviršių rezultatai pateikti 1 lentelėje.

1 lentelė. Trinties koeficiento ir trinties jėgos matavimo rezultatai

Metodas	Trinties jėga	Trinties koeficientas
Be tepimo ir virpesių	3,2 N	0,5
Su tepimu	1,6 N	0,1
Su virpesiais	1,9 N	0,12

2.3. Mechaninis aliuminio lydinio lakšto bandymas

Dėl SPIF proceso sudėtingumo ir specialių sąlygų, tokių kaip lenkimas veikiant įtempiams, ciklinis lenkimas ir išlenkimas, taip pat šlyties deformacijos, kurios prisideda prie bendro formuojamumo gerinimo, reikalauja mokslinių tyrimų ir metodų. Pagrindiniai parametrai, turintys įtakos formuojamumui, yra įrankio dydis, įsigilinimas, lakštinio metalo storis ir medžiagos savybės. Formuojamumas didėja mažėjant įrankio skersmeniui, mažėjant žingsniui per apsisukimą ir lakšto storiui, o pastūma neturi reikšmingos įtakos [58]. Įtempimais pagrįstas formavimo ribinės kreivės kriterijus yra plačiai naudojamas lakštinio metalo formavimo pramonėje,

siekiant numatyti lūžį. Šis kriterijus galioja tik tada, kai deformacija yra tiesinė [59]. Tačiau SPIF proceso metu deformacijos netiesinės, o praktika naudojant įtempimu pagrįstą formavimo ribinį kriterijų dažnai lemia klaidingą formavimo ir įtrūkimų prognozės vertinimą. Įtempimais pagrįstos formavimo ribos nėra jautrios jokiems deformacijos kelio pokyčiams ir yra naudojamos modeliuojant iškirpimo ribą, kartu su pradūrimo riba, pagrįsta didžiausio šlyties įtempio kriterijumi [60]. Įtempimo kelias, įtempių būsena ir SPIF formavimo prognozė buvo įvertinti FE analize. Siekiant apibūdinti aliuminio lydinio lakšto plastiškumą ir tąsumą, buvo atlikti Erichseno suspaudimo bandymai su kvadratinėmis aliuminio plokštėmis pagal ISO 20482: 2013 (Metalinės medžiagos – Lakštai ir juostelės – Erichseno tempimo bandymas). Erichseno standartas pateikė informaciją apie lūžį esant lygiaašei įtempimo būsenai.

FE kodas „LS-Dyna“ buvo naudojamas taurės formos įspaudui imituoti ir medžiagos modeliui kalibruoti. FE modelis (9 pav., a) susideda iš atitinkamai maždaug 8500 arba 5000 kevalo baigtinių elementų. Įrankio ir aliuminio lakšto kontaktas buvo aprašytas naudojant raktinį žodį: *CONTACT_FORMING _ONE_WAY _SURFACE_TO_SURFACE. Smūgio greitis buvo 1 m/s. Aliuminio elastoplastinės savybės buvo aprašytos medžiagos modeliu „Power Law_Plasticity“ ir kalibravimui pasirinkti trys parametrai: stiprumo koeficientas, deformacijos sukietėjimo koeficientas ir pradūrimo deformacija. Modeliavimo rezultatai pateikti 9 pav., b.

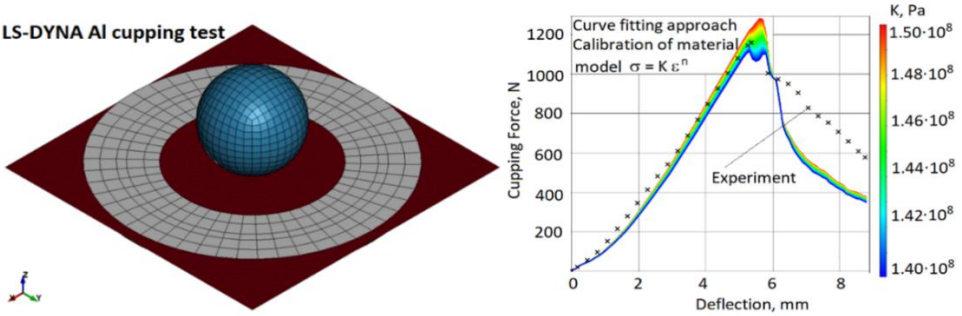

a) b)

9 pav. Taurės formavimo bandymo modeliavimas: a – skaitinis modelis, b – jėgos ir poslinkio grafikas ir modeliavimo rezultatų jautrumas kalibruoto „Power Law“ medžiagos modelio stiprumo koeficientui K (sukietinimo įtempio koeficientas n = 0,097) ir pradūrimo deformacija ε_u = 0,38)

Buvo modeliuojama keičiant trinties koeficientą nuo 0 iki 0,5. Trinties poveikis horizontaliajai jėgos komponentei parodytas 10 pav. Matyti, kad padidinus trinties koeficientą nuo 0 iki 0,5, X jėgos komponentės amplitudės padidėja maždaug 2 kartus. O poveikis vertikaliajai Z jėgos komponentei yra nereikšmingas.

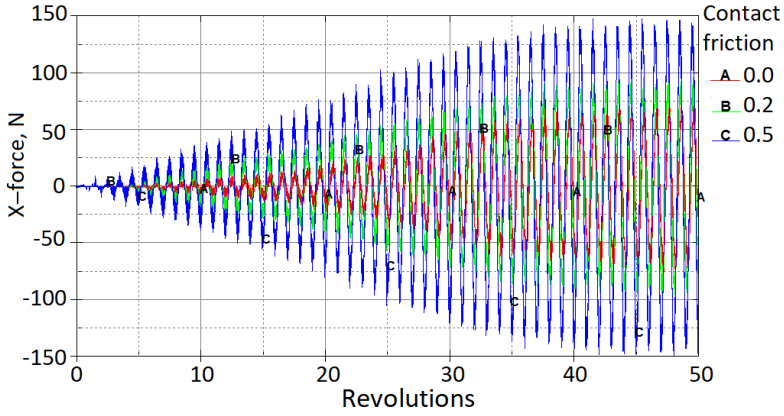

10 pav. X (trinties jėgos) kitimo priklausomybė nuo trinties koeficiento

III. METALINIO LAKŠTO VIENATAŠKIO LAIPSNIŠKO FORMAVIMO PROCESO EKSPERIMENTINIS DUOMENŲ APDOROJIMAS NAUDOJANT MAŠININIO MOKYMOSI ALGORITMUS

Įvadas

Vietoje neekologiško formavimo įrankio ir lakštinio metalo kontaktinio paviršiaus tepimo pasiūlytas inovatyvus virpesiais sužadinamo metalo lakšto ir įrankio sąveikos efektyvinimo metodas, identifikuojantis tinkamiausius lakštinio metalo ultragarsinio sužadinimo režimus. SPIF proceso jėgoms prognozuoti naudojami mašininio mokymosi (ML) metodai, tokie kaip ANN, DPR, KNN, SVM ir DT. Iš viso buvo atsižvelgta į 6 įvesties ypatybes, susijusias su mechaninėmis savybėmis, proceso parametrais ir lakšto storiu.

3.1. Eksperimentinis aliuminio lydinio lakšto SPIF tyrimas

Siekiant patikrinti modeliavimo rezultatus, pateiktus 9 b pav., parodytos lakštinio metalo pradūrimo jėgos eksperimentinio tyrimo metu 11 pav.

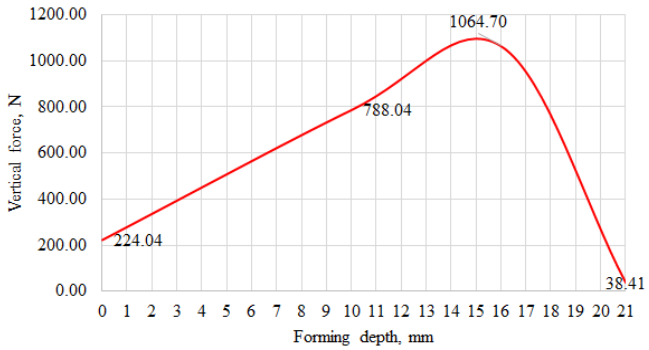

11 pav. Aliuminio lakšto pradūrimo jėgos grafinis vaizdas

Gauti rezultatai – kreivė ir pradūrimo jėgos dydis parodė gerą koreliaciją su modeliavimo rezultatais, pateiktais 9 b pav.

3.2. Eksperimentinių duomenų apdorojimas

SPIF eksperimentas buvo atliktas esant sausai, tepamai ir vibracijos sužadinamai trinčiai įrankių ir lakštinio metalo kontaktiniuose paviršiuose, o vertikalios jėgos priklausomybės nuo proceso sąlygų ir koreliacijos koeficientai rodo tiesinio ryšio tarp dviejų savybių stiprumą. Pearsono koreliacijos koeficientų reikšmės [67] svyruoja nuo −1 iki 1, tuo tarpu jei r = 0, tai kintamieji neturi ryšio; kuo koeficientas arčiau +1 arba -1, tuo ryšys stipresnis. Ženklas rodo, ar santykiai yra teigiami ar neigiami, pvz., jei r = 1, tai dvi savybės turi idealų teigiamą ryšį. Koeficientas, artimas 0, rodo silpną koreliaciją. Koreliacijos koeficientai *r* Pearsono koreliacijos matricoje (*heatmap*) pateikti 12 pav.

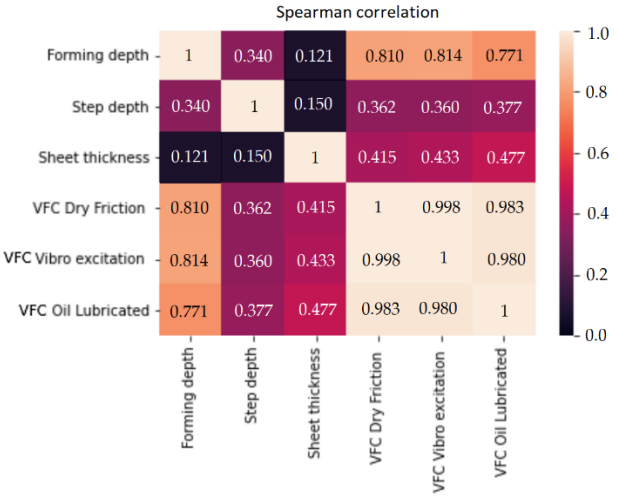

12 pav. Spearmano koreliacijos matrica ir *r* koeficientas

Matome, kad virpesiais žadinamas kontaktas (VFC Dry Friction) turi stipriausią koreliaciją su išėjimo verte, r = 0,998. Tuo tarpu įrankio įsigilinimas ir lakšto storis, kurių reikšmės yra atitinkamai r = 0,360 ir r = 0,433, parodė vidutinę koreliaciją su virpesiais žadinamas kontaktu. Tikslinga įtraukti visus šešis parametrus tolesniam prognozavimo tyrimui naudojant dirbtinius neuroninius tinklus (ANN).

3.3. Hiperparametrų optimizavimas

Hiperparametrų optimizavimas atliktas Gauso proceso regresijos (GPR), Palaikomų vektorių mašinų (SVM), Sprendimų medžių (DT), K-Artimiausių kaimynų (KNN) ir Dirbtinių neuroninių tinklų (ANN) modeliuose naudojant Bajeso optimizavimo metodą [73]. Kiti du populiarūs hiperparametrų derinimo algoritmai yra tinklelio ir atsitiktinė paieška. Tinklelio paieška yra paprasčiausias hiperparametrų derinimo algoritmas, kuris padalija hiperparametrų sritį į atskirą tinklelį. Teoriškai šis

algoritmas turėtų rasti geriausią domeno tašką, tačiau praktiškai nėra labai dažnai naudojamas, nes tai yra išsami ir daug laiko reikalaujanti paieška. Atsitiktinė paieška, skirtingai nei tinklelio paieška, neieško kiekvieno galimo hiperparametrų reikšmių derinio sprendimo, o tikrina tik atsitiktinai pasirinktą šių reikšmių poaibį. Vietoje atsitiktinės paieškos hiperparametrų srityje, Bajeso optimizavimo metodas įgalina intelektualų hiperparametrų atrankos būdą, nes naudoja ankstesnės iteracijos rezultatus, kad nuspręstų, koks bus kitas hiperparametrų rinkinys, kuris pagerins modelio veikimą. Hiperparametrų prioritetų nustatymas yra labai efektyvus ir leidžia daug greičiau rasti geriausias hiperparametrų rinkinio reikšmes, lyginant tiek su tinklelio, tiek su atsitiktine paieška. Bajeso optimizavimo metodas hiperparametrų derinimui naudoja gavimo funkciją, kad nustatytų kitą hiperparametrų reikšmių rinkinį. Yra daug skirtingų gavimo funkcijų, tokių kaip viršutinė pasitikėjimo riba, entropijos paieška, pagerėjimo tikimybė, tikėtino pagerėjimo, tačiau dažniausiai naudojamos paskutinės dvi funkcijos. Apskritai, tikėtino pagerėjimo funkcija įvertina numatomą tikslo funkcijos pagerėjimo dydį:

$$EI(x)=E[\max(0, f'-f(x)],$$

kur f' yra mažiausia iki šiol stebėta f reikšmė; x – to bandinio vieta.

ANN modelio eksperimentinei sąrankai naudojome paprastą grįžtamojo ryšio tinklą – daugiasluoksnį perceptroną (MLP), pateiktą 13 pav. ANN metodas užtikrino gerą prognozavimo tikslumą, o geriausi rezultatai, kai RMSE = 4,5337, vidutinė kvadratinė paklaida-MSE = 20,573 ir vidutinė absoliuti paklaida - MAE = 3,528, buvo gauti naudojant vieną paslėpto sluoksnio neuroninį tinklą su ištaisyto tiesinio vieneto – ReLU – aktyvinimo funkcija, 12 neuronų ir 0 reguliarumo stiprumą 25-oje hiperparametro optimizavimo proceso iteracijoje. Optimali ANN architektūra iš viso apima 3 sluoksnius: įvesties sluoksnį su 5 neuronais, paslėptą sluoksnį su 12 neuronų ir išvesties sluoksnį su vienu neuronu, suteikiančiu realią vertę.

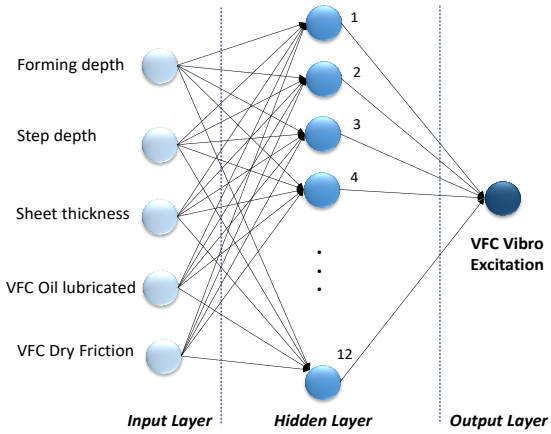

13 pav. ANN modelio architektūra, užtikrinanti geriausią MSE vertę

Pavyzdžiui, ANN modeliui optimizavimo procese buvo įtraukti keturi hiperparametrai: paslėptų sluoksnių skaičius, paslėptų sluoksnių dydis, paslėptų

sluoksnių aktyvinimo funkcija ir reguliavimo stiprumas (2 lentelė). Išnagrinėtos trys dažniausiai pasitaikančios aktyvinimo funkcijos: sigmoidinė, hiperbolinė tangentė (Tanh) ir ištaisytas tiesinis vienetas (ReLU). Reguliavimo stiprumo diapazonas buvo pasirinktas remiantis pirminiais kryžminio patvirtinimo rezultatais. Paslėptų skaičių sluoksnių verčių diapazonai ir paslėpto sluoksnio dydis buvo parinkti pagal duomenų rinkinio dydį.

2 lentelė. ANN modelio hiperparametrai.

	ANN modelio hiperparametrai			
	Paslėptų sluoksnių skaičius	**Paslėpto sluoksnio dydis**	**Aktyvinimo funkcija**	**Reguliavimo stiprumas**
Reikšmės diapazonas	[1; 3]	[10 ;100]	Sigmoid, Tanh, ReLU.	[0;0.001]

ANN metodas užtikrino gerą prognozavimo tikslumą, o geriausi rezultatai, kai RMSE = 4,5337, vidutinė kvadratinė paklaida MSE = 20,573 ir vidutinė absoliuti paklaida – MAE = 3,528, buvo gauti naudojant vieną paslėpto sluoksnio neuroninį tinklą su ištaisyto tiesinio vieneto – ReLU – aktyvinimo funkcija, 12 neuronų ir 0 reguliarumo stiprumą 25-oje hiperparametro optimizavimo proceso iteracijoje (14 pav.).

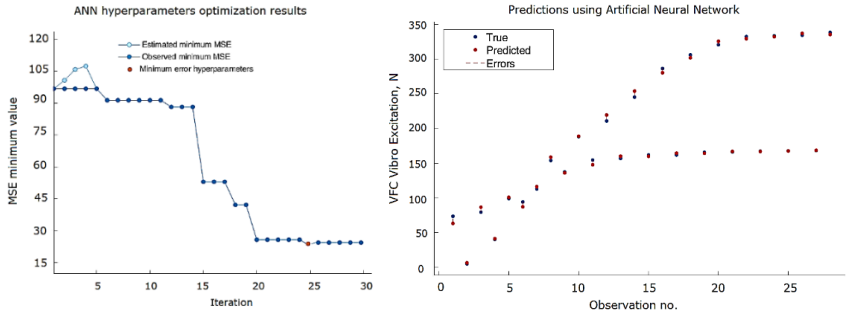

a) b)

14 pav. Minimalus MSE ANN hiperparametrų optimizavimo proceso metu (a) ir ANN modelio testavimo duomenų rezultatai (b)

Determinacijos koeficientas R^2 yra regresijos balas, kuris yra statistinis matas, nurodantis, kaip arti regresijos tiesės yra duomenys.

$$R^2 = \frac{SSR}{SST} = \frac{\sum_{i=1}^{m}(y_i - \widehat{y}_i)^2}{\sum_{i=1}^{m}(y_i - \bar{y})^2},$$

kur *SSR* yra likučių kvadratų suma, SST – bendra kvadratų suma, y – faktinė vertė, $\widehat{y}_i$ – numatoma vertė ir $\bar{y}$– vidutinė vertė.

Regresijos atveju tai matas, kaip regresijos prognozės atitinka tikrus duomenis. Skaičius 1 rodo, kad regresijos prognozės puikiai atitinka duomenis (15 pav.).

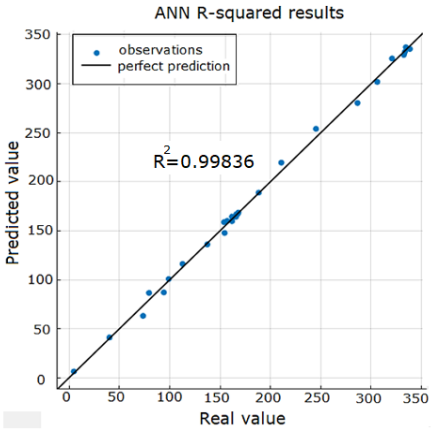

15 pav. ANN modelio regresijos prognozė

R kvadratas visada yra nuo 0 iki 100 % (arba nuo 0 iki 1,0). Kuo didesnis R kvadratas, tuo geresnis modelis. Tikslas nėra maksimaliai padidinti R kvadrato, nes modelio stabilumas ir pritaikomumas yra vienodai svarbūs. Tikrinant pakoreguotą R kvadrato reikšmę, geriausia, jei R kvadrato ir pakoreguoto R kvadrato reikšmės yra arti viena kitos. Jei taip nėra, analitikas gali pritaikyti modelį pašalinant nereikšmingus kintamuosius. Kiekvieno kintamojo *p* reikšmė patikrina nulinę hipotezę, kad koeficientas yra lygus nuliui (jokio poveikio). Maža *p* reikšmė (< 0,05) rodo, kad nulinę hipotezę galima atmesti. Kitaip tariant, kintamieji su maža *p* reikšme gali būti įtraukti į modelį, nes prognozės vertės pokyčiai yra susiję su atsako kintamojo pokyčiais. Regresijos modelis vertinamas remiantis įvairia suvestine klaidų ar likučių statistika. Tiek ANN, tiek GPR metodai buvo nustatyti kaip efektyviausi metodai kuriant VFC Vibro sužadinimo prognozavimo modelius (16 pav.).

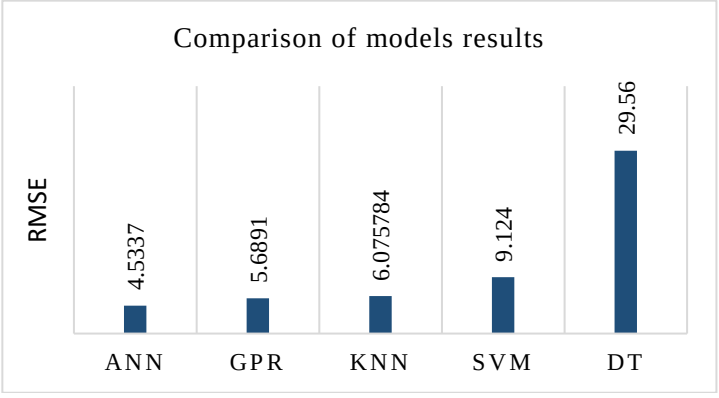

16 pav. Modelių rezultatų palyginimas

IV. ROBOTIZUOTO POLIMERO LAKŠTŲ VIENATAŠKIO LAIPSNIŠKO FORMAVIMO TYRIMAS

Įvadas

Šiame skyriuje skaitinis ir eksperimentinis polimerinių lakštų SPIF parametrų tyrimas parodė, kad didžiausias dėmesys turėtų būti skiriamas polimero šildymo technologijoms, kurios užtikrina greitą ir kokybišką SPIF procesą. Siūlomas inovatyvus polimerinio lakšto terminės deformacijos būdas, naudojant įrankį su sfera, įtaisytą žiedo formos magnete, kurio trintis su įrankio laikikliu sumažinama ultragarsu, o polimero kaitinimas atliekamas lazeriu.

4.1. Skaitmeninis polimero lakštų SPIF parametrų tyrimas

Šiame skyriuje pateikiami lakštų formavimo proceso parametrų – kaitinimo temperatūros priklausomybės nuo laiko ir polimero lakšto poslinkio nuo gravitacijos – analitinių tyrimų rezultatai. Naudojant „Ansys Transient Thermal“ kartu su „Transient Structural“ analize, buvo sukurtas polivinilchlorido (PVC) „Trovidur ESA-D“ lakšto baigtinių elementų modelis. Modeliavimo rezultatai kaitinant lakštą iš apačios – vidutinė ir maksimali lakšto deformacija veikiant žemės gravitacijai laiko atžvilgiu pateikti 17 pav., iš kurių matyti, kad lakšto deformacijos kaitinant per laiką kinta netiesiškai, kol nusistovi.

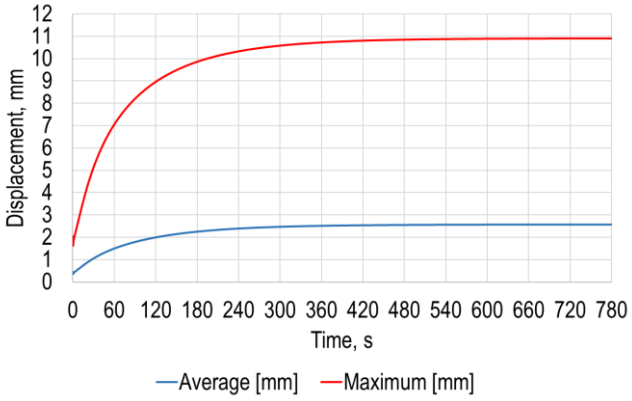

17 pav. Vidutinė ir didžiausia deformacija veikiant žemės gravitacijai polimero lakšto atžvilgiu per tam tikrą kaitinimo laiką

4.2. Skaitinio modeliavimo rezultatų validavimas

Eksperimentinių tyrimų rezultatai – polimero lakšto paviršiaus temperatūra ir laikas bei polimero lakšto poslinkio nuo gravitacijos ir temperatūros priklausomybės – yra pateikti atitinkamai 18 (a) ir (b) pav. Kaip matyti iš 18 a pav. pateiktų rezultatų, maksimali polimero lakšto temperatūra po 2 s nuo kaitinimo pradžios yra lygi 25,8 °C, o po 780 s – 45,5 °C. 18 (b) pav. parodyta, kad lakšto paviršiaus poslinkis žymiai padidėja, kai lakštas įkaista iki 31 °C ir yra didžiausias, kai polimero lakšto temperatūra yra 45,5 °C.

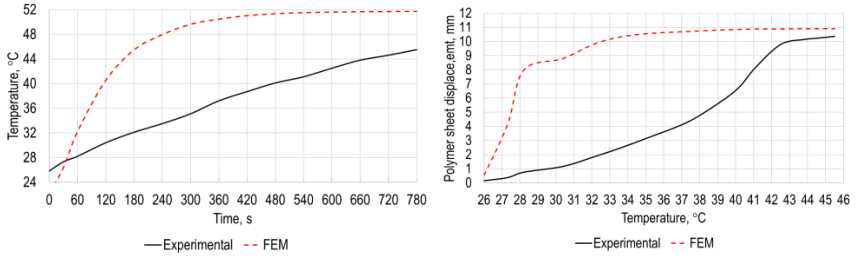

18 pav. Eksperimentinio validavimo rezultatai: a) polimero lakšto temperatūra priklausomybė nuo kaitinimo laiko; b) polimero lakšto poslinkis priklausomai nuo temperatūros

4.3. Pažangaus polimerinio lakštinio šildymo įrenginio kūrimas ir tyrimas

Siekiant eliminuoti 18 pav. ir 19 pav. modeliuojant gautas ir eksperimentiškai patvirtintas įkaitinto polimero lakšto savaimines deformacijas, atsirandančias dėl žemės gravitacijos, reikia naudoti atramines plokštes šioms deformacijoms apriboti. Tačiau tai ne tik padidina gamybos sąnaudas, bet ir sulėtina procesus, nes atraminės plokštės turi būti pritaikytos konkrečių gaminių formavimui, o tai nepageidautina vienetinės gamybos atveju. Daug efektyvesnis yra metodas, susijęs su įrankio naudojimu, kuris, kontakte su polimero lakštu, taip pat įkaitina jį iki kontroliuojamos temperatūros. Be to, toks taškinis polimero lakšto kaitinimas yra daug greitesnis. Šiai idėjai patvirtinti atliktas skaitmeninis modeliavimas, kuriuo gauta šilumos srauto parametrų kitimo kreivė (19 pav.).

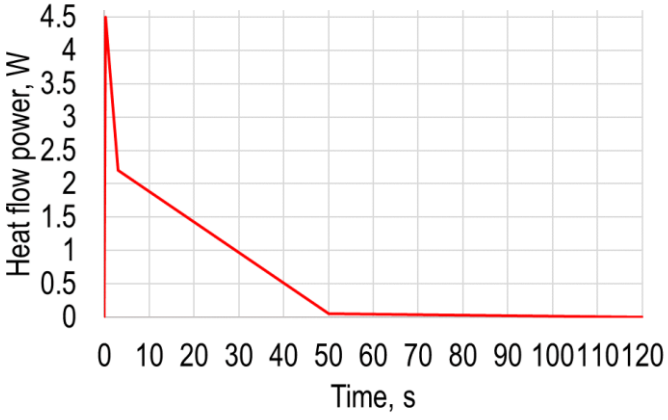

19 pav. Lakštą veikiančios šilumos srauto kreivė

Tokiam taškiniam kaitinimui būtina sukurti SPIF įrankį su taškinio kaitinimo galimybe. Polimerinio lakšto SPIF schema naudojant taškinį kaitinimo įrankį ir bendras įrangos vaizdas parodytas 20 pav.

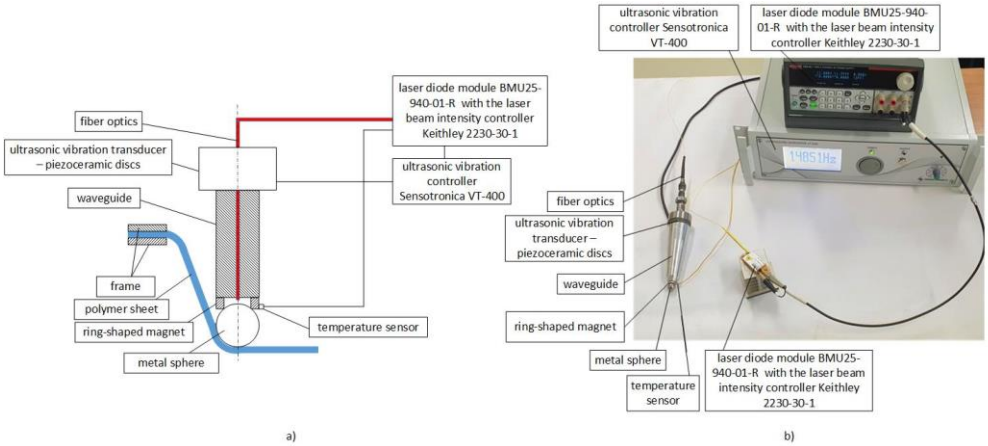

a) b)

20 pav. Palaipsnio formavimo procesas naudojant lazerinį kaitinimą. a) schema, b) įrankis

Kontakto zonoje su polimero lakštu įrankio antgalio metalinė sfera 1 3D laisvai sukasi žiedo formos magnete 2, bangolaidis 3, patalpintas įrankio korpuse, sužadinamas ultragarso virpesių keitikliu – pjezokeraminiais diskais 4, taip sumažinant metalinės sferos trintį su žiedo formos magnetu ir palengvinant jo laisvą sukimąsi. Metalinė sfera kaitinama lazerio spinduliu, nukreiptu į ją per šviesolaidį 5, o kaitinimo temperatūra kontroliuojama grįžtamuoju ryšiu per temperatūros jutiklį 6.

4.4. Eksperimentinis polimerinių lakštų SPIF parametrų tyrimas

21 pav. parodyta trumpalaikė temperatūrų pasiskirstymo formavimo lakšto paviršiuje būsena, kai jis šildomas naudojant karšto oro pistoletą ir sukurtą inovatyvų kaitinimo įrenginį, pavaizduotą 20 pav. Žemiausios temperatūros vertės (40 °C – 60 °C) buvo išmatuotos įrankio-lakšto kontakto zonoje. Pastaba: formavimo proceso metu temperatūra neturi viršyti 75 °C.

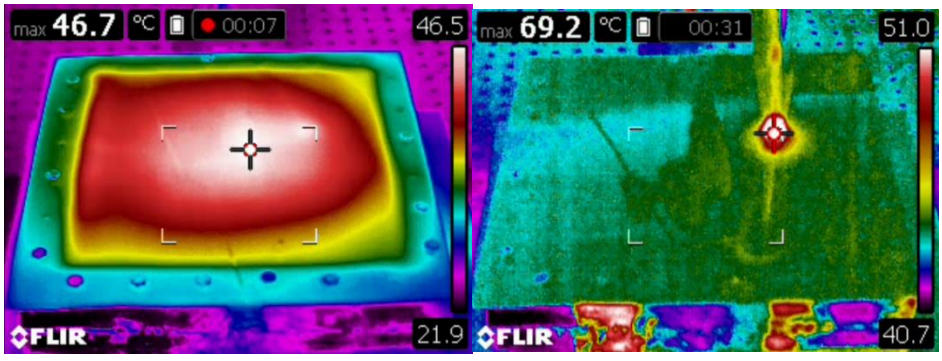

a) b)

21 pav. Polimero lakšto šiluminiai vaizdai: a) kaitinant visą paviršių, b) kaitinant inovatyviu įrenginiu paviršiaus taške

22 pav. pavaizduoti suformuoti skirtingos erdvinės geometrijos polimeriniai lakštai.

a) b) c) d)

22 pav. Suformuotų polimero PVC ESA-D lakštų nuotraukos: a) erdvinė apskrita geometrija; b) erdvinė kvadratinė geometrija; c) erdvinė gėlės geometrija; d) erdvinė žvaigždės geometrija

4.5 Robotizuoto polimero lakšto SPIF testai su skirtingais įrankiais

Pramoniniam robotui IRB1200 M2004 valdyti buvo naudojama standartinė ABB valdiklio IRC5 M2004 versija. Deja, jis neturi analoginių įėjimų. Norint išplėsti valdiklio IRCS M2001 galimybes, buvo naudojamas „DeviceNet“ tinklo adapteris CREVIS NA-9111 su analoginiu įvesties kanalų plėtiniu „PicoScope-3424“ (Pico Technology Ltd., Kembridžšyras, JK). Eksperimente naudotas sukimo momento jutiklis „Mark-10 STJ100“ užtikrino ±1 V analoginę išvestį visu mastu, o išplėstinė analoginė įvestis turėjo 0–10 V dinaminį diapazoną („PicoScope-3424“). Todėl, siekiant išnaudoti visas 12 bitų analoginės įvesties dinaminio diapazono galimybes, signalas buvo sustiprintas penkis kartus tuo pačiu metu suteikiant teigiamą poslinkio įtampą. Robotizuotos žingsnis po žingsnio grįžtamojo ryšio sistemos schema pateikta 23 pav.

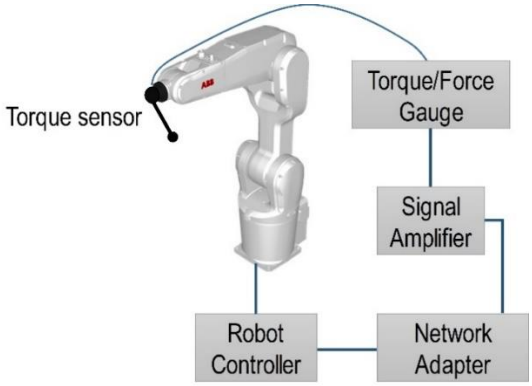

23 pav. Robotizuoto polimerinio lakšto SPIF žingsnis po žingsnio grįžtamojo ryšio sistemos schemos

Eksperimentiniai termoplastinio formavimo bandymai buvo atlikti su 2 mm storio „PVC Trovidur ESA-D“ polimero lakštu. Suformuoto pavyzdžio geometrija kūgio formos, didysis skersmuo – 140 mm, mažasis skersmuo – 80 mm, įspaudimo gylis – 30 mm. Vertikalaus ir horizontalaus slėgio žingsniai yra vienodi – 0,5 mm. Eksperimentiniai bandymai buvo atlikti su trimis skirtingais formavimo įrankiais:

1. Formavimo įrankis su Ø17 mm laisvai besisukančia sfera.

2. Formavimo įrankis su Ø10 mm besisukančia sfera, paremta žiedo formos magnetiniu laikikliu.

3. Formavimo įrankis su Ø10 mm besisukančia sfera, paremta žiedo formos magnetiniu laikikliu ir įkaitinta iki 46 °C.

Eksperimentinių tyrimų rezultatai – jėgos priklausomybė nuo formavimo įrankio ir įspaudimo gylis – pateikti 24 pav.

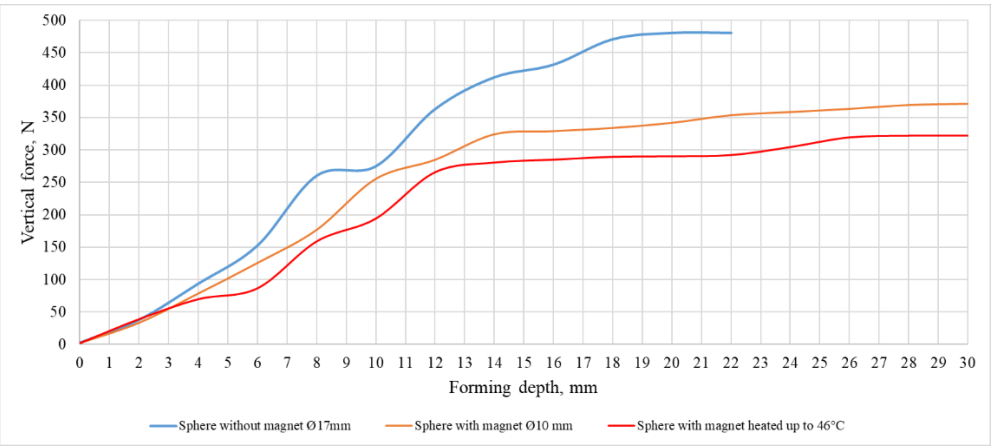

24 pav. Skirtingų įrankių formavimo jėgos priklausomybė nuo formavimo gylio

Iš pateiktų grafikų matyti, kad taškinio polimero kaitinimo formavimo įrankiu atveju vertikalioji polimero lakštą veikiančios jėgos dedamoji yra mažiausia, kas leidžia tikėtis mažiausios tikimybės sukelti formavimo defektus. Visuose polimerų formavimo procesuose pirmiausia reikia užtikrinti polimerinių medžiagų kokybę, kontroliuojant medžiagos temperatūrą. Kaitinant daugumoje polimerų vyksta šiluminiai perėjimai, kurie leidžia suprasti jų morfologiją. Didėjant kaitinimo temperatūrai, tirtų polimerų bandinių stiprumas mažėja ir atitinkamai medžiaga tampa minkštesnė. Naudojant SPIF, polimero lakštas kaitinamas iki tikslinės temperatūros, tada suformuojamas iki tam tikros formos. Polimero lakštas lokaliai deformuojamas formavimo įrankiu, kuris juda polimero lakšto paviršiumi. Kadangi judančio įrankio trajektorija yra 3D erdvėje, šis formavimo procesas yra lankstus, kad būtų pritaikytas įvairioms gaminių formoms išgauti. Kaitinimo temperatūra turėtų būti žemesnė už stiklėjimo temperatūrą, kuri buvo ideali termoplastiniam lakštui suminkštinti ir standumui palaikyti. SPIF įrenginys modifikuojamas sukuriant specializuotą įrankių laikiklį ir antgalį, kuris įkaitina polimero lakštą iki aukštesnės nei kambario, bet žemesnės už polimero stiklėjimo temperatūros ir išlaiko formavimo apkrovas. Šis procesas užtikrina lokalų ir kontroliuojamą kaitinimą, kai lakštą liečia įrankis. Įkaitęs įrankis, judantis lakšto paviršiumi, lokaliai padidina polimero plastiškumą kontaktinėje zonoje su mažesne deformavimo jėga, nesumažina polimero standumo aplink įrankio kontaktinę sritį ir pašalina atraminės plokštės poreikį.

IŠVADOS

1. Sukurtas skaitmeninis įrankio ir ruošinio sąveikos proceso modelis, kaip netiesinis dėl didelių plastinių lakšto deformacijų, įvertinantis ribines sąlygas, atsirandančias įrankio ir lakšto sąlyčio vietoje. Ištirtos metalo lakštų formavimo galimybės, nustatyti jo pramušimo kriterijai. Gauti rezultatai rodo, kad palaipsnio formavimo metu pasiekiamos efektyvios deformacijos yra daug didesnės nei nurodyta medžiagos duomenų lape, nes tempimo deformacijos vertės yra 3–8 %, o pramušimo-trūkimo deformacijos vertės, sukalibruotos taurelės pavidalo bandiniui, sudaro 38 %.

2. Sukurtu skaitmeninio metalo lakšto formavimo modeliu gauti rezultatai yra artimi gautiems eksperimentiškai su nuokrypiu iki 5%. Sukurta ir patentuota robotizuoto metalo lakšto laipsniško formavimo įranga, kuria siekiama sumažinti trinties jėgas kontakte tarp įrankio ir lakšto, pakeičiant aplinkai nekenksmingą tepimą ultragarsiniu lakšto sužadinimu dviem ortogonalinėmis kryptimis jo plokštumoje. Veikiant metalo lakštą aukšto dažnio virpesiais, trinties koeficientas įrankio ir lakšto kontakto vietoje siekia 0,12, o suteptų paviršių atveju yra lygus 0,10.

3. Vertikalios formavimo jėgos komponentės prognozavimas, ultragarsu sužadinus metalo lakštą, buvo vykdomas naudojant mašininio mokymosi – Dirbtinio neuroninio tinklo (ANN), Gauso proceso regresijos (GPR), Paramos vektorių mašinų (SVM), K-artimiausių kaimynų (KNN) ir Sprendimų medžio (DT) – algoritmus optimizuojant Bajeso hiperparametrus ir gaunant geriausią architektūrą bei siekiant geriausio įmanomo rezultato, derinant keturis technologinius įvesties tinklo hiperparametrus. Apibendrinant modeliavimo tikslumo rezultatus, buvo nustatyta, kad ANN ir GPR modeliai yra patys efektyviausi, nors jų mokymosi laikai labai skiriasi, tačiau tai mažiau svarbu nei prognozavimo tikslumo rezultatai, atsižvelgiant į tai, kad ANN modelis yra 20 % tikslesnis.

4. Polimero lakštų įvairių kaitinimo būdų skaitmeninio modeliavimo rezultatai patvirtinti naudojant sukurtą ir patentuotą robotizuotą polimerinių lakštų laipsniško formavimo stendą. Rezultatai parodė, kad naudojant užpatentuotą sprendimą polimero lakštą kaitinti kontakto su formavimo įrankiu taške naudojant lazerio spindulio energiją, yra sutrumpinamas šildymo laikas ir lakšto deformacija sumažinama 6 kartus nuo 780 s iki 120 s ir nuo 2,6 mm iki 0,42 mm. Eksperimentiniai robotizuoto polimero lakšto laipsniško formavimo tyrimai patvirtino, kad siūlomas lokalinio šildymo būdas sumažina formavimo jėgas ir lakšto kaitinimo laiką, o formavimo procesą galima atlikti be polimerinio lakšto pagrindo atramos.

REFERENCES

1.Centeno G, Bagudanch I, Martínez-Donaire AJ, García-Romeu ML, Vallellano C. Critical (2014) analysis of necking and fracture limit strains and forming forces in single-point incremental forming, Mat & Des, Vol. 63, pp. 20-29

2. Xia Z C Rapid freeform sheet metal forming: technology development and system verification, Ford motor company, 2014

3. Behera A K, Verbert J, Lauwers B, Duflou J (2013) Tool path compensation strategies for single point incremental sheet forming using multivariate adaptive regression splines, J. Computer-Aided Design, Vol. 45, 3 pp. 575-590.

4. Martins P A F., Bay N, Skjoedt M, Silva M B (2008) Theory of single point incremental forming, CIRP Annals, 57, pp. 247-252.

5. Kim Y H, Park J J 2002) Effect of process parameters on formability in incremental forming of sheet metal. J. Mater. Process. Technol. Vol. 130–131, 3, pp. 42– 46.

6. Durante M, Formisano A, Langella, A,Minutolo F M C (2009) The influence of tool rotation on an incremental forming process. J. Mater. Process. Technol., Vol. 209, 9, pp. 4621–4626.

7. Oleksik V, Trzepieciński T, Szpunar M, Chodoła L, Ficek D, Szczęsny I (2021) Single-Point Incremental Forming of Titanium and Titanium Alloy Sheets, Materials (Basel). Vol. 14(21) pp. 6372.

8.Palumbo G, Brandizzi M (2012) Experimental investigations on the single point incremental forming of a titanium alloy component combining static heating with high tool rotation speed. Mater Des Vol.40(0) pp.43–51

9. Duflou J R, Callebaut B, Verbert J, De Baerdemaeker H (2007) Laser assisted incremental forming: formability and accuracy improvement. CIRP Ann Manuf Technol Vol. 56(1) pp. 273–276. https://doi.org/10.1016/j.cirp.2007.05.063

10. Ghiotti A, Bruschi S (2010) A novel experimental set-up for warm incremental forming of AZ31B magnesium alloy sheets. Steel Res Int Vol. 81 pp. 950–954

11. Fan G, Sun F, Meng X, Gao L, Tong G (2010) Electric hot incremental forming of Ti-6Al-4V titanium sheet. Int J Adv Manuf Technol Vol.49(9) pp. 941–947

12. Ambrogio G, Filice L, Gagliardi F (2012) Formability of lightweight alloys by hot incremental sheet forming. Mater Des Vol. 34 pp. 501–508

13. Fan G, Sun F, Meng X, Gao L, Tong G (2010) Electric hot incremental forming of Ti-6Al-4V titanium sheet. Int J Adv Manuf Technol Vol.49(9) pp. 941–947

14. Zhang Q, Xiao F, Guo H, Li C, Gao L, Guo X, Han W, Bondarev AB (2010) Warm negative incremental forming of magnesium alloy AZ31 Sheet: New lubricating method. J Mater Process Technol Vol. 210(2) pp. 323–329

15. Ambrogio G, Filice L, Manco GL (2008) Warm incremental forming of magnesium alloy AZ31. CIRP Ann Manuf Technol Vol.57(1) pp. 257–260.

16. Galdos L, Argandoña ESD, Ulacia I, Arruebarrena G (2012) Warm incremental forming of magnesium alloys using hot fluid as heating media. Key Eng Mater Vol. 504–506 pp. 815–820

17. Skjoedt M, Silva MB, Martins PAF, Bay N (2010) Strategies and limits in multi-stage single-point incremental forming. J Strain Anal Eng Des Vol. 45(1) pp.33–44

18. Duflou JR, Verbert J, Belkassem B, Gu J, Sol H, Henrard C, Habraken AM (2008) Process window enhancement for single point incremental forming through multi-step toolpaths. CIRP Ann Manuf Technol Vol.57(1) pp. 253–256

19. Li J, Hu J, Pan J, Geng P (2011) Thickness distribution and design of a multi-stage process for sheet metal incremental forming. Int J Adv Manuf Technol Vol. 62(9–12) pp. 981–988

20. Arfa H, Bahloul R, BelHadjSalah H (2012) Finite element modelling and experimental investigation of single point incremental forming process of aluminum sheets: influence of process parameters on punch force monitoring and on mechanical and geometrical quality of parts. International J Mat Form Vol. 6, pages 483–510 (2013)

21. Duflou J R, Vanhove H, Verbert J, Gu J, Vasilakos I, Eyckens P (2010) Twist revisited: twist phenomena in single point incremental forming. CIRP Ann Manuf Technol Vol. 59(1) pp. 307–310

22. Malhotra R, Reddy N V, Cao J (2010) Automatic 3D spiral toolpath generation for single point incremental forming. J Manuf Sci Eng Vol. 132(6) pp. 061003

23. Vanhove H, Mohammad A, Jeswiet J (2018) Single point incremental forming: state-of-the-art and prospects, Int J Mat Form Vol. 11, pp. 743–773

24. Behera A K, Lauwers B, Duflou J R (2014) Tool path generation framework for accurate manufacture of complex 3D sheet metal parts using single point incremental forming. Comput Ind Vol. 65(4) pp. 563–584

25. Verbert J, Behera A K, Lauwers B, Duflou J R (2011) Multivariate adaptive regression splines as a tool to improve the accuracy of parts produced by FSPIF. Key Eng Mater Vol.473 pp. 841–846

26. Hirt G, Bambach M, Bleck W, Prahl U, Stollenwerk J (2015) The development of incremental sheet forming from flexible forming to fully integrated production of sheet metal parts. Advan in Prod Techn pp. 117–129

27. Göttmann A, Diettrich J, Bergweiler G, Bambach M, Hirt G, Loosen P, Poprawe R (2011) Laser-assisted asymmetric incremental sheet forming of titanium sheet metal parts. Prod Eng Res Devel Vol.5(3) pp. 263–271

28. Li P, He J, Liu Q, Yang M, Wang Q, Yuan Q, Li Y (2017) Evaluation of forming forces in ultrasonic incremental sheet metal forming, **Error! Hyperlink reference not valid. Error! Hyperlink reference not valid.**, pp. 132-139

29. He N, Li L, Yang Y, Hao X, Zhao G (2016) Finite element simulation of ultrasonic incremental forming, Materials Science Forum, Vol. 836-837, pp. 452-461

30. Zhang L, Wu C, Zhang L (2021) Ultrasonic vibration–assisted incremental sheet metal forming, The Int J Adv Man Techn Vol. 114, pp. 3311–3323

31. Belchior J, Leotoing L, Guines D, Courteille E, Maurine P (2014) A process/machine coupling approach: application to robotized incremental sheet forming, J Mat Proc Techn, Vol. 214 pp. 1605-1616

32. Eyckens P, Del-lero Moreau J, Duflou J, Van Bael A, Van Hoote P (2009) MK Modelling of sheet formability in the incremental sheet forming process, taking into-account through-thickness shear. Int. J. Mat Form, Vol. 2(1) pp. 379-382

33.Hadoush A, Van den Boogaard A H (2009) Substructuring in the implicit simulation of single point incremental sheet forming, Int J Mat Form Vol. 2 pp.181–189 Google Scholar

34. Van Bael A, Eyckens P, He S, Bouffioux C, Henrard C, Habraken AM, Duflou J, Van Houtte P (2007) Forming limit predictions for single-point incremental sheet metal forming, 10TH Esaform Conf on Mat Form, Google Scholar

35. Wu R, Hu Q, Li M, Cai S, Chen J (2021) Evaluation of the forming limit of incremental sheet forming based on ductile damage, J Mat Proc Techn, Vol. 287: 116497.Google Scholar

36. Verleysen P, Peirs J, Van Slycken J, Faes K, Duchene L (2011) Effect of strain rate on the forming behaviour of sheet metals, J Mat Proc Techn, Vol. 211(8) pp. 1457-1464

37. Guzmán C F, Yuan S, Duchêne L, Flores E I S, Habraken A M (2018) Damage prediction in single point incremental forming using an extended Gurson model, Int J Sol and Str, Vol.151 (15) pp. 45-56 Google Scholar

38. Bouffioux C, Lequesne C, Vanhove H, Duflou J R, Pouteau P, Duchêne L, Habraken A M (2011) Experimental and numerical study of an AlMgSc sheet formed by an incremental process, J Mat Proc Techn, Vol. 211(11) pp. 1684-1693 Google Scholar

39. Dib M A, Oliveira N J, Marques A E, Oliveira M C, Fernandes J V, Ribeiro B M (2020) Single and ensemble classifiers for defect prediction in sheet metal forming under variability. Neur Comp and Appl, Vol. 32, pp. 12335-12349

40. Jenab A, Sarraf I S, Green D E, Rahmann T, Worswick M J (2016) The use of genetic algorithm and neural network to predict rate-dependent tensile flow behaviour of AA5182-O sheets. Mat and Des Vol.94 pp. 262-273

41. Mekras N (2017) Using artificial neural networks to model aluminium based sheet forming processes and tools details. J. Phys.: Conf. Ser. 896 012090

42. Akrichi S, Abbassi A, Abid S, Benyahia N (2019) Roundness and positioning deviation prediction in single point incremental forming using deep learning approaches. Adv in Mech Eng, Vol.11(7) pp. 1-15

43. Trzepieciński T, Kubit A, Dzierwa A, Krasowski B, Jurczak W. (2021) Surface Finish Analysis in Single Point Incremental Sheet Forming of Rib-Stiffened 2024-T3 and 7075-T6 Alclad Alumnium Alloy Panels. Materials Vol.14(7):1640

44. Oraon M, Sharma V (2018) Predicting force in single point incremental forming by using artificial neural network, Int J of Eng, Vol. 31(1) pp. 88-95

45. Ambrogio G, De Napoli L, Filice L, Gagliardi F, Muzzupappa M (2005) Application of incremental forming process for high customised medical product manufacturing. J Mat Proc Techn Vol. 162-163 pp.156–162

46. Duflou J R., Lauwers B, Verbert J, Gelaude F, Tunckol Y (2005) Medical application of single point incremental forming: Cranial plate manufacturing Virtual Modelling and Rapid Manufacturing - Adv Res in Virt and Rap Prot, pp. 161-166

47. Bagudanch I, Lozano-Sánchez L M, Puigpinós L, Sabater M, Elizalde L E, Elías-Zúñiga A, Garcia-Romeu ML (2015) Manufacturing of polymeric biocompatible cranial geometry by single point incremental forming. Proc Eng Vol. 132 pp.267–273.

48. Lu B, Xu D K, Liu R Z, Ou H, Long H, Chen J (2015) Cranial reconstruction using double side incremental forming. Key Eng Mater, Vol. 639 pp.535–542.

49. Vanhove H, Carette Y, Vancleef S, Duflou JR (2017) Production of thin shell clavicle implants through single point incremental forming. Proc Engg, Vol. 183 pp.174–179.

50. Milutinović M, Lendjel R, Baloš S, Zlatanovič D L, Sevšek L, Papelnjak T (2021) Characterisation of geometrical and physical properties of a stainless steel denture framework manufactured by single-point incremental forming. J of Mat Res and Techn, Vol. 10, pp. 605-623

51. Martins P. A. F., Kwiatkowski L., Franzena V., Tekkaya E., Kleiner M. Single point incremental forming of polymers, CIRP Ann. - Manuf. Technol., 2009, Vol. 58(1), pp. 229–232

52. Hassan M, Hussain G, Wei H, Qadeer A, Alkahtani M (2021) Progress on single-point incremental forming of polymers, Int J Adv Man Techn, Vol. 114, pp. 1-26

53. Silva MB, Alves LM, Martins PAF (2010) Single point incremental forming of PVC: experimental findings and theoretical interpretation. Eur J Mech A/Sol, Vol. 29 pp.557–566

54. Bagudanch I, Frigolé I, Garcia-Romeu M L, Centeno G, Elías-Zúñiga A, Ciurana Q D (2015) Forming force and temperature effects on single point incremental forming of polyvinylchloride. J Mater Process Techn, Vol. 219 pp.221–229.55. Yang Z, Chen F (2020) Mechanism of twist in incremental sheet forming of thermoplastic polymer. Mater Des, Vol. 195:108997

56. Jakson K P, Allwood J M, Landert M (2008) Incremental forming of sandwich panels, J Mat Proc Techn, Vol. 204(1–3), pp. 290–303

57. Bhattacharya A, Maneesh K, Venkata Reddy N, Cao J (2011) Formability and surface finish studies in single point incremental forming. J of Manuf SciEN and Eng, Vol.133(6). https://doi.org/10.1115/1.4005458

58.Stoughton T B, Yoon J W (2011) A new approach for failure criterion for sheet metals. Int J of Plast, Vol.27(3), pp. 440-459.

59.Jawale K, Duarte J F, Reis A, Silva M B (2018) Microstructural investigation and lubrication study for single point incremental forming of copper. Int J of Sol and Str, Vol.151 pp. 145-151.

60.Gorji M, Berisha B, Manopulo N, Hora P (2016) Effect of through thickness strain distribution on shear fracture hazard and its mitigation by using multilayer aluminum sheets. J Mat Proc Techn, Vol.232 pp. 19-33.

61.Dietsch P, Tihay K, Bui-Van A, Cornette D. (2017). Methodology to assess fracture during crash simulation: fracture strain criteria and their calibration. Metallurg Res Techn, Vol.114(6)

62.Bouffioux C, Lequesne C, Vanhove H, Duflou J R, Pouteau P, Duchêne L, Habraken A M (2011. Experimental and numerical study of an AlMgSc sheet formed by an incremental process. J of Mat Proc Techn, Vol.211(11) pp. 1684-1693.

63.Silva M B, Skjødt M, Atkins A G, Bay N, Martins P A F (2008) Single-point incremental forming and formability—failure diagrams. The J Str Anal for Eng Des, Vol.43(1) pp. 15-35.

64.Allwood J M, Shouler D R, Tekkaya A E (2007) The increased forming limits of incremental sheet forming processes. In Key Eng Mat, Vol. 344, pp. 621-628. Trans Tech Publications Ltd.

65.Emmens W C, van den Boogaard A H (2007) Strain in shear, and material behaviour in incremental forming. In Key engineering materials, Vol. 344, pp. 519-526. Trans Tech Publ Ltd.

66. Hauke J, Kossowski T M (2011) Comparison of values of Pearson's and Spearman's correlation coefficients on the same sets of data. Quaest Geograph, Vol.30(2*)* pp. 87-93.

67. Browne M W (2000) Cross-Validation Methods. In J Math Psych, Vol.44(1), pp.108-132).

68. Pietersma A, Lacroixa R, Lefebvre D, Wade K (2003) Performance analysis for machine-learning experiments using small data sets, Comp and Electr in Agri, Vol. 38(1) pp. 1-17

69. Vabalas A, Gowen E, Poliakoff E, Casson A J (2019) Machine learning algorithm validation with a limited sample size, PlosOne, Vol.14(11), 20p

70. Torgyn S, Lowe D, Daga S, Briggs D, Higgins R, Khovanova N A (2015) Machine learning for predictive modelling based on small data. Biomed Eng, Vol.48(20) pp. 469-474

71. Shaikhina T, Khovanova N, Mallick K (2014) Artificial neural networks in hard tissue engineering: another look at age-dependence of trabecular bone properties in osteoarthritis. IEEE EMBS Int Conf Biom & Health Inf, pp.484-487

72. Li Y, Shami A (2020). On hyperparameter optimization of machine learning algorithms: Theory and practice, In Neurocomputing, Vol. 415, pp. 295-316.

73. Wu, J; Chen X Y, Zhang H, Xiong L D, Lei H, Deng S H (2019) Hyperparameter optimization for machine learning models based on bayesian optimization, J of Elec Sc and Techn, Vol.17(1) pp. 26-40

74. Chicco D, Warrens M J, Jurman G (2021) The coefficient of determination R-squared is more informative than SMAPE, MAE, MAPE, MSE and RMSE in regression analysis evaluation. Peer J Comp Sc, Vol.7: e623 pp. 1-24

75.Rochling industrial materials (2021). Available online: https://www.roechling.com/industrial/materials/thermoplastics/detail/trovidur-esa-d-261 (accessed on 07 October 2021).

76. Littmann W, Storck H, Walaschek J (2001) Reduction of friction using piezoelectric vibrations. In Smart Str and Mat: Damp and Isol, Int Soc Opt Phot, Vol.4331, pp. 302-311

LIST OF AUTHOR'S PUBLICATIONS

Indexed in the Web of Science with the Impact Factor

1. Ostasevicius, Vytautas; Paulauskaite-Taraseviciene, Agnė; **Paleviciute, Ieva**; Jurenas, Vytautas; Griskevicius, Paulius; Eidukynas, Darius; Kizauskiene, Laura. Investigation of the robotized incremental metal-sheet forming process with ultrasonic excitation // Materials. Basel : MDPI. ISSN 1996-1944. 2022, vol. 15, iss. 3, art. no. 1024, p. 1-18. DOI: 10.3390/ma15031024. [Science Citation Index

Expanded (Web of Science); Scopus; MEDLINE] [IF: 3,623; AIF: 5,678; IF/AIF: 0,638; Q1 (2020, InCites JCR SCIE)] [M.kr.: T 009, T 007, N 009]

2. Ostasevicius, Vytautas; **Paleviciute, Ieva**; Paulauskaite-Taraseviciene, Agne; Jurenas, Vytautas; Eidukynas, Darius; Kizauskiene, Laura. Comparative analysis of machine learning methods for predicting robotized incremental metal sheet forming force // Sensors. Basel : MDPI. ISSN 1424-8220. 2022, vol. 22, iss. 1, art. no. 18, p. 1-22. DOI: 10.3390/s22010018. [Science Citation Index Expanded (Web of Science); Scopus; DOAJ] [IF: 3,576; AIF: 3,906; IF/AIF: 0,915; Q1 (2020, InCites JCR SCIE)] [M.kr.: T 007, N 009, T 009]
3. Ostasevicius, Vytautas; Eidukynas, Darius; Jurenas, Vytautas; **Paleviciute, Ieva**; Gudauskis, Marius; Grigaliunas, Valdas. Investigation of advanced robotized polymer sheet incremental forming process // Sensors. Basel : MDPI. ISSN 1424-8220. 2021, vol. 21, iss. 22, art. no. 7459, p. 1-17. DOI: 10.3390/s21227459. [Science Citation Index Expanded (Web of Science); Scopus; MEDLINE] [IF: 3,576; AIF: 3,906; IF/AIF: 0,915; Q1 (2020, InCites JCR SCIE)] [M.kr.: T 009]

IEEE database

4. Ostaševičius, Vytautas; Jūrėnas, Vytautas; Eidukynas, Darius; Grigaliūnas, Valdas; Gudauskis, Marius; **Palevičiūtė, Ieva**; Ambrasas, Vidmantas. Peculiarities of the robotised incremental metal and polymer sheets forming // 15th international conference of mechatronic systems and materials, MSM'2020: the book of selected, peer reviewed papers, July 1-3, 2020, Bialystok, Poland / edited by: Z. Kulesza, A. Mystkowski, J. Pauk, A. Idzkowski. Piscataway, NJ : IEEE, 2020. ISBN 9781728169576. eISBN 9781728169569. p. 1-3. DOI: 10.1109/MSM49833.2020.9201731. [Scopus; INSPEC] [M.kr.: T 009].

PATENTS

1. Ostasevicius Vytautas, Jurenas Vytautas, Grigaliunas Valdas, Eidukynas Darius, Bubulis Algimantas, **Paleviciute Ieva** (2020). Incremental forming machine for sheet metal parts. Patent in LT Patent Bureau, application No. LT2020 516 6p
2. Ostasevicius Vytautas, Jurenas Vytautas, Eidukynas Darius, Grigaliunas Valdas, Gudauskis Marius, Bubulis Algimantas, **Paleviciute Ieva**, Ambrasas Vidmantas (2020). Incremental forming machine for sheet plastic parts, patent application LT2020 528 6p
3. Ostasevicius Vytautas, Jurenas Vytautas, Bubulis Algimantas, Eidukynas Darius, Paulauskaite-Taraseviciene Agnė, **Paleviciute Ieva** (2021). Sheet parts incremental forming device, patent application LT2021 549 6p

UDK 621.9.02(043.3)

SL 344. 2022-*-*, * leidyb. apsk. l. Tiražas 14 egz. Užsakymas *.
Išleido Kauno technologijos universitetas, K. Donelaičio g. 73, 44249 Kaunas
Spausdino leidyklos „Technologija“ spaustuvė, Studentų g. 54, 51424 Kaunas